OUTFLOW OF WEDDELL SEA WATERS

INTO THE SCOTIA SEA

THROUGH THE WESTERN SECTOR

OF THE SOUTH SCOTIA RIDGE

A thesis

submitted to the Department of Physics

of the Universitat de les Illes Balears

for the degree of Doctor of Physics

by

Margarita Palmer García

Palma de Mallorca, November 2012

Damià Gomis Bosch, Catedràtic d'Universitat del Departament de Física de la Universitat de les Illes Balears,

CERTIFICA

Que aquesta tesi ha estat realitzada per la Sra. *Margarita Palmer García* sota la seva direcció. I per a que així consti, firma la present,

a Palma, a dia 5 de novembre de 2012

Damià Gomis Bosch

To my parents

ACKNOWLEDGEMENTS

Last, but not least, I am especially grateful to my family for their support and to my colleagues at IMEDEA for their friendship along these years.

ABSTRACT

This work compiles the results of the analysis of hydrographical data collected in January 2008 over the western sector of the South Scotia Ridge (SSR). The cruise was carried out on board R/V Hespérides in the framework of the Synoptic Antarctic Shelf-Slope Interaction (SASSI) study, one of the core projects endorsed by the International Polar Year. SASSI focused on shelf-slope processes taking place all along the Antarctic continental slope, paying particular attention to the Antarctic Slope Front (ASF) and its associated westward Antarctic Slope Current (ASC). The Spanish contribution to SASSI (framed by the E-SASSI project) focused on the SSR region between the South Shetland Islands and the South Orkney Islands, bounded to the north by the Scotia Sea and to the south by the Weddell Sea. The main objectives of E-SASSI were (1) to quantify the outflow of Weddell Sea waters into the Scotia Sea and to determine how these waters contribute to the modification of the Southern Boundary (SB) of the Antarctic Circumpolar Current (ACC); (2) to determine the role of the Antarctic Slope Front in these processes; and (3) to track the path of the Antarctic Slope Current before diluting into the Scotia Sea. This thesis aims to answer these questions.

The sector of the SSR located between the South Shetland Islands and the South Orkney Islands is a region of especial interest. First because the gaps indenting the ridge constitute the first gate for the outflow of relatively shallow, recently ventilated waters from the northwestern Weddell Sea into the Scotia Sea. Second, because of the complexity of the bathymetry: a deep trough (the Hesperides Trough) separates the northern and southern flanks of the ridge and the location and depth of the different gaps indenting the ridge constrain the pathway of the Antarctic Slope Current. A key feature of the E-SASSI cruise with respect to previous studies conducted in the region is the unprecedented high spatial resolution of the hydrographic survey, particularly over the continental slopes. Also the coverage of all the gaps of the northern flank of the ridge was a novelty of E-SASSI. Both features have allowed a better quantification of the water mass transports in the region.

The E-SASSI physical data consist mainly of Conductivity-Temperature-Depth (CTD) and ship-mounted Acoustic Doppler Currentmeter Profiler (ADCP) measurements. The presence of narrow jets, the rough topography, the strong tidal currents observed in the

region, and the fact that velocity measurements were available only for the upper 500 meters of the water column, they all handicapped the determination of the barotropic component of the flow. Inverse modeling based on the conservation of volume, heat, and salt over an enclosed region was used to refine the barotropic component of the velocity pattern initially estimated from the adjustment of the baroclinic component of velocity profiles to the ADCP measurements. The regional circulation, including the pathway of the Antarctic Slope Current, was inferred from the joint analysis of CTD profiles and the velocity field inferred from the inverse model.

Results from a cross-slope section located in the Weddell Sea side show the well-defined structure of the Antarctic Slope Front before reaching the SSR. At the firsts gaps indenting the southern flank of the SSR the ASC has been observed to break into two branches: an inshore branch following the upper levels of the slope (700m) and an offshore branch extending over the 1600m isobath. At the northern flank the sampling covered all the gaps of the ridge and several cross-slope sections into the Scotia Sea. The inshore branch of the ASC was detected crossing a relatively shallow gap that prevents the outflow of the offshore, deeper branch and acts as a barrier for Weddell Sea Deep Water (WSDW). In spite of the higher velocities of the outflow, this shallow gap is less important in terms of Warm Deep Water (WDW) transport than the deeper Hesperides Passage hosting the outflow of the deeper branch of the ASC. This passage accounts for most of the outflow of Weddell Sea waters into the Scotia Sea and is the only gate of WSDW through the western sector of the SSR. The transports inferred from the inverse model give a net outflow of 7 ± 5 Sv, 2 Sv corresponding to WSDW and most of the other 5 Sv being WDW.

In addition to the determination of the circulation pattern we have also analyzed inflow/outflow θS diagrams. They show an overall homogenization of the outflowing waters with respect to the more variable incoming Weddell Sea waters. In the last part of this thesis we show that isopycnal mixing between inshore and offshore water masses taking place within the Hesperides Trough is the main process for the modification of subsurface and intermediate layers. We also describe the role of the ASF in the formation of the most modified WDW observed before reaching the SSR and study the contribution of this water to the modification of the Southern Boundary of the ACC, in the southwestern sector of the Scotia Sea.

RESUM

Aquest treball reuneix els resultats de l'anàlisi de dades hidrogràfiques preses el gener de 2008 durant una campanya oceanogràfica a la Dorsal d'Escòcia del Sud (Antàrtida). La campanya es va dur a terme a bord del R/V Hespérides en el marc del projecte SASSI (*Synoptic Antarctic Shelf-Slope Interaction study*), un dels projectes clau de l'Any Polar International. Aquest projecte va tenir com a objectiu l'estudi de processos entre la plataforma i el talús continental antàrtics, amb una especial atenció al Front de Talús Antàrtic i al seu corrent associat que flueix en sentit oest, el Corrent de Talús Antàrtic. La contribució espanyola a SASSI (el projecte E-SASSI) es va centrar en el sector oest de la Dorsal d'Escòcia del Sud, entre les illes Shetland del Sud i Orcades del Sud, flanquejat al nord pel Mar d'Escòcia i al sud pel Mar de Weddell. Els objectius principals d'E-SASSI eren: (1) quantificar l'exportació d'aigües del Mar de Weddell cap al Mar d'Escòcia i determinar com aquestes aigües contribueixen a la modificació de la Frontera Sud del Corrent Circumpolar Antàrtic; (2) determinar el paper que juga el Front de Talús en tots aquests processos; i (3) traçar el camí que recorr el Corrent de Talús abans de diluir-se en el Mar d'Escòcia. Aquesta tesi tracta de respondre totes aquestes qüestions.

El sector oest de la dorsal és d'especial interés. Primer perquè els passos que s'obren al llarg de la dorsal constitueixen la primera porta de sortida cap al Mar d'Escòcia d'aigües relativament poc fondes i recentment ventilades que flueixen al llarg del marge nordoest del Mar de Weddell. Segon, degut a la complexitat de la batimetria: la localització i fondària d'aquests passos, a més de l'existència d'una fossa submarina que separa aquesta banda de la dorsal en un flanc nord i un flanc sud (la Fossa d'Hespèrides), són tots factors que afecten al pas del Corrent de Talús per sobre de la dorsal. Els punts claus de la campanya E-SASSI respecte d'estudis precedents duïts a terme en aquesta regió són, d'una banda, l'elevada resolució espacial del mostreig hidrogràfic, sobretot al talús continental, i d'altra, la cobertura del mostreig, que abastà tots els passos del flanc nord de la dorsal. Ambdós aspectes han estat una aportació fonamental per part d'E-SASSI, per quan han permès una millor quantificació dels transports d'aigües en aquesta regió.

El conjunt de dades físiques d'E-SASSI són majoritàriament dades de conductivitat, temperatura i pressió (*Conductivity-Temperature-Depth,* CTD) i de velocitat (*Acoustic*

Doppler Currentmeter Profiler, ADCP). La presència de corrents prims, lo abrupt de la batimetria, els forts corrents de marea observats a la regió, i el fet de disposar de mesures directes de la velocitat només en els primers 500 metres de la columna d'aigua, tot plegat fa que la determinació del component baròtrop del fluxe sigui complicada. La modelització inversa és una tècnica que es basa en la conservació de volum, calor i sal a una regió de perímetre tancat. Aquest tècnica s'ha emprat per refinar el component baròtrop del patró inicial de velocitat obtingut a partir de l'ajust del component baroclí a dades d'ADCP. La circulació regional, i en particular el traçat del Corrent de Talús, s'ha obtingut a partir de l'anàlisi conjunt de les dades de CTD i del camp de velocitats donat pel model.

Quan als resultats, una secció hidrogràfica d'E-SASSI mostra el Front de Talús perfectament estructurat just abans d'arribar al flanc sud de la dorsal. És al primer pas d'aquest flanc on el Corrent de Talús se separa en dues branques: una interior que flueix a la part alta del talús (700m) i una de més externa que segueix la isobata de 1600m. Al flanc nord el mostreig va cobrir tots els passos i diverses seccions que travessen el talús cap a dintre del Mar d'Escòcia. La branca interna del Corrent de Talús es va detectar creuant un pas relativament poc profund, que per altra banda no només evita la sortida de la branca més externa sinó també la de *Weddell Sea Deep Water* (WSDW). Tot i les intenses velocitats del fluxe de sortida, aquest pas no és tan important com el Pas d'Hespèrides pel que fa a exportació de *Warm Deep Water* (WDW). Aquest pas no només permet la sortida de la branca externa del Corrent de Talús, sinó que és l'única porta de sortida de WSDW a la banda oest de la Dorsal d'Escòcia del Sud. Els transports obtinguts pel model invers han donat un fluxe net de sortida de 7 ± 5 Sv, dels quals 2 Sv són WSDW i gran part dels 5 Sv restants corresponen a WDW.

A més de la determinació de la circulació regional hem comparat les característiques d'entrada i sortida de les aigües a sobre de diagrames θS. L'anàlisi ha mostrat una homogeneïtzació de les aigües del Mar de Weddell quan travessen la dorsal. Hem mostrat que això és degut a processos de mescla isopicna a la Fossa d'Hespèrides pel que fa a la modificació de les capes subsuperficial i intermèdia. També hem descrit al darrer punt de la tesi el paper que juga el Front de Talús en la formació de la forma més modificada de WDW observada abans d'entrar a la dorsal i la seva contribució en la modificació de la Frontera Sud del ACC al sudoest del Mar d'Escòcia.

CONTENTS

CHAPTER 1

INTRODUCTION

1.1. Water masses and circulation in the Atlantic sector of the Southern Ocean

The dynamics in the Southern Ocean have a global impact on Earth's climate. This ocean surrounds Antarctica, a continent of extreme temperatures, and connects with the three major oceans in the planet, playing a key role in the global Ocean Conveyor Belt (Broecker, 1991). When the surface, relatively warm water carried by the Gulf Stream reaches the northern regions of the Atlantic Ocean, it cools, gets denser, and sinks near the Labrador Peninsula and Greenland. After crossing the Atlantic Ocean from North to South in the form of North Atlantic Deep Water (NADW; see upper panel of Fig. 1.1) it reaches the southern boundary of the South Atlantic Subtropical Gyre, in the Southern Ocean. There it overrides the densest Antarctic bottom waters and incorporates into the Antarctic Circumpolar Current (ACC; Reid et al., 1977).

The ACC is the most important ocean current on Earth because of its circumpolar distribution around Antarctica, strength, and transport. It flows eastwards without any interruption, with velocities of tens of cm s^{-1} (lower panel of Fig. 1.1). The ultimate driving force of the ACC are the westerly winds: sea surface Ekman processes derived from the wind pattern produce the convergence/divergence of upper waters to the north/south of approximately 50ºS, resulting into a pronounced tilting of isopycnals between 40ºS and 60ºS. The horizontal density gradients derived from the isopycnal tilting result in the observed eastward baroclinic flow through geostrophic adjustment. The tilting of isopycnals is not spatially uniform; where isopycnals are steeper the flow is more intense and a jet is observed (see upper panel of Fig. 1.2). Orsi et al. (1995) completed the previous knowledge on the ACC with an extended analysis of new available data and described the overall structure of the current. To the north, the Subtropical Front (STF) separates the ACC from the warmer surface waters of the Subtropical Gyre that also flow eastwards. On the contrary, the Southern Boundary (SB) of the ACC is the limit between its eastward flow and westward currents flowing closer to the continent and carrying water

from the subpolar regions. In between the northern and southern limits, three circumpolar jets are observed within the ACC: the Subantarctic Front (SAF), the Polar Front (PF), and the Southern ACC Front (SACCF). Although the mean circulation of the ACC is a strong eastwad flow, some branches turn southwards and incorporate into the clockwise circulation of the subpolar regions, i.e. the Weddell and Ross Gyres in the Atlantic and Pacific sectors, respectively (Orsi et al., 1993; see the lower panel of Fig. 1.2).
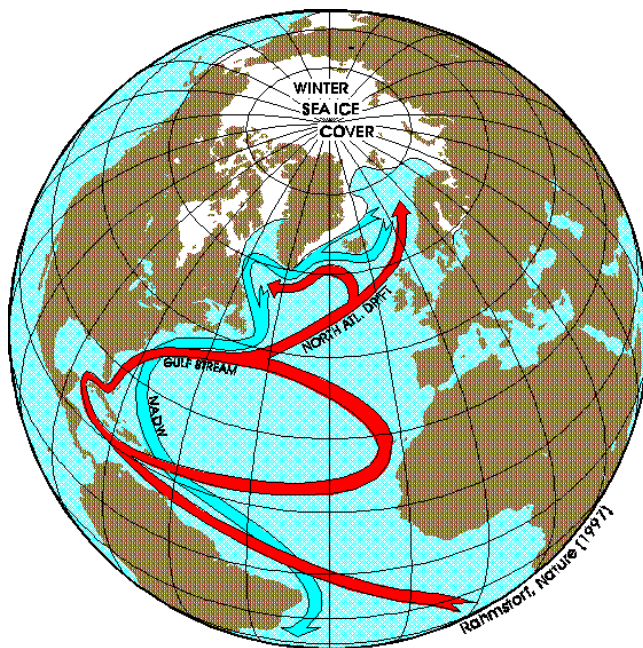
Figure 1.1*. Upper panel: scheme of the Global Conveyor Belt in the North Atlantic (Rahmstorf, 1997). Surface currents are depicted in red, deep current in cyan.*
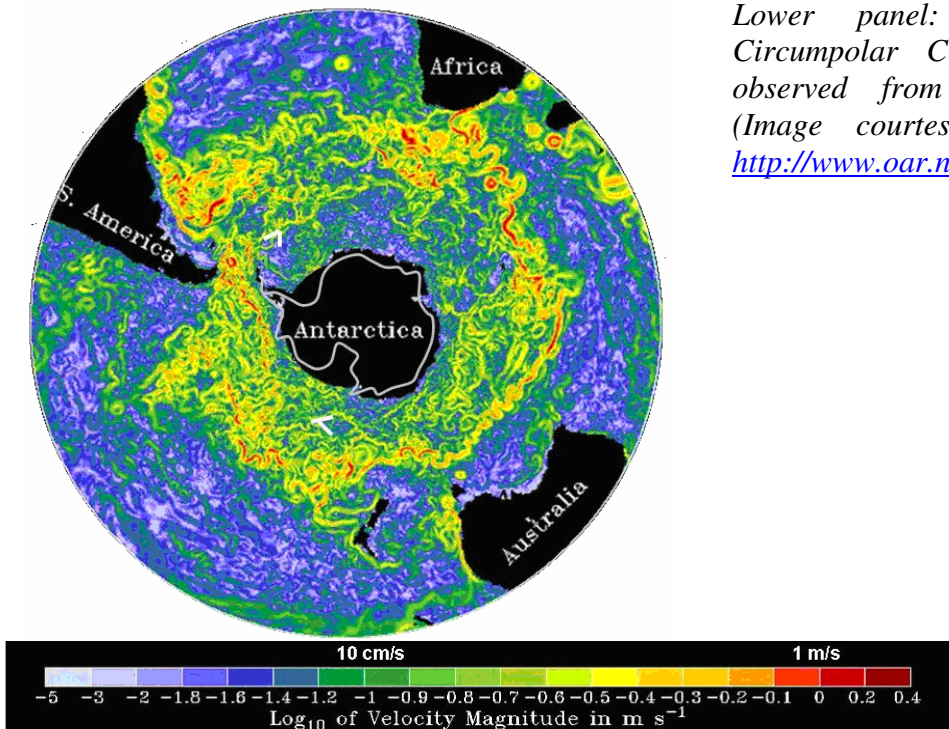
Lower panel: the Antarctic Circumpolar Current (ACC) as observed from altimetry data (Image courtesy from NOAA, http://www.oar.noaa.gov).

2
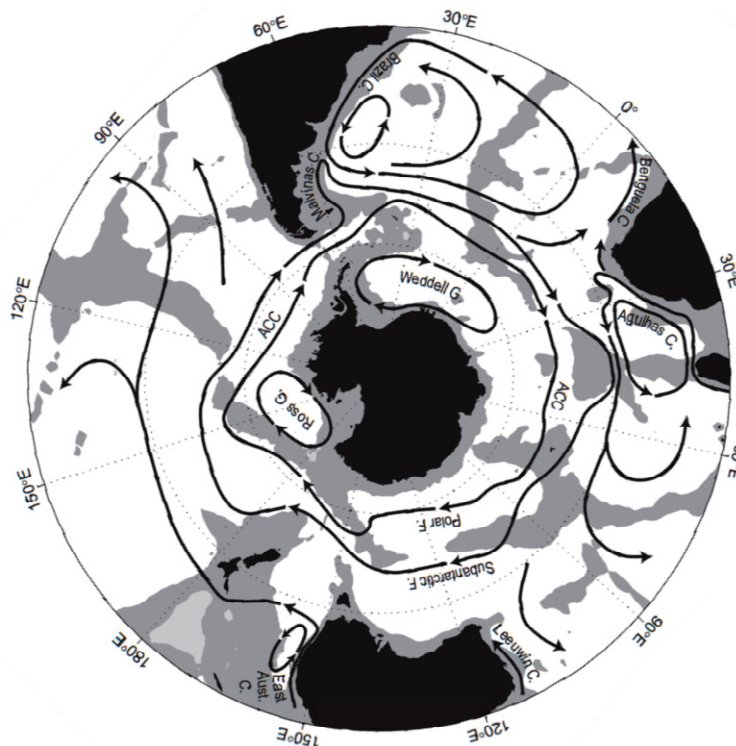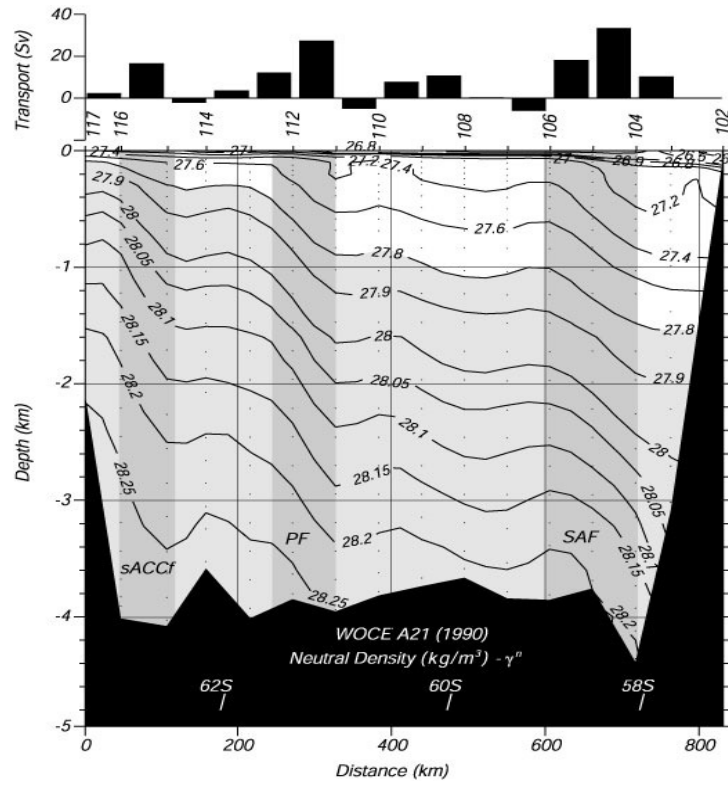
Figure 1.2. *Upper panel: density distribution at a cross-section through Drake Passage (Stewart, 2005). The frontal structure of the ACC and the baroclinic transports are also indicated. Lower panel: scheme of the circulation in the Southern Ocean (Rintoul et al., 2001).*

The water mass that characterizes the ACC is the Circumpolar Deep Water (CDW); it is the most abundant water mass south of the Polar Front (Orsi et al., 1995). At upper levels CDW is characterized by a relative temperature maximum, a minimum in oxygen, and a maximum in nutrients due to the contribution of deep waters from the Pacific and Indian Oceans; it is the so called Upper CDW, or UCDW. The lower levels are characterized by a relative salinity maximum due to the incorporation of NADW; it is the so called Lower CDW, or LCDW (Orsi et al., 1995; see Fig. 1.3). Overriding the CDW we find Antarctic Surface Water (AASW), which includes all the different surface water masses located to the south of the Polar Front of the ACC. The interaction with ice and with the atmosphere is the cause of the wide spatial and temporal variability of AASW. Thus, Shelf Water (SW) results from ocean-ice interactions (Whitworth et al., 1998), while Winter Water (WW) is the subsurface remnant of the cold, surface winter water after the summer warming of the first meters of the water column (Mosby, 1934). LCDW is the only constituent of CDW that incorporates into the subpolar gyres. These gyres allow the ventilation of LCDW when approaching to the coldest regions of the Southern Ocean and contribute to the formation of the dense Antarctic Bottom Water (AABW; Jacobs, 1991).
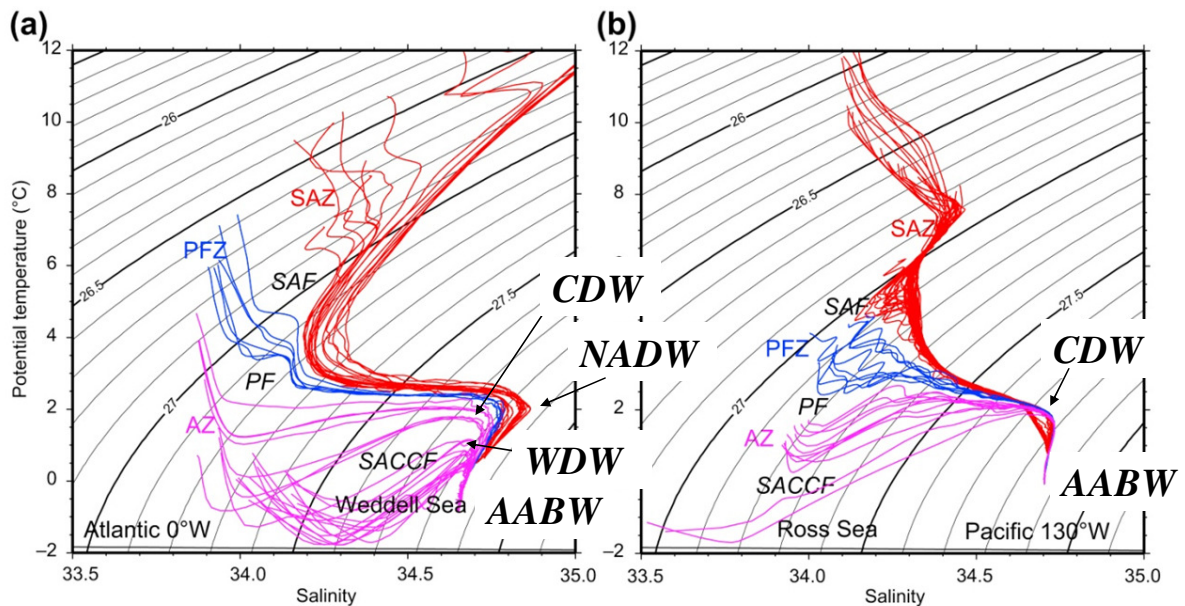
Figure 1.3. Potential temperature vs. salinity diagrams for typical profiles of the Atlantic and Pacific sectors of the Southern Ocean (Talley et al., 2011). Several deep and bottom water mass labels are added.

The incorporation of ventilated and new formed water masses from the subpolar regions ventilates the ACC and therefore the global ocean (Orsi et al., 1999). Lateral and vertical mixing are thought to be the basic processes for the ventilation of CDW. Lateral ventilation along isopycnals was shown by Whitworth et al. (1994). Naveira-Garabato et al. (2003) obtained intense diapycnal mixing rates in the Scotia Sea (southwest Atlantic) between CDW and the upper layers of AABW from the Weddell Sea. However, it is the outflow of intermediate and deep fresher and colder Weddell Sea waters towards the Southern Boundary of the ACC that makes the Scotia Sea to play a key role in the ventilation of the Southern Ocean.

CDW enters the Scotia Sea through its western boundary, the Drake Passage. Bounded north by the southern tip of the American continent and south by the South Shetland Islands, the Drake Passage forces the ACC to narrow at this longitude. After crossing the passage the ACC is bounded to the north by the Falkland Plateau and the North Scotia Ridge (NSR), and to the south by the South Scotia Ridge (SSR), both ridges running longitudinally from west to east. Whereas the gaps of the northern ridge constrain the pathways of the northern jets of the ACC (SAF and PF, Orsi et al., 1995), the gaps of the southern ridge are crucial for the ventilation of ACC waters as they allow the inflow of subpolar, ventilated waters from the Weddell Sea into the Scotia Sea (see Fig. 1.4; Naveira-Garabato et al., 2002a). The eastern boundary of the Scotia Sea is the Georgia Passage, which is much narrower than the Drake Passage as it is flanked by the South Georgia Island and the South Sandwich Islands Arc. This passage not only hosts the southern jet of the ACC (SACCF), which turns to the north at this location, but also the Southern Boundary of the ACC (Orsi et al., 1995). In the Scotia Sea, the Southern Boundary of the ACC marks the southernmost extent of CDW mixtures with Weddell Sea waters. These mixtures, which extend from the southern continental slope in the western Scotia Sea to the Georgia Passage, result in the abrupt horizontal gradients of most water properties observed in this region (see Fig. 1.4).

The hydrodynamic structure of the Weddell Gyre is crucial to understand the outflow of cold ventilated waters from the Weddell Sea into the Scotia Sea. A LCDW branch of the ACC delimited by the 27.95 and 28.27 kg m^{-3} neutral density isopycnals (Whitworth et al., 1998) turns southwards through the Southwest Indian Ridge discontinuity (eastern

boundary of the Weddell Sea; see Orsi et al., 1993) and incorporates into the cyclonic Weddell Gyre. When LCDW approaches the shelf waters of the continental margin, density gradients result in westward geostrophic currents. Along the way, mixing processes between these waters take place, eroding the core temperature and salinity maxima of LCDW and increasing the upper limit density to 28.10 kg m^{-3}. This modified water mass is referred to as Warm Deep Water (WDW; Carmack, 1974) and occupies most of the open-sea water column in the Weddell Sea. Moreover, AABW is formed in the Weddell Sea from the intrusion and mixing of SW with WDW. Defined by a neutral density > 28.27 kg m^{-3}, it is separated into Weddell Sea Deep Water (WSDW, θ > -0.7°C) and Weddell Sea Bottom Water (WSBW, θ < -0.7°C) (Reid et al., 1977). The characteristics of AABW are conditioned by the local properties of SW (Orsi et al., 1999), but they are fresher and colder than the bottom waters of the Ross Sea, the second region in bottom water formation around Antarctica. This makes the Weddell Sea particularly important for the ventilation of the Southern Ocean.
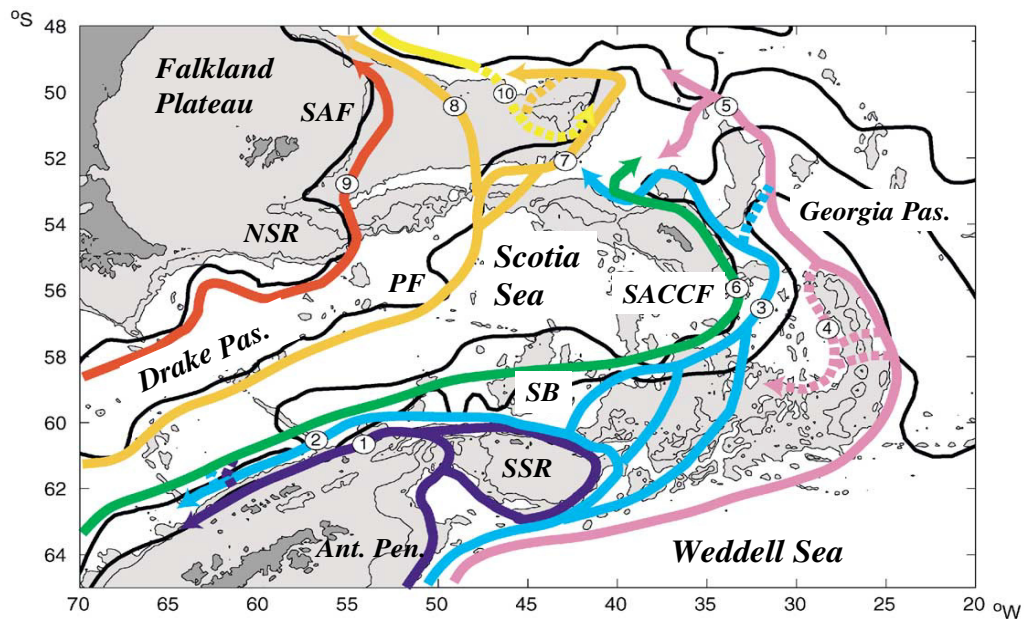
Figure 1.4. Upper panel: scheme of the circulation in the Scotia Sea (Naveira-Garabato et al., 2002a). The fronts and some topographical features are indicated.

Middle and lower panels (next page): potential temperature and salinity distributions around Antarctica at 2000m (upper level of AABW in the southern sector of the Scotia Sea, Naveira-Garabato et al., 2003). The cooling and freshening taking place in the Scotia Sea due to the outflow of Weddell Sea waters is well apparent. The higher temperatures and salinities observed in the South Atlantic correspond to NADW. Images courtesy from the WOCE Southern Ocean Atlas (http://woceatlas.tamu.edu/).
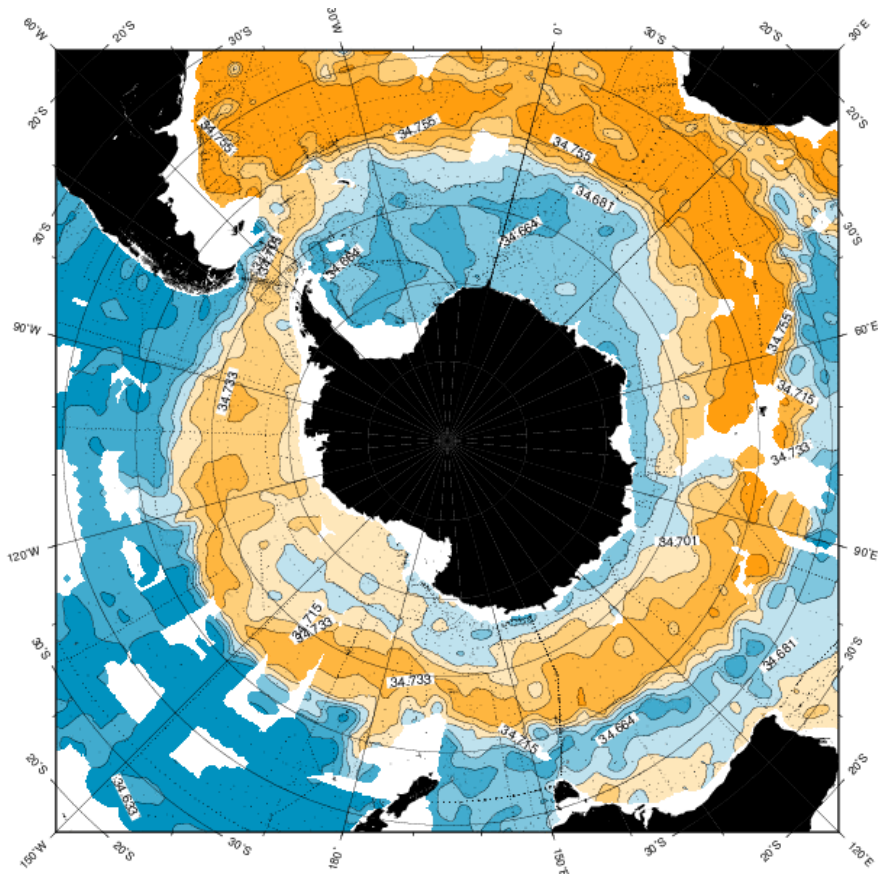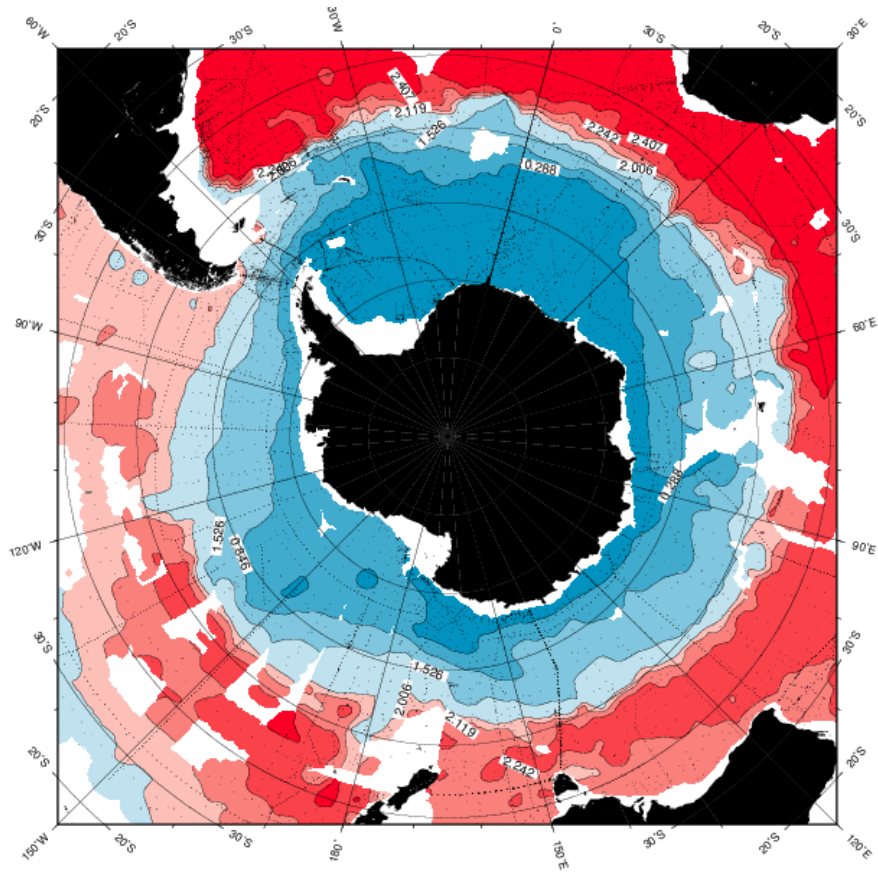
The westward currents flowing along the continental margin were measured by Sverdrup (1953) at 2ºE. The associated shelf-slope frontal structures were first described by Gill (1973) at the southern rim of the Weddell Sea, and named as the Antarctic Slope Front (ASF) after the work of Ainley and Jacobs (1981). Jacobs (1986, 1991) noted that the ASF is guided by the topography and characterized by horizontal gradients in many properties across the continental slope. The ASF is found along most of the Antarctic margin, the only exception being the western coast of the Antarctic Peninsula, where CDW floods the continental shelf (Whitworth et al., 1998). At 24ºW (southeastern Weddell Sea) for instance, a single front separating inshore cold and fresh AASW from the seaward warmer and saltier WDW (the regional component of LCDW in the Weddell Sea) has been reported (see Gill, 1973). Further west, at 32ºW and 50ºW (close to the Filchner and Ronne ice shelves), a V-shaped double frontal structure filled with AASW has been reported separating the colder but saltier SW (Whitworth et al. 1998) from the offshore WDW. A sketch of the structure of the ASF is shown in Fig. 1.5.
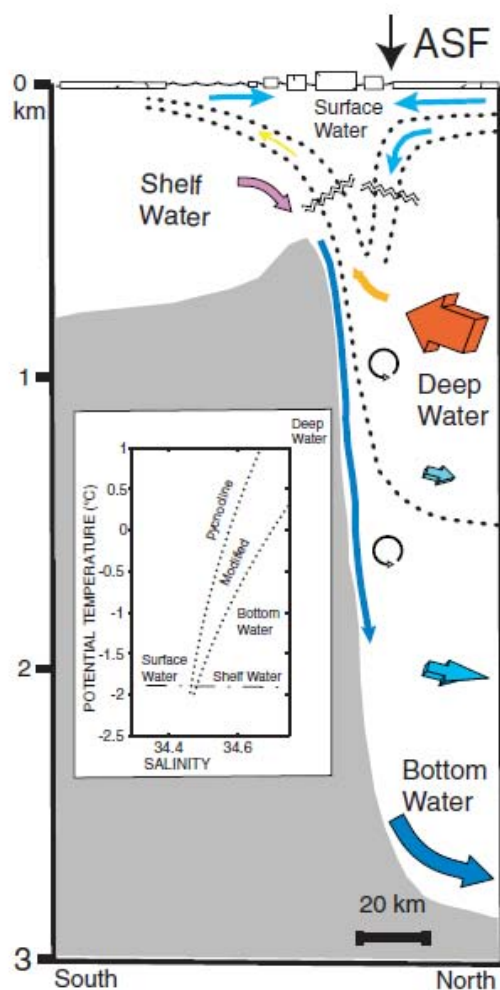
Figure 1.5. Sketch of the Antarctic Slope Front (ASF). Image courtesy from the report of the AnSlope Program "Cross-slope exchanges at the Antarctic Slope Front", available from: http://cmdac.oce.orst.edu/data/datarpt/anslope/planning/projdesc.pdf.

8

After its pathway around the continental margin of the Weddell Sea, LCDW reaches again the SSR region, now on its southern flank and in the modified form of WDW. Along the northeastern slopes of the Antarctic Peninsula (Patterson and Sievers, 1980) there is a continuous mixing of colder ($\theta_{max} < 0$ºC; Deacon and Foster, 1977), fresher, and oxygen-rich shelf waters with waters from the Weddell Gyre ($\theta_{max} > 0$ºC; Deacon and Foster, 1977). It is this branch of cooled and freshened Weddell Gyre waters that flows into the Powell Basin (the northernmost basin of the Weddell Sea) along its outer rim and then spreads into the Scotia Sea through the gaps across the SSR located to the west of the South Orkney Plateau (Gordon et al., 2001). A less modified inner branch continues eastwards, surrounds the South Orkney Plateau and outflows into the Scotia Sea through the gaps located to the east of the South Orkney Islands (see Fig. 1.4; Gordon et al., 2001; Naveira-Garabato, 2002a). The outflow into the Scotia Sea of Weddell Sea waters carries AASW, WDW, and WSDW. Whereas the lighter Weddell Sea waters ventilate the ACC isopycnally, WSDW underrides the ACC and diapycnally ventilates the lower layers of the ACC (Orsi et al., 1999). WSBW cannot cross the SSR and therefore it does not outflow into the Scotia Sea (Orsi et al., 1993).

1.2. Outline of the problem

As shown above, the dynamics of the Southern Ocean are key to the global ocean circulation and therefore to the Earth's climate. On the other hand, the extreme conditions that characterize Antarctica and its surrounding ocean make this region difficult to explore and submitted to many uncertainties. One of these uncertainties is the fate of the Antarctic Slope Current (ASC) before disappearing south of the Drake Passage, after crossing the SSR (Whitworth et al., 1998). Heywood et al. (2004) traced its pathway through the southern flank of the SSR and suggested its presence in the northern wall of the Hesperides Trough. However, its incorporation into the Scotia Sea through the northern gaps of the SSR has not been documented in spite of its importance for the ventilation of the Scotia Sea. A major reason for it is that surveying the ASC is handicapped by its narrowing as the continental slope steepens to the north of the Powell Basin and by its weakening as it crosses the complicated bathymetry of the ridge region.

Although the western sector of the SSR is the first outflowing gate for recently ventilated Weddell Sea waters into the Scotia Sea, the quantification of water mass transports through this region addressed in previous works showed some discrepancies. Conversely, the studies on the outflow through the eastern sector of the SSR (through the gaps located beyond the Orkney Plateau, such as the Orkney Passage) are more numerous and accurate (see e.g. Franco et al., 2007; Naveira-Garabato et al., 2002b), mainly because it was assumed that the ventilation of the Scotia Sea through the eastern SSR was more relevant than through the western sector. The outflow of WSDW through different eastern gaps is well documented, for instance, while it remains unclear for the region studied in this work. These are matters to be clarified too.

The questions outlined above can only be solved by means of a dedicated survey of the region. Determining the role of the ASF and the pathway of the ASC between the South Shetland and South Orkney Islands, for instance, need of high resolution observations in order to resolve such narrow features. This was precisely one of the goals of the E-SASSI project, the Spanish contribution to the international polar year project SASSI (Synoptic Antarctic Shelf-Slope Interaction study). The main objective of SASSI was to obtain a quasi-simultaneous sampling of different continental shelf-slope regions around Antarctica, focusing on the exchanges of mass, heat, and biogeochemical parameters between the continental shelves and the open ocean. These exchanges include essential processes like the modification and formation of deep and bottom waters due to the intrusion of relative warm and salty waters over the continental shelf.

The region studied by E-SASSI did not cover the regions of bottom water formation, but covered the first outflowing gate of Weddell Sea waters into the Scotia Sea. Thus, in addition to determine the role of the ASF and the pathway of the ASC between the South Shetland and South Orkney Islands, E-SASSI aimed to determine and quantify the whole outflow of Weddell Sea waters through the western sector of the SSR. The characterization of the outflow implies to study the processes involved in the modification of Weddell Sea waters as they cross this region and their interaction with Weddell Sea waters outflowing through the eastern gaps that takes place in the Scotia Sea. That is, E-SASSI was designed to characterize the contribution of Weddell Sea waters outflowing over the western sector of the SSR to the modification of the ACC and hence of the global ocean.

1.3. Objectives of this thesis

The objectives of this thesis are essentially those of the E-SASSI project. We intend to reach these objectives through the analysis of the data set collected during the intensive oceanographic cruise carried out on January 2008 (the ESASSI-08 cruise). Specific objectives of this thesis are (1) to describe the regional circulation, paying particular attention to the Antarctic Slope Current; (2) to quantify the water mass transports over the western sector of the SSR; and (3) to study the modification of Weddell Sea water masses as they cross the SSR and how do they interact with Scotia Sea waters.

The thesis is structured in an introduction, five major chapters and the conclusions. In this introduction we have given a brief overview of the circulation and water masses observed in the Atlantic sector of the Southern Ocean, we have defined several unknowns and set the objectives of our work. The second Chapter is a summary of the cruise carried out on January 2008 and of the subsequent data processing, paying particular attention to the calculation of the variables that are most relevant for our analysis. In Chapter 3 we use an inverse model in order to obtain a better estimation of the velocity field and hence of the transports over the ridge. The ultimate aim is a better understanding of the circulation of the different water masses and of the role of the bathymetry in the exchange of properties, aspects that are addressed in Chapter 4. Chapter 5 is devoted to determine the path and fate of the Antarctic Slope Current. The last of the major chapters (Chapter 6) focuses on the modification of Weddell Sea waters as they cross the western section of the SSR and outflow into the Scotia Sea. In particular we determine the water mass fractions of the modified water masses present in the region by applying an Optimum Multiparameter Technique. The main conclusions of this work are outlined in Chapter 7.

CHAPTER 2

THE ESASSI-08 CRUISE AND DATA TREATMENT

2.1. The ESASSI-08 cruise

In the framework of the recent International Polar Year, the ESASSI-08 cruise was carried out on January 2008 on board R/V Hespérides. Of the 20 scientists onboard the vessel, 15 were from the Mediterranean Institute for Advanced Studies (IMEDEA), 4 from the Texas A&M University (TAMU), and 1 from the University of East Anglia (UEA). A team of 8 technicians from the Marine Technology Unit (UTM) of the Spanish National Research Council (CSIC) was responsible for the logistics of the measurements.

After sailing from Ushuaia (Argentina) on January the 2nd, and before crossing the Drake Passage, the main task was the calibration of the ship-borne *Acoustic Doppler Current Profiler* (ADCP). The calibration based on changing the heading by 90º from one transect to another, for a total of 5 transects of about 20 minutes each. The aim was to align correctly the instrument respect to the hull of the vessel. Besides, a hydrographical cast was made to test the *Conductivity-Temperature-Depth* (CTD) sensor. The survey of the target region started the 4th of January and it covered the Weddell-Scotia Confluence region, from 60ºS to 62ºS and from 58ºW to 46ºW. The design of the sampling was planned in order to address the questions outlined in the previous section, namely the path of the Antarctic Slope Current over the western sector of the South Scotia Ridge and the export of waters from the Powell Basin to the Scotia Sea. A total of 113 CTD profiles were obtained, distributed along 11 sections running across different slopes of the SSR and along three additional transects (see Fig. 2.1 and Table 2.1). All cross-slope sections followed a similar strategy: one or two casts were obtained over the continental shelf; the others where obtained at different depths downslope, with a separation distance decreasing down to 2 nm where the sharp gradients characteristic of the slope front where detected. The CTD profiles (including those obtained by the attached oxygen and fluorescence sensors) run from surface to bottom at every station. Discrete water samplings were also taken at different depths with the aim of calibrating the CTD sensor and to measure a whole set of biogeochemical parameters.
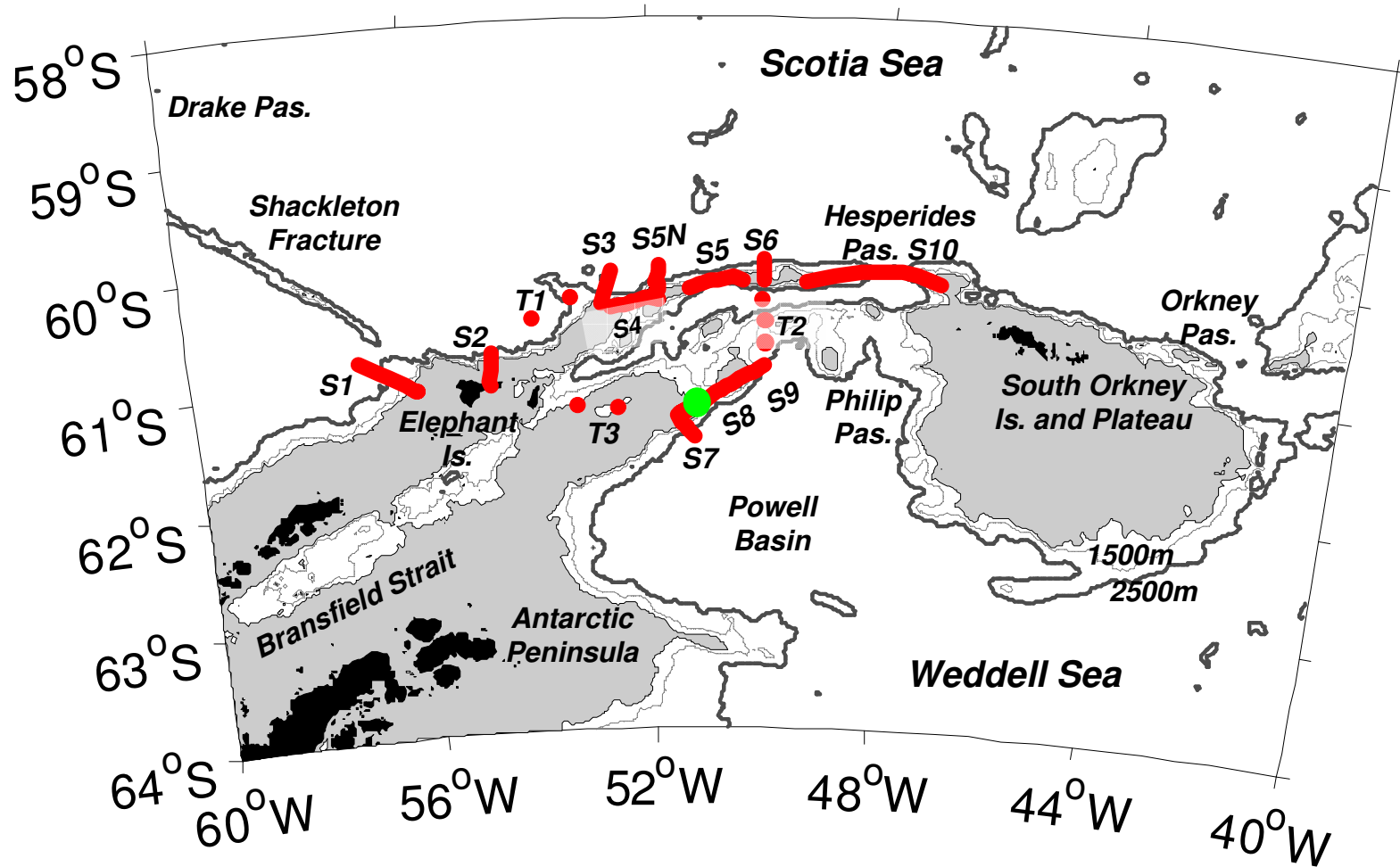
Figure 2.1. *The ESASSI-08 hydrographic sampling (transects and transit casts in red; yo-yo station in green). The bathymetry is from Smith and Sandwell (1997); the areas shallower than 1000m are shaded.*

Table 2.1. Tracking of the ESASSI-08 cruise.

Sections and transits	Starting position	Starting date	Ending position	Finishing date	Cast
Beagle Channel	Port of Ushuaia	02/01/08 11:00	55º18'S 66º20'W	03/01/08 01:00	
Calibration of the ship-borne ADCP	55º18'S 66º20'W	03/01/08 05:21	55º28'S 66º19'W	03/01/08 07:06	00
Drake Passage	55º31'S 66º14'W	03/01/08 08:09	60º44'S 57º08'W	04/01/08 22:19	
Section S1 (south of Drake Passage)	**60º48'S 57º04'W**	**04/01/08 22:48**	**61º05'S 56º03'W**	**05/01/08 21:31**	**01-08**
Transit from section S1 to section S2	61º05'S 56º03'W	05/01/08 21:31	61º04'S 54º49'W	06/01/08 02:34	
Section S2 (north of Elephant Island)	**61º04'S 54º49'W**	**06/01/08 02:34**	**60º47'S 54º47'W**	**06/01/08 19:28**	**09-15**
Transit T1, from section S2 to section S3 (Scotia Sea)	**60º47'S 54º47'W**	**06/01/08 19:28**	**60º09'S 52º42'W**	**07/01/08 11:49**	**16-17**
Section S3 (cross-slope section in the Scotia Sea)	**60º09'S 52º42'W**	**07/01/08 11:49**	**60º25'S 52º53'W**	**08/01/08 05:13**	**18-24**
Section S4 (gap of the northern flank of the SSR)	**60º27'S 52º41'W**	**08/01/08 08:53**	**60º22'S 52º01'W**	**09/01/08 09:43**	**25-35**
Section S5N (cross-slope section in the Scotia Sea)	**60º22'S 52º01'W**	**09/01/08 09:48**	**60º07'S 51º52'W**	**10/01/08 08:12**	**36-44**
Transit from section S5N to section S7	60º07'S 51º52'W	10/01/08 08:12	61º22'S 51º32'W	10/01/08 19:15	
Section S7 (cross-slope section in the Weddell Sea)	**61º22'S 51º32'W**	**10/01/08 19:15**	**61º33'S 51º15'W**	**11/01/08 14:53**	**45-53**
Transit from section S7 to section S8	61º33'S 51º15'W	11/01/08 14:53	61º17'S 51º15'W	11/01/08 18:28	
Section S8 (gap of the southern flank of the SSR)	**61º17'S 51º15'W**	**11/01/08 18:28**	**61º06'S 50º36'W**	**12/01/08 21:30**	**54-68**
Section S9 (cross-slope section in the Weddell Sea)	**61º06'S 50º36'W**	**12/01/08 21:30**	**60º57'S 50º02'W**	**13/01/08 09:50**	**69-75**

Transit T2, from section S9 to section S**6 (Hesperides Trough)**	**60º57'S 50º02'W**	**13/01/08 09:50**	**60º13'S 50º03'W**	**14/01/08 05:10**	**76-78**
Section S6 (cross-slope section in the Scotia Sea)	**60º13'S 50º03'W**	**14/01/08 05:10**	**60º03'S 50º02'W**	**14/01/08 17:40**	**79-85**
Transit from section S6 to section S5	60º03'S 50º02'W	14/01/08 17:40	60º17'S 51º19'W	15/01/08 02:58	
Section S5 (gap of the northern flank of the SSR)	**60º17'S 51º19'W**	**15/01/08 02:58**	**60º13'S 50º25'W**	**15/01/08 16:49**	**86-93**
Transit from section S5 to section S10	60º13'S 50º25'W	15/01/08 16:49	60º13'S 49º19'W	15/01/08 22:35	
Section S10 (Hesperides Passage)	**60º13'S 49º19'W**	**15/01/08 22:35**	**60º12'S 47º02'W**	**16/01/08 22:45**	**94-100**
Transit from section S10 to Signy Is. (South Orkney Islands)	60º12'S 47º02'W	16/01/08 22:45	Signy	18/01/08 04:30	
Transit from Signy Is. to the yo-yo station	Signy	18/01/08 05:00	61º15'S 51º13'W	19/01/08 16:55	
Yo-yo station	61º15'S 51º13'W	19/01/08 16:55	61º15'S 51º16'W	20/01/08 04:31	101-111
Transit T3, southwestern flank of the SSR	**61º15'S 51º16'W**	**20/01/08 04:31**	**61º14'S 53º19'W**	**20/01/08 17:16**	**112-113**
Transit from the last station to Deception Island	61º14'S 53º19'W	20/01/08 17:16	Deception Island		

2.2. Data set and instrumentation

The rosette used in the ESASSI-08 cruise hosted a Seabird 911 CTD and 24 Niskin bottles of 12 l each for water samplings. The down/up casts were carried out at a speed between 45 and 60 m min^{-1} and were controlled from an onboard computer. In this way CTD measurements were observed in real time and the depth of the bottle samples (taken during the upcasts) were decided looking at the downcast profiles. The variables measured by the CTD multisensor were conductivity, temperature, and pressure, but the acquisition software also provided salinity (inferred from conductivity), density (inferred from temperature, salinity and pressure using the state equation) and depth (inferred from the vertical integration of the specific volume with pressure). Dissolved oxygen, turbidity, and fluorescence were also measured with additional sensors attached to the CTD.

The water samples from the bottles provided accurate measurements of salinity, dissolved oxygen and chlorophyll, which were used for the calibration of the conductivity, oxygen, and fluorescense sensors of the CTD, respectively. Clorofluorocarbons (CFC), nutrients (silicates, phosphates, nitrates) and other biogeochemical parameters such as pH, alkalinity or dissolved organic carbon were also measured from the water samples. Phosphates will be used in this work as water mass tracers.

The vessel-mounted ADCP measures the speed and direction of currents relative to the ship (in which case the ship velocity must be accurately determined in order to infer absolute current velocities) or relative to the bottom (only in waters shallower than 500m approximately). The vertical resolution and range of the measurements depends on the accoustic frequency: higher frequencies result in a higher vertical resolution, but in a shorter vertical range. For the ESASSI-08 cruise the ADCP was set to provide measurements in 8m vertical cells covering from surface to about 600m depth. Data were collected both at stations and along the track of the ship. The accuracy of a single profile was estimated in 0.09 m s^{-1} in the upper 450m and in 0.17 m s^{-1} from 450m to 600m. The accuracy can be improved by averaging a set of velocity profiles: for the ESASSI-08 cruise we averaged the profiles in 20-min intervals (i.e., over 2 nm along track), which in the best case would resulted in an accuracy of the order of 0.02-0.03 m s^{-1}.(errors can be significantly larger due to inaccuracies in the navigation system, for instance).

Additional measurement were those provided by a thermosalinograph measuring in a continuous way a flow of water sucked from 4 - 5m depth. The same flow was used to measure also CFCs and other parameters. Data from the meteorological station, different acoustic echo-sounders, and the navigation systems (GPS, heading, velocity of the ship) were all acquired in an automatic mode and saved by the System for Oceanographical Data Adquisition (SADO) installed onboard.

Not all the variables have the same spatial resolution. The variables saved by the SADO and the ship-borne ADCP cover most of the track of the ship, though in the case of the ADCP they only cover the upper (600m) levels. Data from the CTD and the attached oxygen, fluorescence and transmittance sensors are discrete in the horizontal dimension (they were acquired only at station points) but are continuous in the vertical and cover from the surface to the bottom. The water samples from the Niskin bottles are discrete in both, the horizontal dimension (they were sampled at every CTD station) and in the vertical dimension (the samples were obtained typically at 10-12 levels in the vertical).

The range of measurement of the temperature sensor of the CTD is from -5ºC a +35ºC, with a nominal accuracy of ±0.001 ºC and a resolution of ±0.0002 ºC. Although this sensor can hardly be calibrated from cruise measurements, it is considered to be quite reliable provided it is routinely calibrated in between cruises (as it was the case). The pressure sensor used in ESASSI-08 had a nominal accuracy of ±0.015% and a nominal resolution of ±0.001% of the whole measurement range, which was of 10500m (i.e., an accuracy of about 1.5m and a resolution of about 0.1m). The nominal accuracy and resolution of the conductivity sensor expressed in practical salinity units were ±0.001 and ± 0.0002, respectively. Unlike the temperature sensor, the conductivity cell is more sensible to drifts due to environmental conditions, and therefore a calibration against water sample salinity measurements is highly recommended. The same applies to the dissolved oxygen sensor. The calibration procedures and their results are presented in the following.

2.3. Calibrations

2.3.1. Conductivity sensor

A total of 258 salinity samples were analyzed onboard with an autosalinometer, a Guildline Portasal 8410A calibrated with IAPSO Standard Seawater ampoules. The measurement range of that model is from 2 to 42, the accuracy is ±0.003 and the resolution is ±0.0003. Although the nominal accuracy of the salinometer is worse than the accuracy of the conductivity sensor of the CTD, the latter is more submitted to drifts and therefore an in situ calibration against the water samples is highly recommended.

Water sample salinity measurements covered a wide range of stations and depths, recording values from 34.1 to 34.8. The linear regression between water samples and CTD values gave a correlation coefficient of 0.9991 and a mean value for the residuals of ±0.003, which is within the value of the nominal accuracy of the autosalinometer (Fig 2.2). Hence, no further correction apart from the linear regression towards the water samples was applied to salinity CTD data.
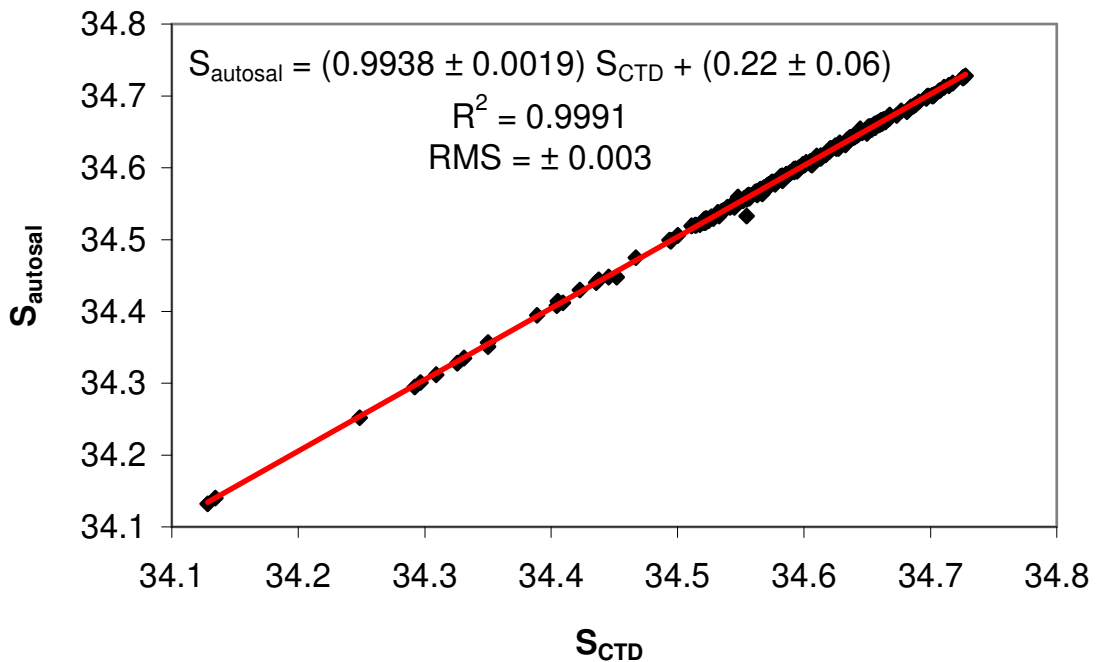

Figure 2.2. Linear regression for the salinity data sets.

2.3.2. Dissolved oxygen sensor

The accuracy and resolution of the oxygen sensor are significantly poorer (relative to the usual variability of the parameter) than for the conductivity or the temperature sensors. This makes the calibration of that sensor to be particularly important. Bottle water samples were analyzed by applying the Winkler methodology, a potentiometric titration method (Culberson and Huang, 1987) where the 0.01N iodate OSIL standards were used for quality control following the recommendations of Culberson et al. (1991) for aliquot determinations. The analysis of replicate samples taken from the same Niskin bottle point to a precision of less than $0.7 \, \mu mol \, kg^{-1}$ for dissolved oxygen.

A preliminary analysis of the first 28 stations revealed important differences between the values measured by the CTD sensor and the Winkler measurements (Fig. 2.3). A comparison with historical data in the Scotia Sea, the differences between the downcasts and upcasts and other calibration tests suggested that the Winkler measurements are correct, so that the problem was with the oxygen sensor of the CTD. In particular it seems that the sensor experienced a hysteresis with pressure during the first part of the cruise, perhaps because it was a new sensor (Fig. 2.4). For the other casts (29-113) the values given by the CTD sensor are more in agreement with the Winkler measurements. In that latter case the calibration of the oxygen sensor data set is straightforward, as a simple linear regression is enough for these values to match the water sample measurements.

The calibration of the station 1-28 data set is more problematic, as it can be inferred from Fig. 2.4, which shows higher and pressure dependent residuals for the first water sample batches. We first tried a regression with an exponential dependence with pressure, in an attempt to eliminate the observed anomalies. After that, two mean square linear regressions were applied to the residuals, one for the data located between 100 and 900 db and another one for pressures greater than 900 db. For the upper range 0-100 db results were not satisfactory and therefore they were discarded; this is not a great loss, since surface oxygen velocities are not as important as at deeper levels for the study of water masses.
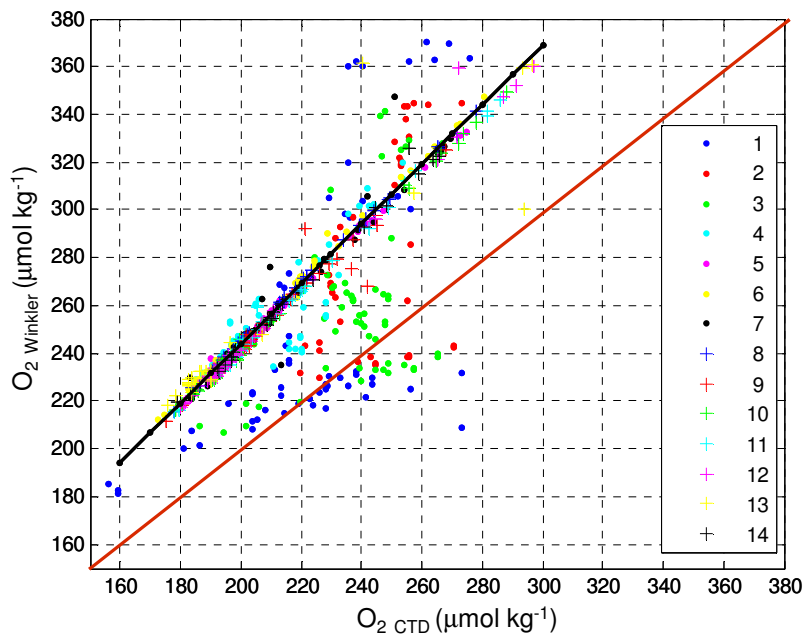
Figure 2.3. *Comparison of dissolved oxygen values given by the oxygen sensor of the CTD and the Winkler results. 'Batchs' are sets of water samples analyzed altogether and that include different casts. The most important deviations correspond to casts from 1 to 28 (batches 1, 2, 3, and part of 4). Figure courtesy of M. Álvarez.*
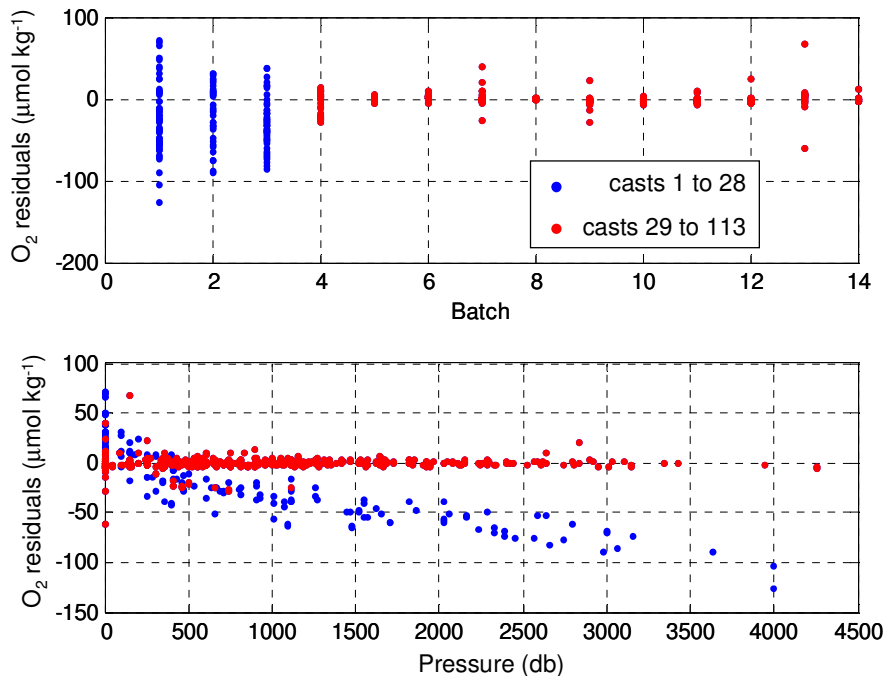
Figure 2.4. *Differences between Winkler and CTD oxygen measurements after applying a common linear regression to the data set (black line in Fig. 2.3). The residuals are smaller and independent on pressure for casts 29-113 (batch>4). The residuals are larger and dependent on pressure for casts 1-28 (batch 1-4).*

The numerical expressions used to calibrate the CTD dissolved oxygen are:

Casts 1 to 28:

$$O_{2\,Winkler} = (381\pm6)p^{(-0.065\pm0.003)} + (1.03\pm0.07)O_{2\,CTD} + (-226\pm17) \; , \; \begin{cases} R^2 = 0.70, \; RMS = 14\,\mu mol\,kg^{-1} \\ 100db \leq p < 900db \\ O_2(\mu mol\,kg^{-1}) \end{cases}$$

$$O_{2\,Winkler} = (381\pm6)p^{(-0.065\pm0.003)} + (0.63\pm0.05)O_{2\,CTD} + (-150\pm11) \; , \; \begin{cases} R^2 = 0.76, \; RMS = 7\,\mu mol\,kg^{-1} \\ p \geq 900db \\ O_2(\mu mol\,kg^{-1}) \end{cases}$$

Casts 29 to 113:

$$O_{2\,Winkler} = (1.237\pm0.007)O_{2\,CTD} + (-3.7\pm1.4) \; , \; \begin{cases} R^2 = 0.99, \; RMS = 4\,\mu mol\,kg^{-1} \\ p(db) \\ O_2(\mu mol\,kg^{-1}) \end{cases}$$

Although the correction has significantly reduced the differences between Winkler and CTD values, the first 28 casts must be taken with caution. When plotting vertical sections of the different parameters and after a water mass analysis we conclude that calibrated oxygen data from casts 1 to 28 are good enough, but not excellent. For instance, no reliable trends can be inferred from the comparison with other cruises in the region. Conversely, the accuracy of the other casts (29-113) and the bottle values of the first casts (1-28) are valid to be used for any purpose.

2.3.3. Phosphate measurements

Samples for phosphate analysis were saved in high-density polyethylene tubes and frozen. They were analyzed at IMEDEA using a Bran-Luebe AA3 autoanalyzer and following standard methods (Hansen and Koroleff, 1999). When comparing the obtained phosphate concentrations with historical data from the WOCE Southern Ocean Atlas (Orsi and Whitworth, 2005), a bias of -0.65 ± 0.15 µmol kg^{-1} was detected and corrected (see Fig. 2.5).
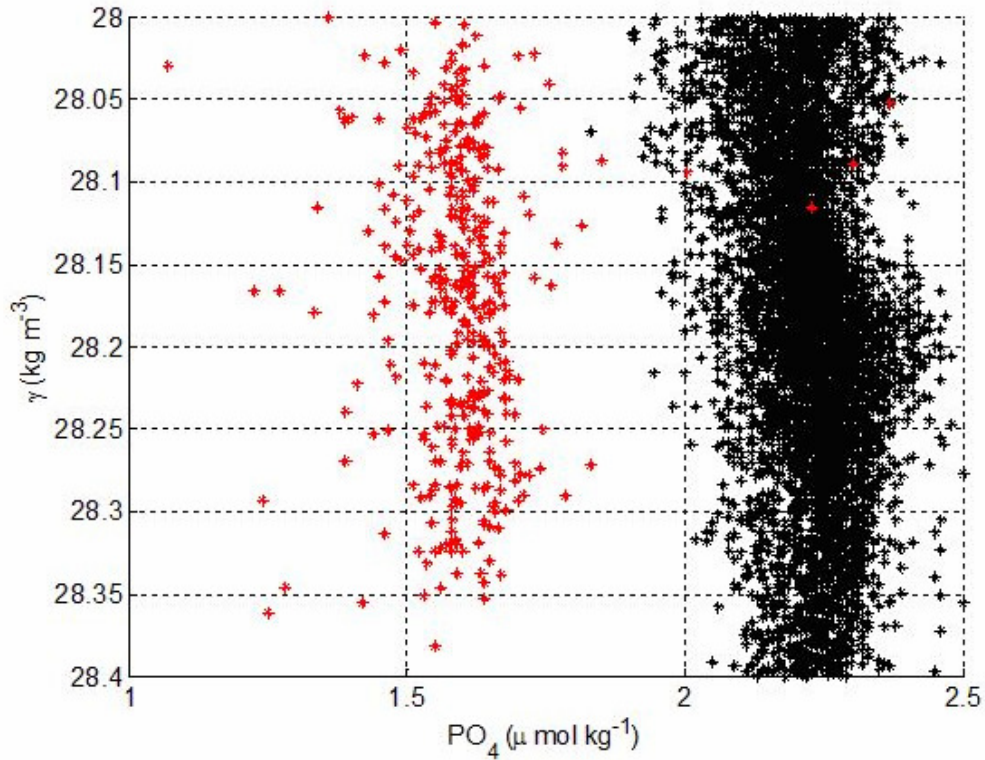
Figure 2.5. *Neutral density vs. phosphate concentrations. ESASSI direct measurements (red) and climatological values (black).*

As part of the nutrient cycle, organic phosphates are re-mineralized by bacteria in the water column: $\Delta(PO_4) = PO_4^* - PO_4$. Broecker et al. (1998) stated that the ratio between the phosphates and oxygen used by bacteria during this process $(\Delta(O_2) = O_2^{saturation} - O_2)$ is approximately constant: $-\dfrac{\Delta(O_2)}{\Delta(PO_4)} = 175$. This allows the estimation of PO_4^*, which can be used as a quasi-conservative tracer of water masses (see e.g. Naveira-Garabato et al., 2002b). We will examine the distribution of PO_4^* later on in this work.

2.4. Neutral density

The basic physical parameters to classify water masses in the ocean are potential temperature, salinity, and neutral density. Salinity is given by the acquisition software of the CTD. The computation of potential temperature (the temperature of a water parcel

when it is adiabatically moved from its original position to the surface) is straightforward; we used the CSIRO MatLAB Seawater Library (Phil Morgan, maintained by Lindsay Pender, 2003) based on the UNESCO algorithms. Instead, some background related to different density variables (Stewart, 2005) is needed to better understand the meaning of neutral density.

The absolute density is difficult to measure out of the environmentally controlled conditions of a laboratory. The use of a density relative to the density of pure water is consequently more extended. The "in situ" density is the density of a water parcel at a certain depth. It is a function of salinity, temperature, and pressure: $\rho = \rho(S, T, p)$. Due to the small changes in sea water, the density anomaly $\sigma(S, T, p) = \rho(S, T, p) - 1000 \text{ kg m}^{-3}$ is more widely used. When it comes to compare water masses, however, it is necessary to reference the density to the same pressure level, in order to avoid density differences due to the effects of pressure. A water parcel can be denser than another parcel of the same water mass just because it is located at a different pressure level. At upper levels the surface pressure can be used as reference, the density then being computed as $\sigma_t = \sigma_t(S, T, p = 0)$. At levels deeper than a few hundred meters, however, the warming due to the effects of pressure is no longer negligible and must be taken into account. Most of this indirect effect of pressure over the density is eliminated by using the potential temperature θ instead of the in situ temperature in the density equation: $\sigma_\theta = \sigma_\theta(S, \theta, p = 0)$. This approximation is the so called potential density and it eliminates not only the direct effect of pressure over the density, but also the indirect effects through temperature. There are still other effects not considered by the definition of σ_θ which can be relevant at depths greater than a thousand meters and for long trajectory water masses. That is the case of the Southern Ocean, where it is convenient to use of a more appropriate definition of density.

When analyzing the properties of the ocean to determine the origin of water masses, it is assumed that the movement of a water parcel located in the interior of the ocean is mostly due to the density distribution. This implies that a water parcel follows a layer of heat (isentropic surface) and salt conservation. This type of surface is complicated to define when mixing processes are involved. In practice, potential density surfaces are often used to trace the path of a water parcel. Thus, from 0 to 500db, the isentropic surfaces are

approximated by the potential density computed relative to the surface (σ_0); from 500 to 1500 db, potential density surfaces referred to 1000 db (σ_1) are used; and so on. This method is obviously better than using σ_0 at all depths, but it is not perfect for a wide range of pressure levels. Jackett and McDougall (1997) published a key paper where they defined a new variable, the neutral density. Neutral density surfaces are the closest approximation to the real isentropic surfaces and are almost globally described. They are based on the interpolation of an extensive data set of CTD profiles and water samples around the globe, all it implemented in a package that can be easily applied to the most extended programming languages. The neutral density is a function of latitude, longitude, pressure, in situ temperature, and salinity, and has an error (derived from the interpolation) smaller than the observational error.

2.5 De-tiding of ADCP measurements

ADCP measurements were taken along the track of the ship shown in Fig. 2.6. In order to evaluate the potential impact of tidal currents on hydrographic data, a yo-yo station located at the shelf break of section S8 (600m depth, see Fig. 2.6) was also performed during the cruise. Figure 2.7 (upper panel) shows the sequence of temperature profiles gathered during 12 hours at that station. There is a clear transition from profiles that are characteristic of shelf waters (more homogeneous) to profiles that reflect the structure of open ocean water masses (with a subsurface temperature minimum characteristic of remnant WW located at 100-200m and the 400-500m temperature maximum characteristic of WDW). These results suggest that WDW could flood and retreat from the slope region with a tidal periodicity. The tidal currents measured at the yo-yo station were as high as 1 m s^{-1} (see Fig. 2.6, lower panel). Similar values were obtained over the shelf-slope of some of the other gaps surveyed during the cruise. This unexpected feature (previous studies had reported weak tidal currents in the region) confirms the crucial role of the abrupt bathymetry in the forcing of the flow. Regarding the data processing, it makes clear that ADCP data must be carefully detided if they have to account only for the subinertial flow.

In order to eliminate tidal currents from the ADCP record, we tested three models: the circum-Antarctic inverse barotropic tidal model (CADA, Padman et al., 2002), the Antarctic
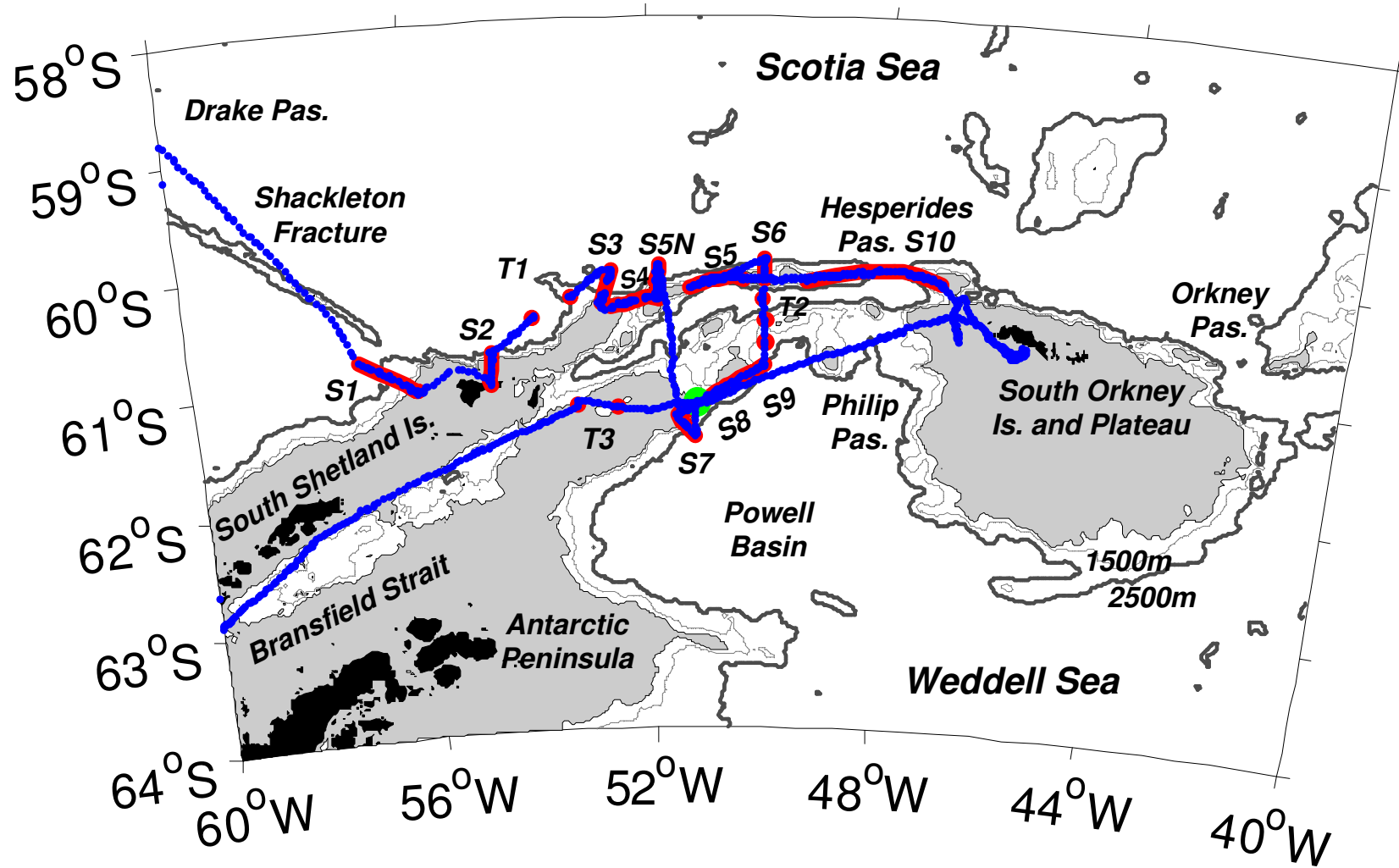
Figure 2.6. ADCP data set along the ship tracking (blue). ESASSI-08 hydrographic sampling (transects and transit casts in red; yo-yo station in green). The bathymetry is from Smith and Sandwell (1997); the areas shallower than 1000m are shaded.
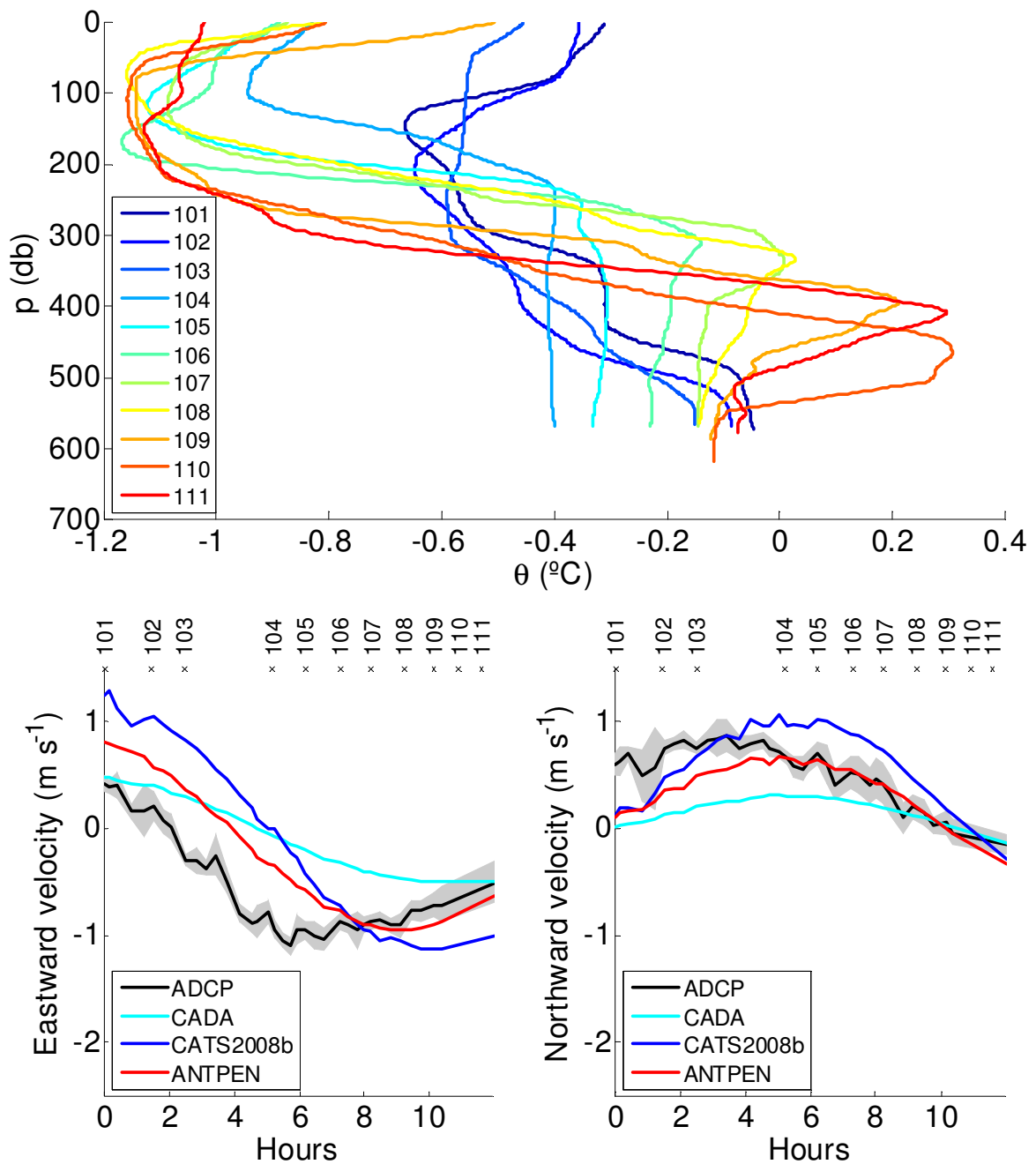
Figure 2.7. *Upper panel: temperature profiles measured at the ESASSI yo-yo station located at the shelf break of section S8 (depth of 600m, see Fig. 2.6 for location). Lower panels: mean velocity components obtained by vertically averaging ADCP data gathered below a depth of 50m (black line, with the standard deviation from the mean value in gray) and tidal velocity components at the same location and time as predicted by three tide models; the time at which the profiles of the upper plot were gathered is marked.*

Peninsula high-resolution tidal forward model (AntPen, a regional version of CATS, Padman et al., 2002), and a recent update of the circum-Antarctic tidal forward model CATS02 (CATS2008b, Padman et al., 2008). The three models gave very similar results at open-sea. At section S8 (Fig. 2.7) the overall structure of the tidal current given by the three models is also similar and consistent with the directions inferred from the hydrographic profiles obtained along the section. However, the magnitude of the currents is rather different among the models, particularly over the shelf break. After a careful checking of the model outputs against sea level data and an exhaustive comparison of the vertical structure of the residual currents against geostrophic currents, the AntPen model was chosen for the de-tiding.
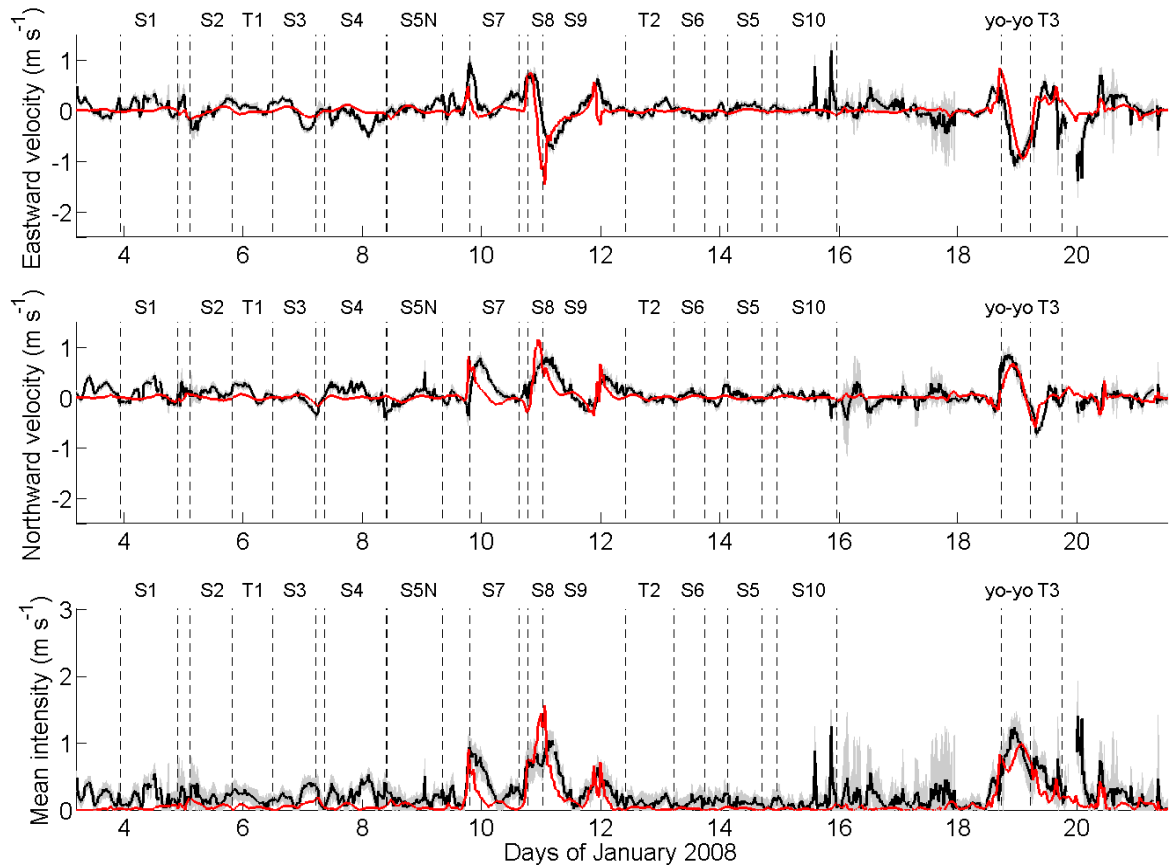
Figure 2.8*. Velocity components and velocity speed estimated by vertically averaging ADCP data gathered below 50m plotted along the track of the ship (black line, with the standard deviation from the mean value in gray). Tidal velocity components and speed at the same location and time as predicted by the AntPen model (red line). The location of the sections plotted in Fig. 2.6 is marked.*

Figure 2.8 shows the mean velocities estimated from ADCP data along the whole track of the ship. The values were obtained averaging the layer below 50m in order to avoid wind-induced effects (tidal currents are essentially barotropic, as inferred from the small deviations from the mean shown in Fig. 2.7). Figure 2.8 also shows the collocated tidal currents given by the AntPen model. Altogether, results suggest that tidal currents are the dominant component of the flow; the highest speeds are observed at the southern flank of the ridge (sections S7, S8 and S9, and at transit T3, from S7 to Elephant Island).

2.6 Baroclinic and barotropic components of the flow

Ocean dynamics is described by the momentum equations for horizontal velocities, and the hypothesis of hydrostatic balance and incompressibility. Because the ocean interior is very approximately in geostrophic balance, the prognostic equations can be reduced to the diagnostic equations giving the longitudinal and latitudinal geostrophic velocities (U_g, V_g).

$$\frac{1}{\rho}\frac{\partial p}{\partial x} = fV_g \quad ; \quad \frac{1}{\rho}\frac{\partial p}{\partial y} = -fU_g \tag{2.1}$$

where p is pressure, ρ is density, f is the Coriolis parameter, g is the gravity acceleration and (x,y) are the horizontal coordinates. Having the stations distributed along cross-slope sections implies that only the cross-section (along-slope) flow can be obtained.

The geostrophic velocity field can be split into two components: the baroclinic and the barotropic components. The first one gives the velocity shear with respect to a reference level and depends on the contribution of horizontal density differences to the pressure gradients appearing in (2.1). In a finite differencing scheme and working with pressure instead of z as vertical coordinate, the cross-section baroclinic component of the geostrophic flow (V_{bc}) in between two (station or grid) points can be expressed simply as the difference between the dynamical height (Φ) measured at these two points divided by the distance between the points (Δx) and the Coriolis parameter (see e.g. Stewart, 2005):

$$V_{bc}\Big|_{ref} = \frac{10}{f}\frac{d\Phi\Big|_{ref}}{dx} \simeq \frac{10}{f}\frac{\Phi(x+\Delta x)\Big|_{ref} - \Phi(x)\Big|_{ref}}{\Delta x} \tag{2.2}$$

A second contribution to the horizontal pressure gradients appearing in (2.1) comes from sea level height anomalies. In this case the pressure differences (and hence the derived geostrophic velocity) will be the same at every depth. This is the barotropic component (V_{bt}) of the flow.

The baroclinic component of the flow can be estimated at any depth where T, S (and hence density) measurements are available. On the other hand, (absolute) velocity measuremets (V_{abs}) are only available for the depth range covered by the ADCP (upper several hundred meters). Thus, if we take advantage of the two independent data sets (density and velocity) covering the upper levels to estimate the barotropic component, this could also be added to the baroclinic component computed below the range of the ADCP in order to recover the absolute velocity at any depth. The important point to be noticed is that the barotropic component is constant with depth, and therefore the value computed at upper levels is the same to be added at lower levels. It is also important to note, however, that since the baroclinic component depends on the reference level used for the geostrophic computations, the barotropic component will also be a function of that level:

$$V_{abs}\left(p\right)=V_{bc}\left(p\right)\big|_{p_{ref}}+V_{bt}\left(p_{ref}\right)$$

(2.3)

In principle, $V_{bt}(p_{ref})$ could be determined using velocity measurements at any single level p, since (2.3) is valid everywhere. In particular, since $V_{bc}(p_{ref})\big|_{pref} = 0$, the barotropic component could be simply made equal to the actual velocity field at the reference level (Chereskin and Trunnell, 1996). The problem is that the noise-to-signal ratio of ADCP data is rather high. Although the nominal accuracy reported in section 2.2 for averaged ADCP profiles was quite acceptable, it neglects for instance the errors derived from inaccuracies in the detiding process. Thus, using (2.3) as it stands would imply transferring the errors of ADCP data to the barotropic component of the flow $V_{bt}(p_{ref})$. It can be shown, for instance, that using (2.3) at different p levels would result in rather different $V_{bt}(p_{ref})$ estimates.

Rudnick (1996) suggested to determine the barotropic component in a different way, namely through the minimization of the expression

$$\overline{\left(V_{abs}\left(p\right)-V_{ADCP}\left(p\right)\right)^{2}}\bigg|_{ADCP\ range}$$

(2.4)

where the overbar could in principle denote vertical averaging over the ADCP range. This is equivalent to make the barotropic component equal to:

$$V_{bt}\left(p_{ref}\right)=\overline{V_{ADCP}\left(p\right)-V_{bc}\left(p\right)|_{p_{ref}}} \tag{2.5}$$

That is, the optimal value of $V_{bt}(p_{ref})$ would be that minimizing the differences between absolute geostrophic velocities and the observed velocities. The basic assumption of Rudnick's method is that the vertical averaging of the differences between ADCP and the baroclinic component is more reliable than the same difference evaluated at a single level, as proposed by Chereskin and Trunnell (1996). This is likely to be the case in the presence of random errors, but it is also clear that the method will not prevent the pouring of vertically correlated ADCP errors into $V_{bt}(p_{ref})$. Another advantage is the independence of the estimated absolute geostrophic velocities with respect to the choice of the reference level, a property that can be easily proved from:

$$V_{abs}\left(p\right)=V_{bc}\left(p\right)|_{p_{ref}}+\overline{V_{ADCP}\left(p\right)-V_{bc}\left(p\right)|_{p_{ref}}} \tag{2.6}$$

A hypothesis implicit in Rudnick's method is that the flow is essentially geostrophic. Because this can only be ensured in the ocean's interior, it is advisable that the averaging domain of (2.4)-(2.6) ignores the surface Ekman layer. For the method to work properly it is also crucial that the a-priori de-tiding of ADCP velocities is as accurate as possible.

Another quality control applied prior to the application of Rudnick's method consisted of checking the consistency between adjacent CTD stations, particularly over the shelf break. A few ESASSI stations located very close to their neighbours (e.g. casts 13, 26, 31, 34, 49, 88) were discarded on the basis of the comparison between the vertical structure of the detided currents and the geostrophic currents between stations. The misfit obtained at the discarded station pairs is due to the lack of synopticity and to the application of the geostrophic balance to structures smaller than the Rossby radius of deformation. Although the lack of synopticity also affects station pairs separated by longer distances, the impact on the mean geostrophic velocity is less important than for stations located very close to each other.

After the estimation of the absolute geostrophic velocity field, computing the cross-section geostrophic flow is, in principle, straightforward. Specific details such as the downwards extrapolation of the velocity field over the slope will be discussed in the next chapters.

CHAPTER 3

GEOSTROPHIC VELOCITY AND TRANSPORTS FROM AN INVERSE MODEL

In this chapter we present an accurate quantification of the transport of volume, heat, and salt through the gaps of the SSR west of the South Orkney Islands. Absolute velocities are first estimated from the CTD casts and ship-borne ADCP data described in the previous chapter. This first estimation is then used as a first guess for the inverse model. The design of the inverse model is presented in section 3.1, while the setup is presented in section 3.2. In section 3.3 we present the application of the model and the analysis of its impact on the first guess of the velocity field. The analysis of the results in terms of the regional circulation (water mass pathways and associated transports) is addressed in chapter 4.

3.1. Inverse model design

Inverse modeling (Wunsch, 1977) allows correcting the velocity field by applying flow conservation equations to a set of neutral density layers of the water column within an enclosed region of the ocean assumed to be in geostrophic balance. For this work, we use the DOBOX model, implemented by Morgan (1994) and tested against a numerical model by McIntosh and Rintoul (1997). The layers considered in this work (see Table 3.1) were chosen basing on the separation between the different water masses present in the region.

3.1.1. Box domain

The domain for the inversion covers from 60˚S (the northern flank of the SSR) to 61.5˚S (the southern flank) and from Elephant Island to 50˚W (Fig. 3.1). The box makes use of six of the hydrographic sections sampled during the ESASSI-08 cruise, with closely spaced stations (1-2 nm over the slope, less than 5 nm elsewhere, 1nm ≡ 1852 m) covering the main passages of the northern and southern flanks of the SSR. The box also uses three transits extending along greater distances but with fewer stations. Direct current measurements from a ship-borne ADCP were collected along all the sections and transits.

Table 3.1*. Inverse model layers and water masses delimited by the chosen neutral density surfaces.*

Layer	Upper interfaces γ^n (kg m^{-3})	Water mass
1	surface	AASW
2	27.95	
3	28.0	LCDW/AASW
4	28.06	
5	28.1	LCDW/WDW
6	28.16	
7	28.23	
8	28.27	WSDW
9	28.31	

The most important gaps crossed by the box model are the two westernmost gaps of the southern flank (2100m and 2500m depth, sections S8 and S9, respectively), the Hesperides Trough (4000m depth, northern part of transit T2), and the two westernmost gaps of the northern flank (1700m and 1300m depth, sections S4 and S5, respectively). The ESASSI-08 cruise did not cover the stretch between Elephant and Clarence Islands, and from Clarence Island to the beginning of transit T3. The closure of the box at this site is addressed in the next section.

3.1.2. Closure of the box

The last hydrographic station of the ESASSI-08 cruise (cast 113, see Fig. 3.1) is located about 80 km to the E-SE of Elephant Island. No ADCP data were recorded between that cast and Elephant Island. Some inflow from the Bransfield Strait has been reported to enter the selected domain through that gap (López et al., 1999) and therefore it must be included in the conservation equations before the inversion of the model equations. The estimation of the property transports across that transect will be based on historical data and on previous results obtained by other authors.
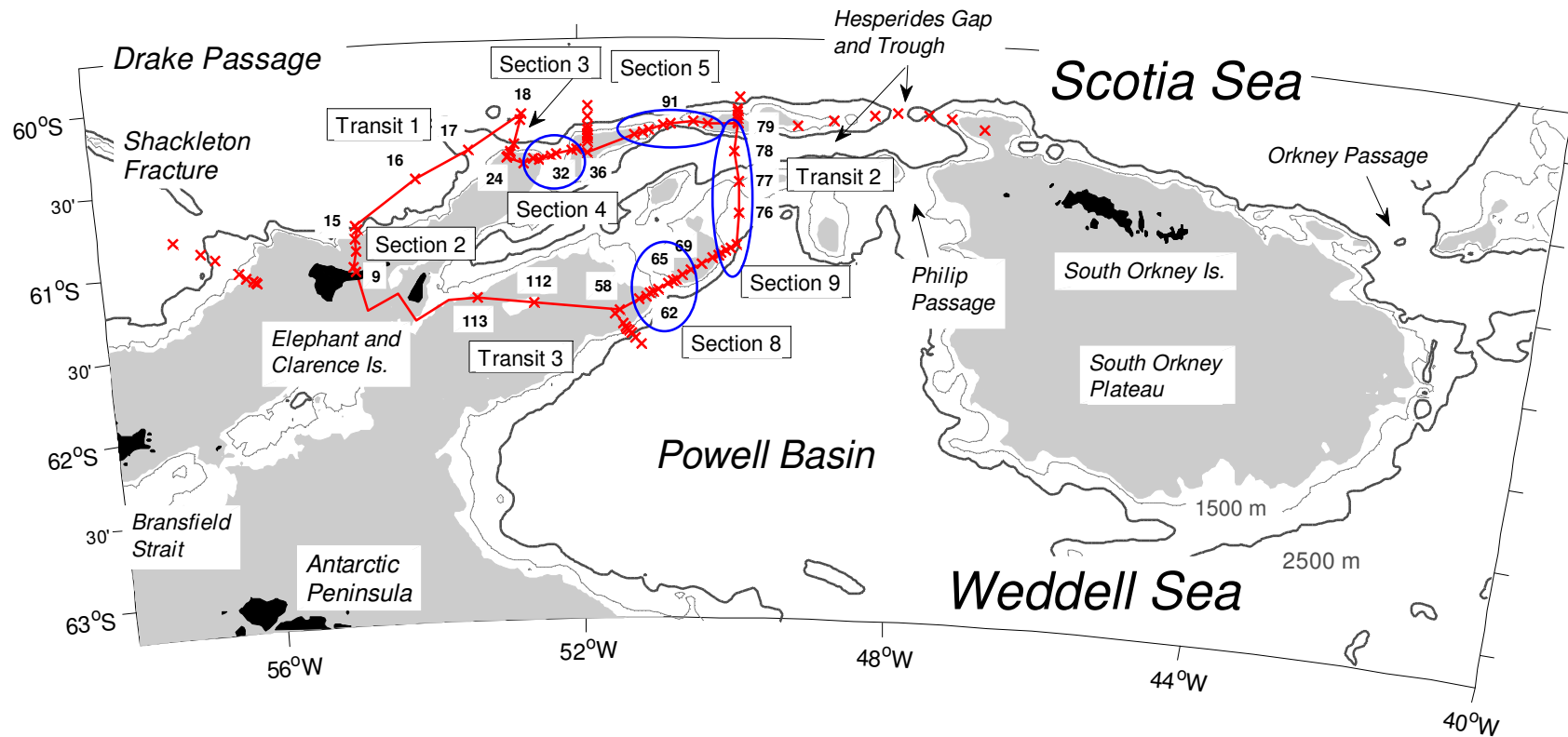
Figure 3.1. *ESASSI-08 hydrographic stations (red crosses) in the region. The stations constituting the model box are linked; only the most relevant are numbered. The bathymetry is from Smith and Sandwell (1997); the areas shallower than 1000m are shaded. The topographical gaps crossed by the boundaries of the model domain have been encircled: one of them is in the southern flank of the South Scotia Ridge (section S8) and two in the northern flank (sections S4 and S5). The eastern boundary of the box (transit T2) runs from the southern flank to the northern flank.*

A relevant contribution to the knowledge of the missing transect comes from the hydrographic data collected during the ECOANTAR-94 cruise carried out in January 1994. That is, the same month as the ESASSI-08 cruise, though 14 years earlier. During ECOANTAR-94 the whole eastern basin of the Bransfield Strait was covered with a regular distribution of stations spaced 20 km (López et al., 1999). Those hydrographic data and the baroclinic component of the geostrophic velocities computed with respect to the deepest common level enable the tracking of the water masses exiting the Bransfield Strait to the east, since they cover most of the gap of the ESASSI-08 cruise. The barotropic component of the current cannot be estimated from ECOANTAR-94 data, due to the absence of direct current measurements. Instead, absolute velocities were estimated from near surface velocities recorded by drifters and interpolated over the ECOANTAR-94station pairs. The analysis of the data set of historical and ADELIE-07 drifters provided by Thompson et al. (2009) shows a negligible barotropic component compared with the geostrophic shear.

The ECOANTAR-94 stations cover most of the missing transect, but there is still a small uncovered segment shallower than 500m close to the southeast coast of Elephant Island. The hypothesis we make is that the westward flow observed at the northern coast of the island (casts 9-10, section S2) is a coastal current surrounding Elephant Island anti-clockwise, so that the volume transport at the southern coast should be equal to the transport observed to the north of the island.

A previous study of the ECOANTAR-94 cruise (López et al., 1999) estimated the geostrophic flow across the missing transect in approximately 0.5 Sv, of which 0.4 Sv would enter the box domain between Elephant and Clarence Islands and 0.1 Sv would enter the box to the southeast of Clarence. That calculation is based on the hypothesis of a common level of no motion at 500m depth. A re-calculation down to the bottom and the inclusion of the coastal flow around Elephant Island increase the net volume transport up to 1.4 Sv (Table 3.2). The lack of synopticity between the drifters and ECOANTAR-94 data as well as the inherent temporal variability of the Bransfield currents (Savidge and Amft, 2009) suggest considering transport uncertainties of the same order as the quoted absolute values.

Table 3.2. *Estimated property transports across the missing transect needed for the closure of the box domain.*

Layer	Volume transport (Sv)	$\Delta\theta$ transport (˚C Sv)	ΔS transport (Sv)
1	0.527	0.249	-0.099
2	0.121	-0.004	-0.010
3	0.221	-0.036	-0.008
4	0.183	-0.027	-0.002
5	0.236	-0.013	0.005
6	0.129	0.007	0.007
7	0	0	0
8	0	0	0
9	0	0	0
Full depth	1.417	0.176	-0.106

3.1.3. Water mass distribution

The vertical distribution of temperature (Fig. 3.2) shows the main water masses along the box. The AASW and AABW are separated by the relative temperature maximum of the regional Circumpolar Deep Water: the WDW found below the 28.1 kg m^{-3} isopycnal over most of the box domain and the LCDW ($\theta_{max} > 1$ºC, $S_{max} > 34.7$) found below the 27.95 / 28.0 kg m^{-3} isopycnals at the northernmost side of the box (casts 18 and19, section S3) delimiting the Southern Boundary of the ACC. The temperatures close to the freezing point ($\theta \approx -1.9$ºC) and the high salinities characterizing recently formed SW are not observed in the box.

The surface layer ($\gamma^n < 27.95$ kg m^{-3}) occupies the upper 400m north of Elephant Island (section S2). Its lower interface rises along the rest of the box, almost outcropping over the shelves of both flanks of the ridge (cast 36, between sections S4 and S5 in the northern flank and cast 69, between sections S8 and S9 in the southern flank, Fig. 3.2). The temperature of the surface layer ranges from -1ºC in the southern flank to 0.3ºC in the northern flank. The warmest surface water ($\theta \approx 0.7$ºC) overrides the Southern Boundary of the ACC.
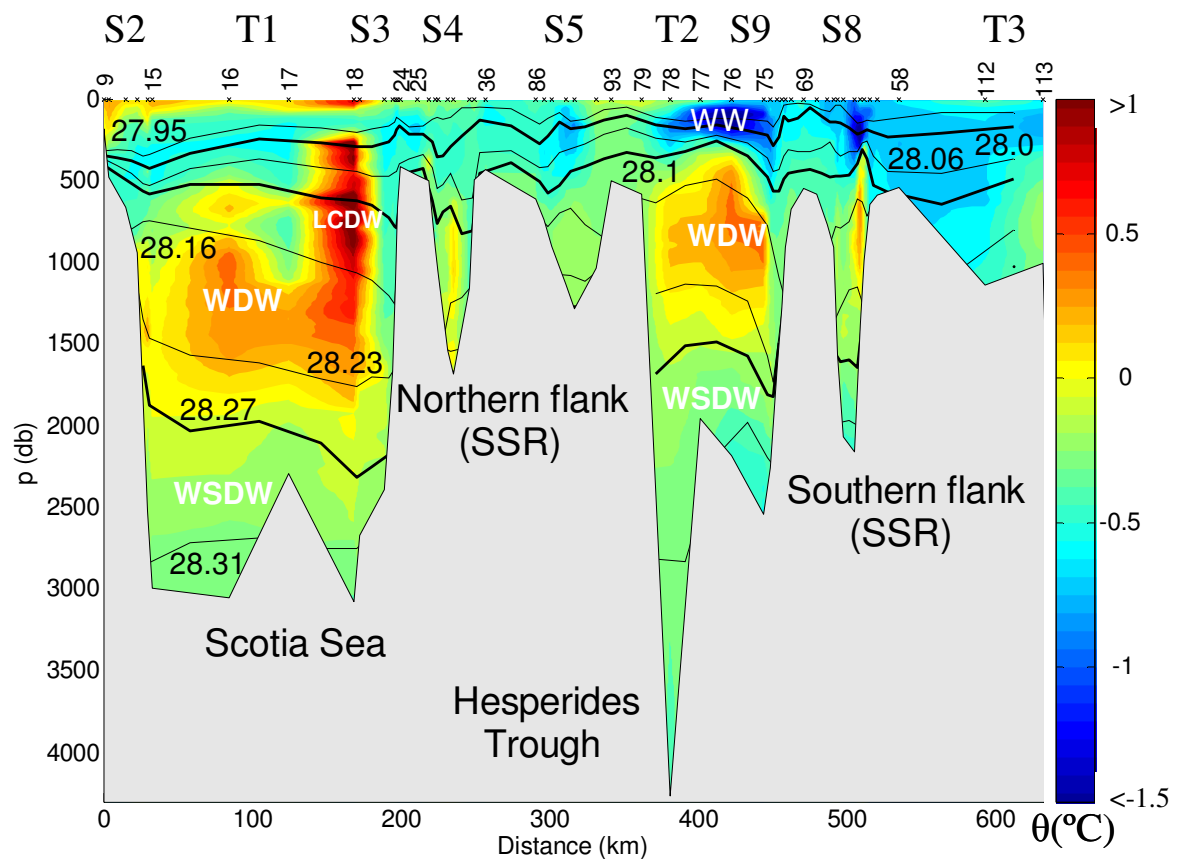
Figure 3.2. *Vertical distribution of potential temperature along the boundaries of the model. Neutral density interfaces delimiting the model layers (see Table 3.1) are drawn in black; the thicker lines correspond to 28.00, 28.10, and 28.27 kg m^{-3}.*

The subsurface layers (27.95–28.00–28.06 kg m^{-3}) are everywhere above the topographic barriers of the region, allowing the free overflowing of AASW. The coldest water mass corresponds to WW, characterized by a temperature minimum located between the 27.95 and 28.0 kg m^{-3} interfaces. Its lowest value (θ = -1.6ºC) is found above the core of the WDW entering the southern flank of the ridge from the Powell Basin (sampled in section S8 and transit T2).

Denser waters are more constrained by the bathymetry. WDW (28.1 - 28.27 kg m^{-3}) is found between 300 and 1500m at the southern flank (section S8) and in the Hesperides Trough (transit T2), and between 500 and about 2000m in the Scotia Sea (transit T1). Its temperature-salinity maximum core ($\theta \leq$ 0.5ºC, S < 34.7) lies just below the 28.16 kg m^{-3} isopycnal. The gaps of the northern flank of the ridge do not show any WDW core: the shallower of the northern gaps (section S5) is filled with an homogeneous, cold water mass

($\theta < 0$ºC), whereas the warmer core of the western gap (section S4) is lighter than the 28.16 kg m^{-3} isopycnal.

The bottom water mass components ($\gamma^n > 28.27$ kg m^{-3}) observed in the Scotia Sea and in the Weddell Sea are not directly connected through the northern gaps of the box domain (sections S4 and S5), but they are through the Hesperides Passage (out of the box domain, see Fig. 3.1). That 3100m gap is the deepest gap to the west of the South Orkney Islands and connects the Hesperides Trough with the Scotia Sea.

The properties observed at the southern and northern flanks of the ridge and at the southwestern sector of the box (transit T3) are rather different because the complex topography allows the confluence of different open-sea and shelf water masses. In spite of that, the property patterns along 50ºW (transit T2, including the Hesperides Trough) seems to be rather stable in time, because similar temperature and salinity distributions were measured in 1975 (Deacon and Foster, 1977).

3.2. Inverse model setup

The set of linear equations used for the inversion accounts for the geostrophic flow across the boundaries of the domain and for internal diapycnal mixing. At the time of the cruise, surface winds (gathered from the NCEP Reanalysis, NOAA/OAR/ESRL PSD, http://www.esrl.noaa.gov/psd) were predominantly eastward over the region, with values around 6 m s^{-1}. They would result in a net northward flow of about 0.1 Sv for an Ekman layer of 50m depth. These values are much smaller than the uncertainties derived from the measurement errors and from the temporal variability inherent to the surface of the ocean, then concluding that the Ekman transport is irrelevant for the model inversion.

In the vertical, the conservation is applied to the full-depth and to the layers delimited by the neutral density interfaces (McDougall, 1987) selected for the inversion (Table 3.1). Each of the four shallower layers covers about 6% of the lateral area, while each of the five deeper layers covers about 15% (Fig. 3.2). Not only the conservation of volume, but also the conservation of potential temperature and salinity are included in the system,

increasing the number of equations (3 properties x 10 layers) but not reducing the indetermination of the system (78 unknowns from 54 station pairs and 3 x 8 diapycnal mixing effective velocities) due to the increase in the number of diapycnal mixing unknowns (Wunsch, 1996; Sloyan and Rintoul, 2000). In order to avoid mathematical problems when inverting the matrix equation, the conservation equations for heat and salt are applied to potential temperature and salinity anomalies relative to the local mean values ($\Delta\theta = \theta - \overline{\theta}$, $\Delta S = S - \overline{S}$, Jullion et al., 2010), instead of to absolute values (θ, S) (McDougall, 1991).

Every equation (i) of the system has the following expression:

$$
\sum_{j=1}^{J} \Delta d_j \delta_j \underset{P_{\text{lower limit of k layer}}}{\overset{P_{\text{upper limit of k layer}}}{\int}} C_{ij} \underbrace{\left(\left[V_{bc}(p)\big|_{ref} \right]_{ij} + \left[V_{bt}(p_{ref}) \right]_j + \left[\Delta V_{bt}(p_{ref}) \right]_j \right)}_{\text{Vtotal}_{ij}} dp +
$$

$$
\underbrace{}_{\text{lateral flow}}
$$

$$
+ w_{\text{k+1 interface}} \overbrace{\sum_{j=1}^{J} \Delta d_j \delta_j C_{\text{k+1 interface},j}}^{\text{inflow into the k layer}} - w_{\text{k interface}} \overbrace{\sum_{j=1}^{J} \Delta d_j \delta_j C_{\text{k interface},j}}^{\text{outflow from the k layer}} = 0
$$

$$
\underbrace{}_{\text{vertical flow}}
$$

(3.1)

The inputs into the system are the property concentrations (C) at every layer (i) and station pair (j) and the first guess of the velocity field $\left(\left[V_{bc}(p)\big|_{ref} \right]_{ij} + \left[V_{bt}(p_{ref}) \right]_j \right)$. The outputs are the correction to the barotropic velocity at every station pair $\left(\left[\Delta V_{bt}(p_{ref}) \right]_j \right)$ and the estimated diapycnal mixing velocities (w) at the interfaces between layers.

In a matrix notation the equation system to be inverted (3.1) can be written as follows:

$$
\left. \begin{array}{l} Ax \simeq b \rightarrow y = Ax \underbrace{-b}_{n} \\ A \equiv USV^{T} \end{array} \right\} \rightarrow x \simeq VS^{-1}U^{T}b
$$

(3.2)

where A represents the matrix of property concentrations per unit area, x is the vector of unknowns, Ax is the misfit to the property balance, $n = -b$ is the vector of the net property transports at each layer, and y is the vector of flow residuals. The system can be solved through a Singular Value Decomposition (Golub and Kahan, 1965) of matrix A, as shown in (3.2), where U and V are orthonormal eigenvectors and S is the diagonal matrix of eigenvalues.

3.3. Velocity field and imbalances before and after the inversion

3.3.1. First guess of the velocity field and initial imbalances

Previous studies have shown that the assumption of a common level of no motion is not appropriate in the region (Gordon et al., 2001; Naveira-Garabato et al., 2002b; Franco et al., 2007). In many cases the barotropic component is as important as the baroclinic one, and inverse models can lead to solutions far from reality if a first guess of the barotropic flow is not considered (Naveira-Garabato et al., 2003). The geostrophic shear with respect to the deepest common level and the de-tided ADCP profiles (AntPen, Padman et al., 2002) of cross-section velocity are shown in the upper panels of Fig. 3.3. In order to obtain an estimation of the barotropic velocity and then of the first guess of the velocity field (third panel, Fig. 3.3), we applied the Rudnick's method (Rudnick, 1996) described in chapter 2 to the geostrophic shear and the mean ADCP profile at every station pair.

The residuals of the fitting are considered as a measure of the error of the barotropic velocity at every station pair. The obtained errors are bigger than ±0.02 m s^{-1} everywhere, with extreme values of about ±0.11 m s^{-1} for some narrow jets over the slope (Fig. 3.3, lower panel). These errors are mostly due to the noise in the ADCP data and they are not reduced by discarding the Ekman layer (see lower panel in Fig. 3.3). The smallest errors are obtained at the gaps of the northern flank, at the Hesperides Trough, and at the Southern Boundary of the ACC. Regarding diapycnal velocities, they are initially set to zero, and their uncertainty is set to ~10^{-5} m s^{-1}, the maximum values observed for mixing processes in the ocean (Orsi et al., 1999).
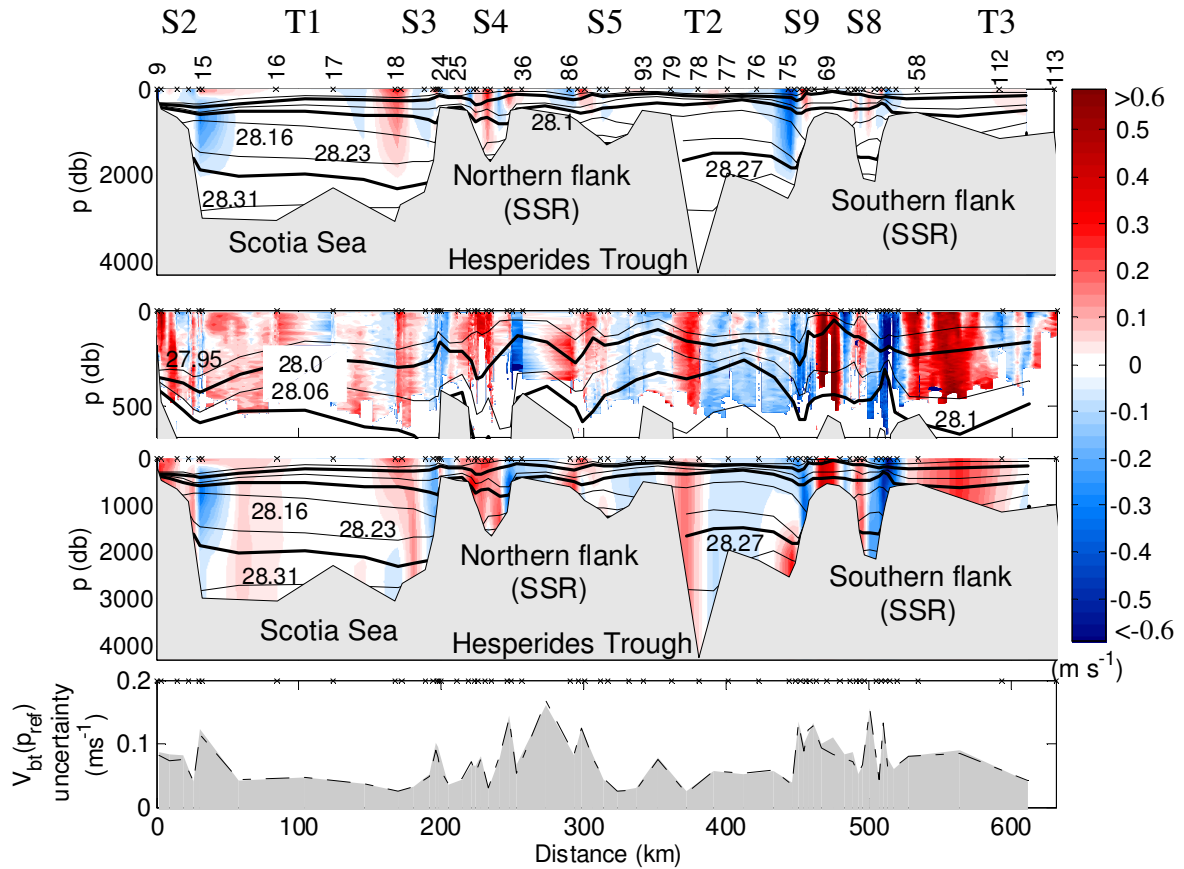
Figure 3.3. *First guess used to initialize the inverse model: the baroclinic component of the geostrophic field relative to the deepest common level (upper panel), the cross-section de-tided ADCP velocity (second panel) and the total geostrophic velocity field before the inversion (third panel). The black lines are the neutral density model interfaces (the thicker ones correspond to 28.00, 28.10, and 28.27 kg m⁻³). Positive values denote outward velocities from the box domain. The lower panel shows the uncertainty of the first guess when the ageostrophic terms inferred from the surface winds are removed (thin line) and when they are not (shaded area).*

The transports calculated from the first guess show a clear imbalance (Fig. 3.4): for single layers the mean residuals are of about 3 Sv, amounting to 25 Sv for the full depth. That big imbalance, introduced by the barotropic component, justifies the use of the inverse method to refine the velocities. The potential temperature and salinity anomalies show the largest imbalance in the shallower and bottom layers. Potential temperature anomalies show the largest imbalance at subsurface levels (layer 3) and close to the core of WDW (layer 6). Salinity anomalies show the maximum imbalance at shallow and bottom layers (Fig. 3.4).
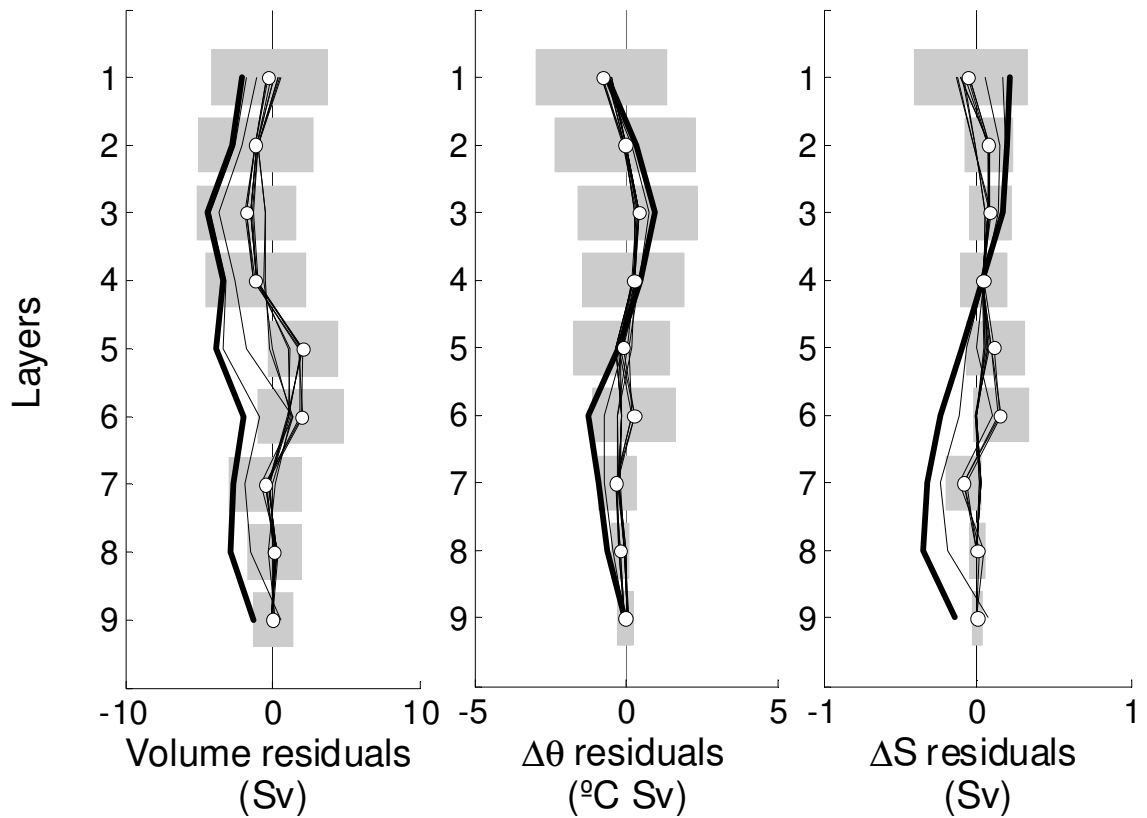
Figure 3.4. *Residuals before and after the inversion. The dash-dot line represents the initial residuals, thin lines denote the residuals for ranks 1 to 12, with the selected rank (5) marked with white circles. The a posteriori errors for rank=5 are shown as gray areas.*

Before the model inversion, the uncertainty of the first guess must be determined and introduced in the equation system. Errors in the volume transport must include the velocity observational errors ($\varepsilon(V_{bt})$ and $\varepsilon(w)$), but also the temporal variability of each layer $\varepsilon(n)$. Determining the error of every layer for a box that covers a small region with a complex topography, and where shallow and deep locations are connected by steep slopes, is not straightforward. The errors assigned to every layer and to the full depth should be close to the initial imbalances, that is, about 3 Sv for each layer, with a minimum of 1.2 Sv for the bottom layer and a maximum of 4.5 Sv for the subsurface layers. The volume errors assigned to each layer are presented in Table 3.3, altogether with the layer mean values of potential temperature and salinity.

Table 3.3. A priori errors for the layers of the conservation system.

Layer	$\varepsilon(n)$ (Sv)	$\overline{\theta} \pm \Delta\theta$ (°C)	$\overline{S} \pm \Delta S$
1	4.0	-0.464 ± 0.267	34.407 ± 0.045
2	4.0	-0.579 ± 0.293	34.466 ± 0.019
3	3.5	-0.521 ± 0.282	34.511 ± 0.020
4	3.5	-0.392 ± 0.237	34.548 ± 0.022
5	3.5	-0.229 ± 0.230	34.586 ± 0.027
6	3.5	-0.018 ± 0.200	34.634 ± 0.025
7	2.5	-0.058 ± 0.124	34.653 ± 0.022
8	2	-0.195 ± 0.072	34.656 ± 0.012
9	1.5	-0.333 ± 0.084	34.655 ± 0.009
Full depth	5	-0.292 ± 0.158	34.564 ± 0.050

The way of introducing the uncertainties of the first guess in the equation system is double weighting the matrix (Wunsch, 1996). In a matrix notation the new equation system to be inverted can be written as follows:

$$\left. \begin{array}{r} W_R \left(AW_C W_C^{-1} x \simeq b \right) \\ \left(W_R AW_C \right) \equiv USV^T \end{array} \right\} \rightarrow \left(W_C^{-1} x \right) \simeq VS^{-1}U^T \left(W_R b \right) \tag{3.3}$$

where W_R and W_C are the row and column weighting matrices, respectively. By introducing W_R we can assign more or less confidence to the conservation in every layer, whereas by introducing W_C we constrain the variability of the velocity field. Both matrices also include a normalizing factor. At W_R this factor is chosen to be twice the standard deviation of the layer mean value of potential temperature and salinity instead of by their means (Table 3.3), in order to avoid possible unrealistic extremes when the mean value for the layer and for the box are similar (Jullion et al., 2010). At W_C this factor accounts for the area of the station pair or the k-interface. The expressions of the weighting matrices can be written as:

$$(W_R)_{ii} = \left\{ \begin{array}{l} \left. \left(\dfrac{1}{\varepsilon(n)} \right) \right\|_{\text{i layer}} \\[2ex] \left. \left(\dfrac{1}{\varepsilon(n)} \dfrac{1}{2\,\Delta\theta} \right) \right\|_{\text{i } \theta\text{-layer}} \\[2ex] \left. \left(\dfrac{1}{\varepsilon(n)} \dfrac{1}{2\,\Delta S} \right) \right\|_{\text{i S-layer}} \end{array} \right. ; \quad (W_C)_{jj} = \left\{ \begin{array}{l} \left. \left(\dfrac{\sqrt{\varepsilon(V_{bt}(p_{ref}))}}{\sqrt{area}} \right) \right\|_{\text{j station pair}} \\[2ex] \left. \left(\dfrac{\sqrt{\varepsilon(w)}}{\sqrt{area}} \right) \right\|_{\text{k interface}} \\[2ex] \left. \left(\dfrac{\sqrt{\varepsilon(w)}}{\sqrt{\bar{\theta}\ area}} \right) \right\|_{\text{k } \theta\text{-interface}} \\[2ex] \left. \left(\dfrac{\sqrt{\varepsilon(w)}}{\sqrt{\bar{S}\ area}} \right) \right\|_{\text{k S-interface}} \end{array} \right. \tag{3.4}$$

The uncertainty of the solution (referred to as 'a posteriori errors') can also be estimated. The method followed here is based on the Gauss-Markov statistical procedure for inverse models developed by Wunsch (1996). The expressions used to compute the final variances of the velocity field (P_{xx}) and net property flow at each layer (P_{nn}) are functions of the initial variances (R_{xx} and R_{nn}):

$$\begin{aligned} P_{xx} &= R_{xx} - R_{xx}\ A^T\ ZZ\ A\ R_{xx} \\ P_{nn} &= \left(I - A\ R_{xx}\ A^T\ ZZ \right) R_{nn} \left(I - A\ R_{xx}\ A^T\ ZZ \right) \end{aligned} \tag{3.5}$$

where

$$R_{xx} = \left\{ \begin{array}{l} \left(\varepsilon(V_{bt}) \right)^2 \\ \left(\varepsilon(w) \right)^2 \end{array} \right. , \quad R_{nn} = \left(\varepsilon(n) \right)^2$$

$$R_{yy} = \left\langle yy^T \right\rangle = A\ R_{xx}\ A^T + R_{nn} ; \quad ZZ \equiv R_{yy}^{-1} \tag{3.6}$$

3.3.2. Final imbalances and absolute velocity field

The output from the inversion is the correction to the barotropic component of the velocity, the transports across the walls of the box, and the diapycnal exchanges. The potential temperature and salinity anomalies used to compute the heat- ('enthalpy' for non-zero

advection, Ganachaud and Wunsch, 2000) and salt-anomaly transports are estimated with respect to the mean values of potential temperature $\left(\overline{\theta} = -0.29\text{°C}\right)$ and salinity $\left(\overline{S} = 34.56\right)$ along the box (full depth, Table 3.3).

Perfect conservation would be reached for the mathematical or maximum rank of the solution (rank = 30 in our case), but mathematical instabilities (rank $\geq$ 27, for the residual norms in the Levenberg-Marquardt plot of Lawson and Hanson, 1974) and physical unrealistic results are obtained when reaching the complete solution. The effective rank (Wunsch, 1996) is a compromise between velocity changes and conservation forcing, and is usually much smaller than the mathematical rank. The impact on the residuals for the first 12 ranks of the solution is presented in Fig. 3.4. The first three eigenvalues are essential to reach robust residuals for all properties. On the other hand, the barotropic velocities change more than their a priori errors for rank $\geq$ 9, and diapycnal mixing effective velocities become sensitive to the rank for rank $\geq$ 6. Therefore we selected the solution corresponding to rank 5; this choice explains 78% of the initial variability, keeps final barotropic velocities inside their initial error margins, and final residuals are not statistically different from zero (they fall within the a posteriori errors). The full-depth residuals are reduced after the inversion from -25 to -0.6 ± 1.1 Sv, and from -9 to -2 ± 5 TW, whereas the residuals for the salt content remain similar (-0.5 ·10^6 to (0.3 ± 0.5)·10^6 kg s^{-1}). The net balance involves the lateral flow, the contribution from the extrapolation to the bottom of the velocity at the deepest common level, and a small contribution from the vertical mixing (volume advection, heat- and salt-anomaly advection-diffusion, Table 3.4). There is some mixing in the middle layers, with effective velocities of the order of ~10^{-6} m s^{-1}. Note that heat and salt diffusion are obtained at the interface that separates LCDW/WDW from WSDW. Some salt exchange is also obtained at upper layers.

The sensitivity of the velocity field resulting from the inversion was tested by changing independently some features of the model setup (Fig. 3.5), such as imposing no fluxes through the missing transect, setting the diapycnal mixing to zero or requiring conservation of only one of the three variables. From all the cases, the barotropic velocity changed more than the a priori error only in a few stations when volume or salinity conservation alone was requested (upper panel, Fig. 3.5). The differences between the sensitivity tests are

much smaller than the velocity correction except in a few locations, so that the overall impact on the velocity field across the walls of the box is small (middle panel, Fig. 3.5). In any case the initial imbalance was reduced by more than 90%.

Particular attention was paid to the impact of the bottom extrapolation (lower panel, Fig. 3.5). The bigger bottom triangle areas are found along the transits of the box domain, where the station separation is larger. Transit T1 is not very relevant for the quantification of the northward exportations, and in Transit T3 the differences between extrapolating or not the velocities fall within the associated uncertainties. Transit T2 deserves more attention, because it crosses the Hesperides Trough and because at the northern station pair (casts 79-78) the area of the bottom triangle is as large as the area of the above levels altogether. After testing different options we decided that the best one was the extrapolation of the velocity obtained at the deepest common level down to the bottom. The reason is that the barotropic component is higher than the baroclinic component in that station pair: the shear is important in the first 200m, where it ranges from 0.10 to 0.16 m s^{-1}, but below that level the shear is negligible as derived from our data (down to 600m) and supported by other data sets such as the DOVETAIL (1997) 48ºW section, which shows rather constant Lower-ADCP values down to the bottom.

Table 3.4. *Diapycnal mixing transports for the selected (rank=5) solution.*

Layer	Diapycnal volume transport (10^6 m^3 s^{-1})	Diapycnal $\Delta\theta$ transport (10^{12} W)	Diapycnal ΔS transport (10^6 kg s^{-1})
1	0.00 ± 0.12	0.00 ± 0.10	0.002 ± 0.014
2	-0.01 ± 0.17	0.00 ± 0.15	-0.002 ± 0.015
3	0.01 ± 0.17	0.00 ± 0.13	0.000 ± 0.008
4	-0.02 ± 0.16	0.00 ± 0.07	0.000 ± 0.003
5	0.04 ± 0.15	0.00 ± 0.07	0.001 ± 0.006
6	-0.02 ± 0.12	0.00 ± 0.12	0.002 ± 0.009
7	0.00 ± 0.08	-0.03 ± 0.11	-0.005 ± 0.009
8	0.00 ± 0.06	0.02 ± 0.05	0.007 ± 0.007
9	0.00 ± 0.04	0.00 ± 0.01	-0.005 ± 0.004
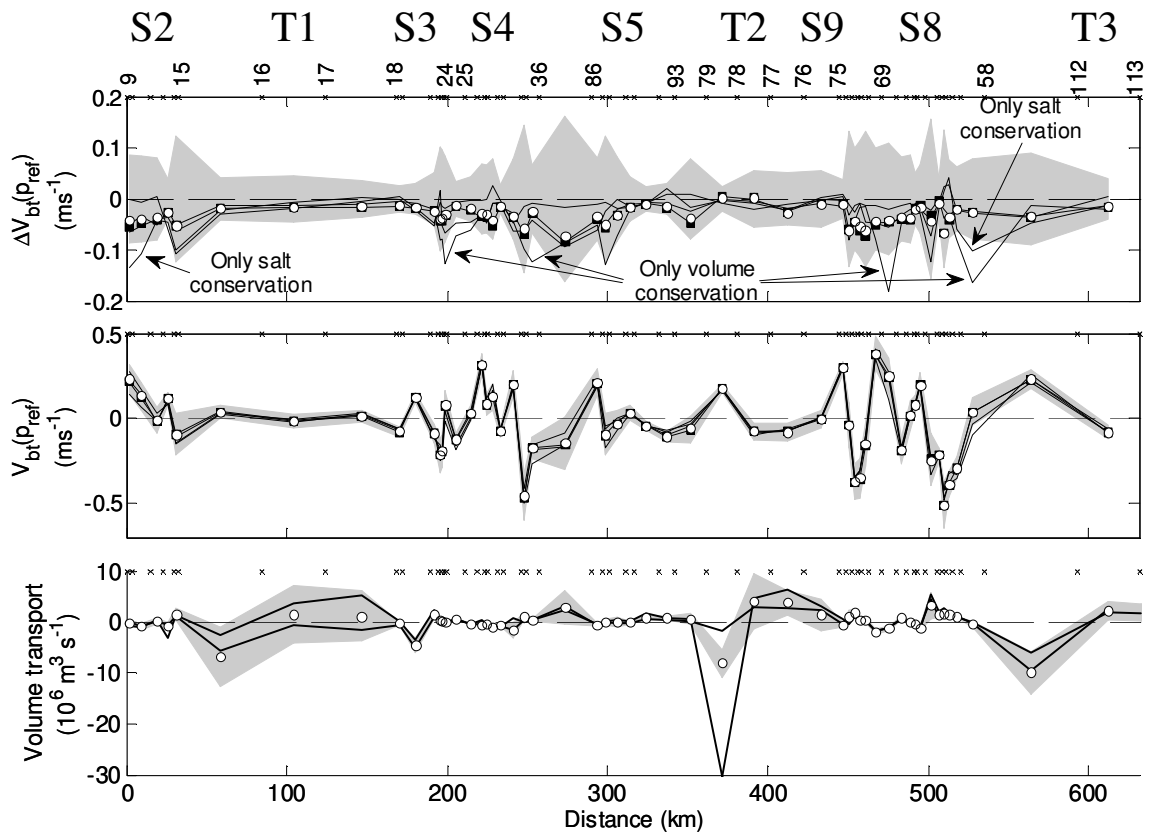
Figure 3.5*. Correction to the barotropic component, with the initial uncertainty in gray (white circles, upper panel) and barotropic velocities obtained after the inversion with the a posteriori error at rank=5 in gray (white circles, lower panel). When no fluxes are assumed through the missing transect (southwest corner of the box) the obtained correction is denoted by black squares. The results of other sensitivity tests (no diapycnal mixing, only volume conservation, only potential temperature anomaly conservation, and only salinity anomaly conservation) are indicated by thin lines. The lower panel shows the full-depth volume transport obtained when applying the bottom triangle velocity extrapolation (white circles) within the a posteriori error in gray. The dash-dot line corresponds to the transport obtained with no extrapolation, and the solid line corresponds to a method of extrapolation that interpolates the temperature and salinity profiles along the hypotenuse of the bottom triangle and infers the geostrophic shear.*

The correction of the barotropic field by the inverse model represents a mean shift of -0.03 m s^{-1} with respect to the first guess (top panel of Fig. 3.6) and compensates most of the previous imbalance. The maximum velocity correction are the -0.07 m s^{-1} obtained over the shelf that separates the two westernmost gaps of the northern flank (sections S4 and S5) and the -0.06 m s^{-1} correction to the inflow through section S8. The barotropic velocities and the absolute velocity field for the selected rank of the solution are shown in the middle and lower panels of Fig. 3.6.
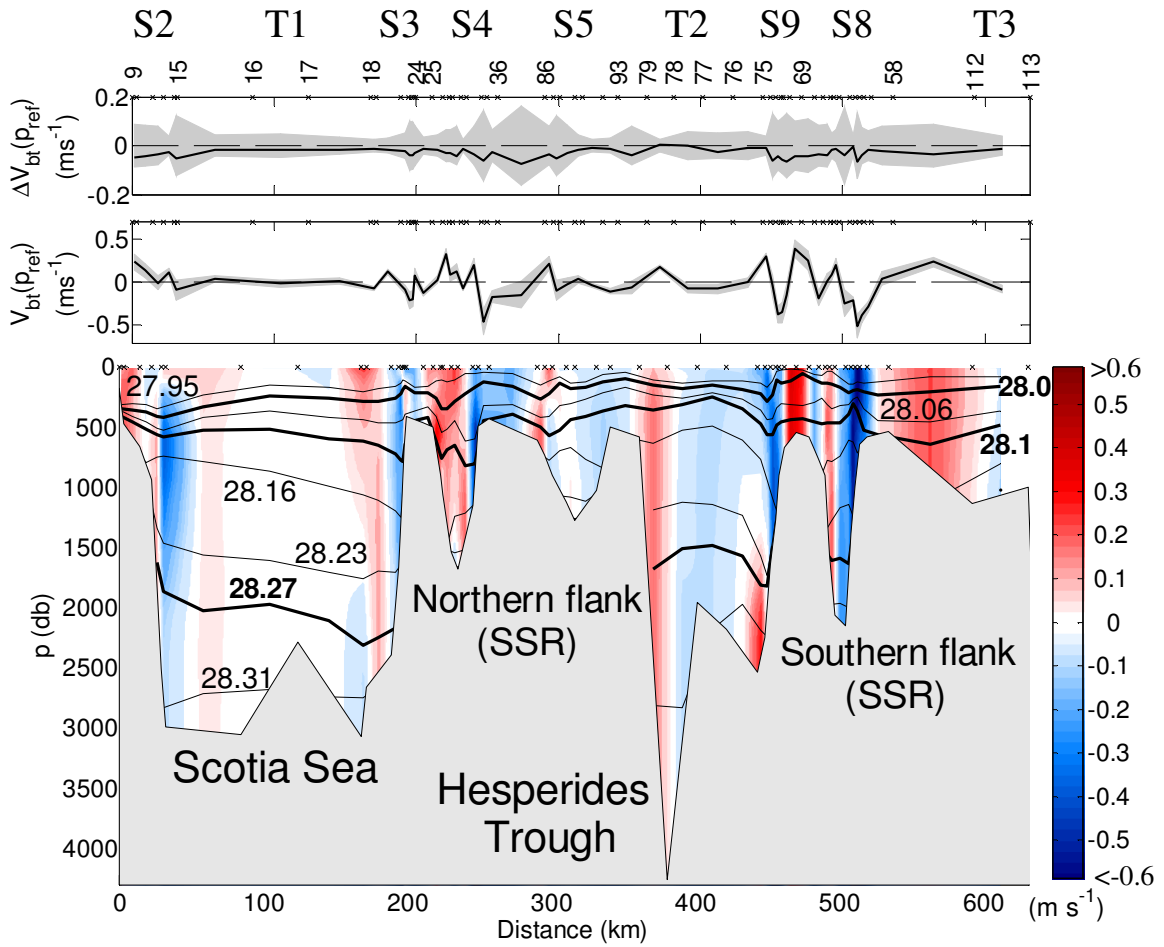
Figure 3.6. *The difference between the model solution with rank=5 and the first guess obtained from the ESASSI-08 data (top panel); the shaded areas denote the uncertainty of the first guess. The barotropic component obtained after the inversion of the model, with shaded areas denoting the uncertainty of the solution (middle panel). The barotropic component has been added to the geostrophic velocities computed from station pairs to yield the total geostrophic velocity field (lower panel); black lines are the neutral density model interfaces (the thicker ones correspond to 28.00, 28.10, and 28.27 kg m^{-3}). Positive values denote outward velocities from the box domain.*

The barotropic velocities have a standard deviation of about ±0.20 m s^{-1} and there is no correlation ($\rho^2 = 0.02$) between the intensity of the geostrophic shears and the barotropic velocities. Nevertheless, barotropic velocities up to ±0.30 m s^{-1} are obtained only where geostrophic shears are smaller than ±0.10 m s^{-1}. Muench and Hellmer (2002) noted that in the northwestern Weddell Sea the weak stratification entails stronger barotropy. Conversely, where geostrophic velocities are larger than ±0.10 m s^{-1}, the barotropic component is smaller. Thompson and Heywood (2008) observed a similar behavior related

to the steepness of the bottom slope for a cross-slope section at the tip of the Antarctic Peninsula. At some of these locations the barotropic velocity has opposite sign to the baroclinic component respect to the deepest common level, yielding bottom undercurrents.

Narrow but strong slope currents are observed flowing to the north/south over the western/eastern flanks of the gaps (that is, leaving shallow areas to the left of the flow). The same holds for the Hesperides Trough, which shows a clear clockwise circulation: outward from the box (to the east) through casts 79-78 and inward (to the west) through casts 77-78 (lower panel of Fig. 3.6, transit T2).

Regarding the hypothesis of synopticity it is worth noting that ESASSI-08 was a comparatively fast cruise compared with the time that it takes to perform large scale cruises used afterwards to run an inverse model. All stations used in the model were sampled in a 10 day period with the exception of stations 112 and 113 (transit T3, see Fig. 3.1), which were sampled five days latter. The non-synopticity respect to the ECOANTAR-94 casts is not relevant in this case because the sensitivity tests indicate that the results along the box are not sensitive to the flow across that transect.

CHAPTER 4

WATER MASS PATHWAYS AND TRANSPORTS
OVER THE WESTERN SECTOR OF THE SOUTH SCOTIA RIDGE

4.1. Introduction

Previous studies on the outflow of Weddell Sea waters into the Scotia Sea have mostly focused on bottom waters and on the deeper, eastern gaps of the SSR. The different cruises and methodologies used to estimate the transports through the Orkney Passage show an overall agreement for the WSDW outflow: results from inverse models are between the 3.48 ± 1.81 Sv (1 Sv ≡ 10^6 m^3 s^{-1}) given by Franco et al. (2007) and the 5.6 ± 0.1 Sv given by Naveira-Garabato et al. (2002b), while ocean circulation models give mean annual transports of 4.2 Sv with a seasonal variability of 0.3 Sv (Schodlok et al., 2002). Naveira-Garabato et al. (2003) also give some figures for the net flow over the whole SSR: 19 ± 7 Sv for the entire water column, of which 6.0 ± 1.5 Sv would correspond to bottom waters and 10.5 ± 5 Sv to LCDW/WDW.

The outflow through the gaps west of the South Orkney Islands is much more uncertain: the annual mean WSDW transport of 2.2 Sv with a seasonal variability of 0.2 Sv obtained by Schodlok et al. (2002) contrasts with the 0.12 ± 0.03 Sv and the -0.1 ± 0.3 Sv given by Franco et al. (2007) and Naveira-Garabato et al. (2002b), respectively. Franco et al. (2007) suggested that the differences among the reported values could be due to the different sampling strategies and methodologies of the analysis. These would be particularly critical when the flow is constrained by a complex topography and subjected to a marked temporal variability derived from the presence of meanders and narrow jets, as it is west of 50ºW. The western gaps of the SSR are shallower than the eastern gaps, and therefore only the lighter components of bottom waters are allowed to overcross west to the South Orkney Islands. However, the fact that the western path is shorter and carries colder and fresher water than the eastern branch suggests that it can also play a significant role in the ventilation of the Scotia Sea.

The objective of this chapter is to use the accurate quantification of the transport of volume, heat, and salt obtained in chapter 3 to infer the regional circulation over the western sector of the SSR. We will focus on the gaps of the northern and southern flanks of the ridge and on the flow that surrounds the Hesperides Trough, a key topographic feature located in between the northern and southern flanks. The analysis of the inverse model results is presented as follows: in section 4.2 we infer the overall regional circulation, in section 4.3 we focus on the outflow of Upper WSDW through the Hesperides Passage and in section 4.4 we examine the water mass modification in the Hesperides Trough. Conclusions are outlined in section 4.5.

4.2. Regional circulation

The volume, heat- and salt-anomaly fluxes obtained after the inversion allow the study of the circulation across the western sector of the SSR. The lateral fluxes along the box domain and the cumulative transports before and after the inversion are shown in Fig. 4.1, where we can observe that transits T1 and T3 introduce most of the initial imbalance. In order to determine the net flow through the sector of the Weddell-Scotia Confluence region covered by the box domain we have compared the net flow crossing its south-southeastern boundary with the net flow through the north-northeastern boundary (Fig. 4.2). In a scenario of perfect volume, heat, and salt conservation, the transports through these two boundaries should be the same. The selected rank of the solution does not reach that point, but the differences fall within the estimated a posteriori uncertainties (lower panels of Fig. 4.2) and are definitely much better than before the inversion (upper panels of Fig. 4.2).

The net fluxes through the region have been quantified as the mean value of the black and gray curves of Fig. 4.2, obtaining northward fluxes of 7 ± 5 Sv, 14 ± 5 TW, and $(0.8 \pm 0.4) \cdot 10^6$ kg s^{-1}. The northward fluxes associated with the export of WDW have been quantified in 7 ± 4 Sv, 11 ± 6 TW and $(0.7 \pm 0.4) \cdot 10^6$ kg s^{-1}, i.e., virtually the same as the full depth integrated transport. These positive heat- and salt-anomaly fluxes, most of them carried within layer 6 (lower panels of Fig. 4.2), do not mean that the Weddell Sea is injecting heat and salt into the Scotia Sea after leaving the Hesperides Trough. They are positive because the WDW entering the SSR from the Powell Basin is warmer and saltier
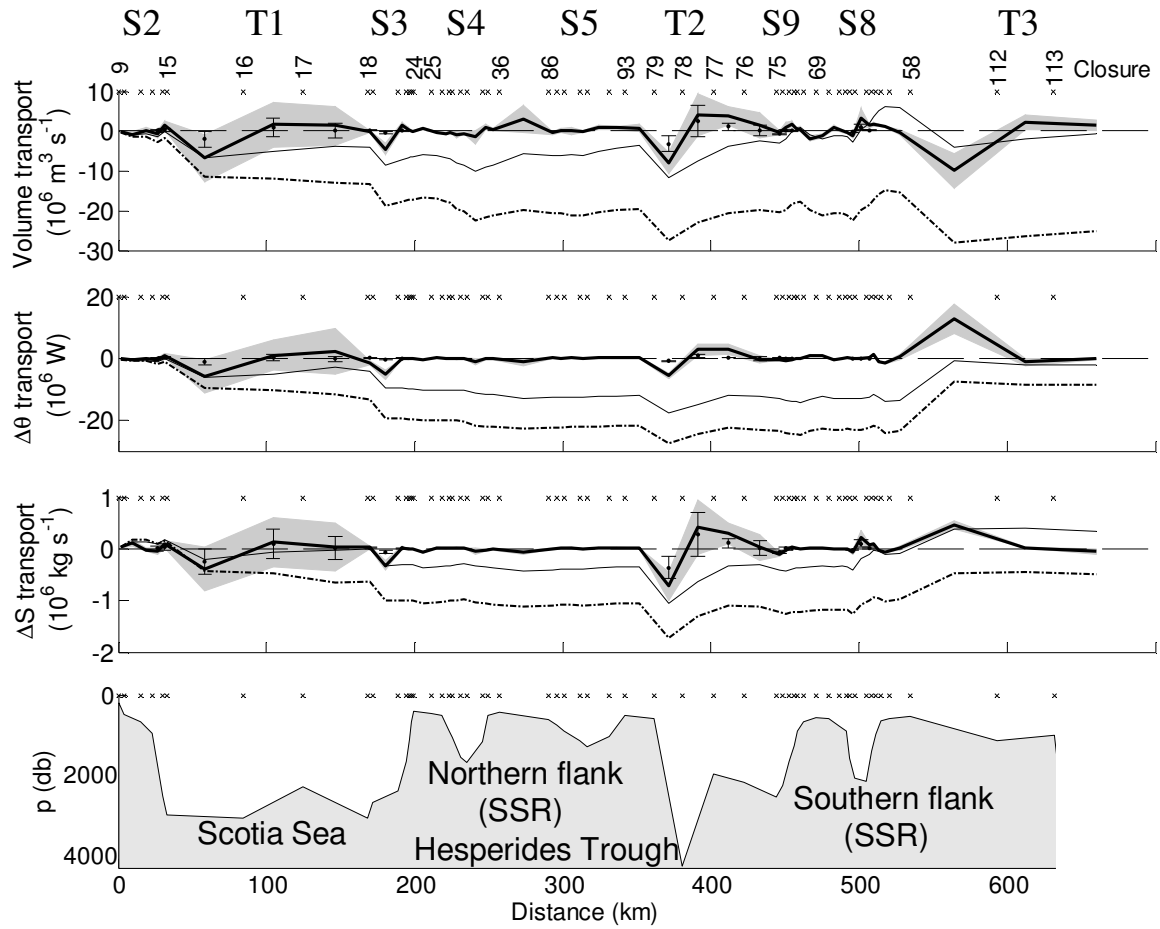
Figure 4.1. *Three upper panels: full depth cross-section flow at the box walls (thick solid line), its uncertainty (shaded area) and cumulative transports before (dash-dot line) and after (thin line) the inversion. Bars denote the transport (central point of the bar) and uncertainty associated with WSDW. The bathymetry is plotted in the lower panel.*

than the mean temperature and salinity of the box domain, then resulting in positive potential temperature and salinity anomalies, respectively. However, the WDW overflowing the SSR is cooler and fresher than the LCDW located further north (out of the box domain), then contributing to the cooling and freshening of the Scotia Sea. At intermediate levels, WDW and a part of LCDW ($28.1 < \gamma^n < 28.27$ kg m^{-3}) occupy most of the lateral area of the box (Fig. 3.2). The volume transport across the different sections of the region is shown in the upper panel of Fig. 4.3.

Above the WDW, the subsurface layers (2, 3, and 4) indicate a net southward transport of AASW. In the southern flank of the ridge, the southward flow is mostly carried by the barotropic jet of transit T3 (casts 58-112), whereas in the northern flank there is an overall

inflow into the ridge from the Scotia Sea. At surface (layer 1), however, the net volume transport is to the north. More important is the heat imbalance of 3.2 ± 1.6 TW, which indicates a heat gain of the surface water as it moves to the north, most likely from air-sea interactions.
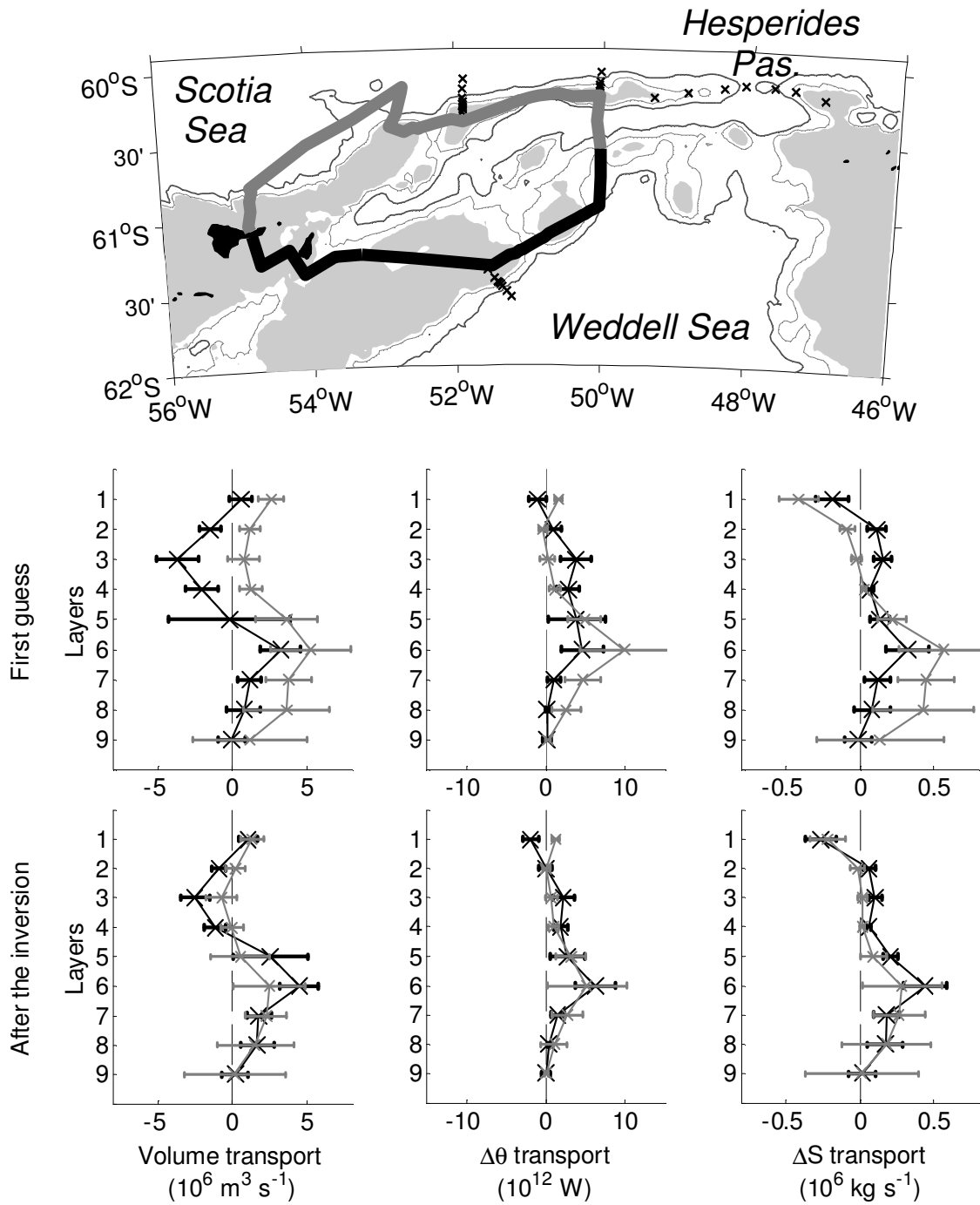
Figure 4.2. *Property transports across the southern (in black, positive entering the domain) and northern (in gray, positive exiting the domain) boundaries of the box before and after the inversion.*
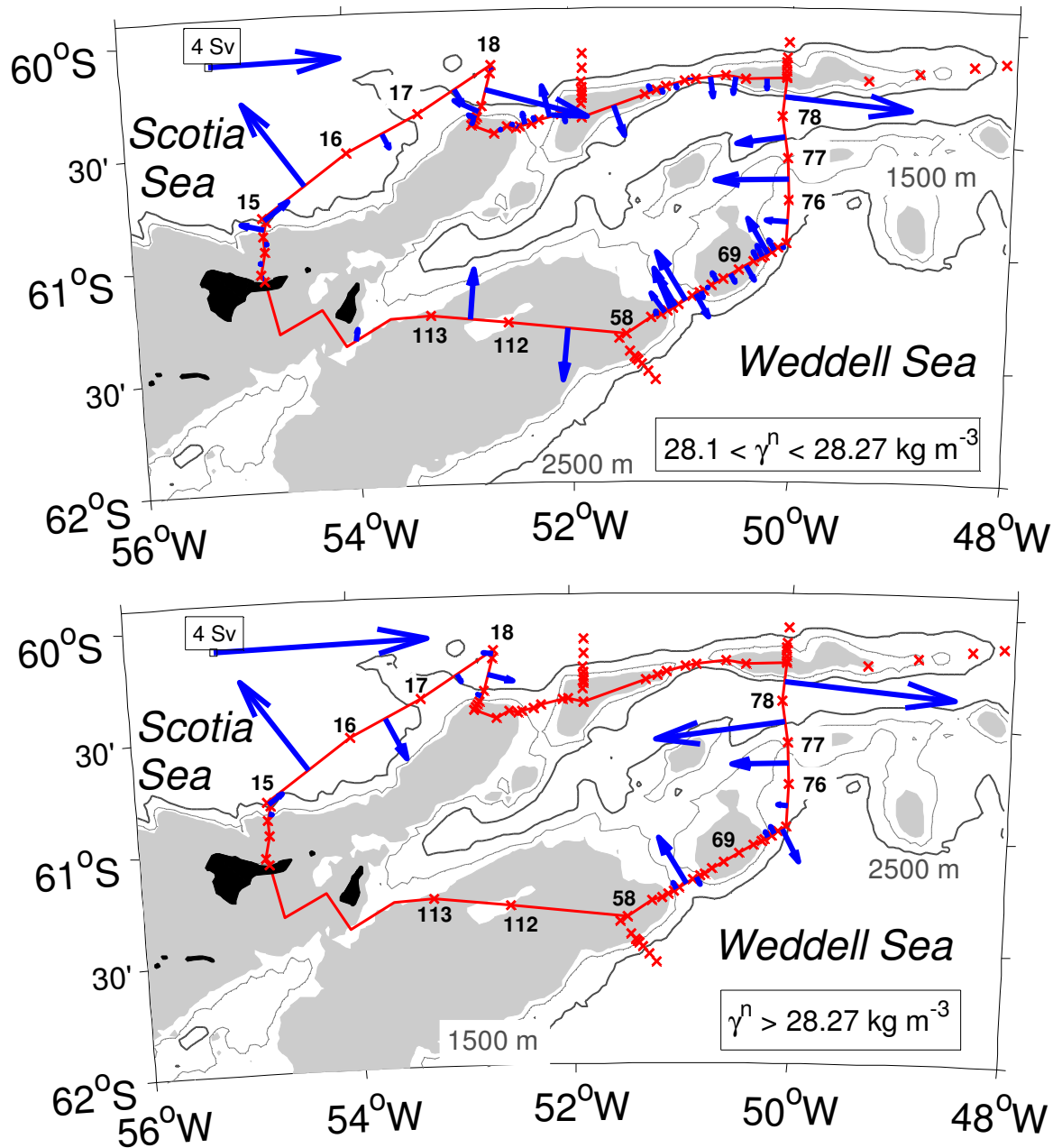
Figure 4.3. *Volume flows across the different passages of the domain for water masses with density greater than 28.10 kg m^{-3}. Upper panel: LCDW/WDW and modifications. Bottom panel: WSDW and modifications.*

Below the WDW, the WSDW enters into the ridge region from the Powell Basin (black line, lower panels of Fig. 4.2). In this case the flow across the north-northeastern boundary (gray line, lower panels of Fig. 4.2) only accounts for the net flow along the Hesperides Trough, as WSDW is too deep to flow through the gaps of the northern boundary of the

domain. The volume transport across the different sections of the region is shown in the lower panel of Fig. 4.3.

The water mass pathways are inferred from the joint analysis of the water mass distribution and the velocity field and fluxes obtained after the inversion. The analysis is complemented by the potential temperature and absolute velocity distributions across the ESASSI-08 section that crosses the Hesperides Passage, out of the box domain (Fig. 4.4) as well as by the previous knowledge of the circulation in the region (Gordon et al., 2001; Naveira-Garabato et al., 2002a; von Gyldenfeldt et al., 2002).
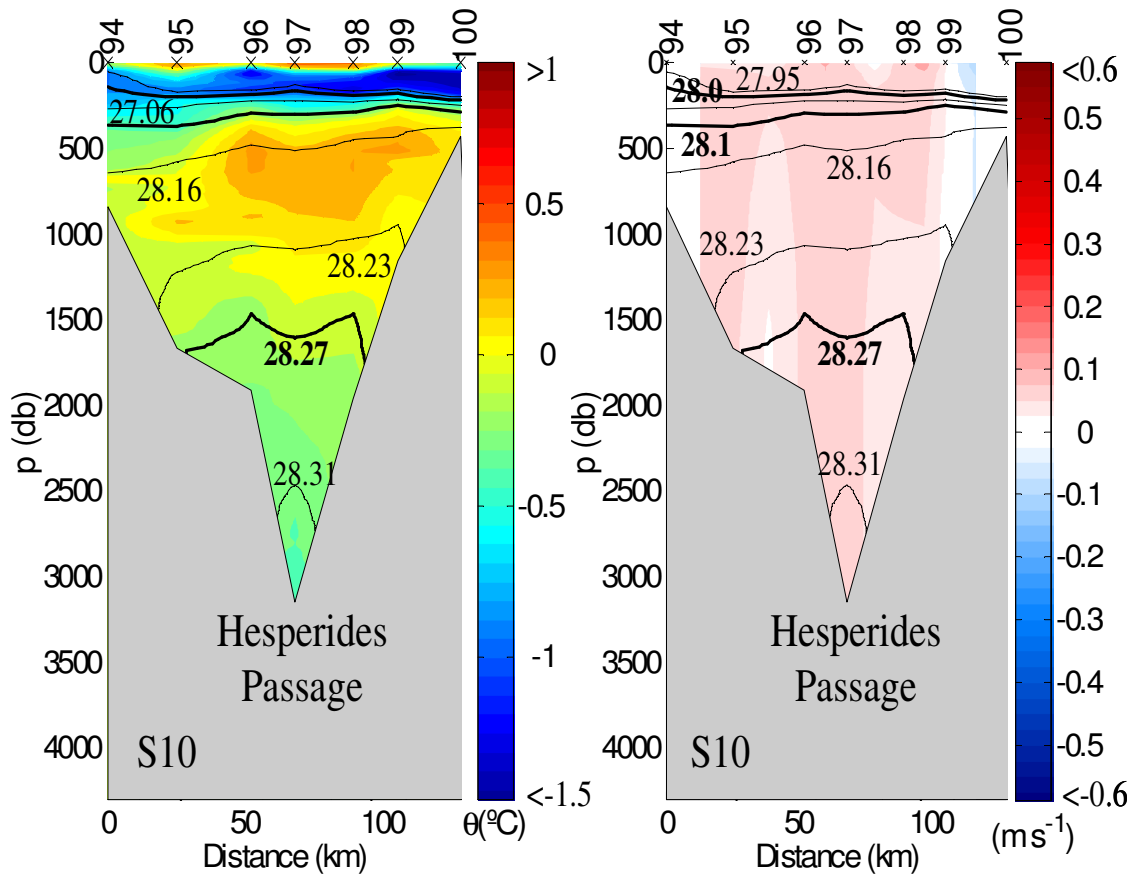
Figure 4.4. ESASSI-08 section across the Hesperides Passage, located out of the box domain (see Fig. 3.1). Left panel: potential temperature distribution; right panel: the velocity field obtained following Rudnick's method (Rudnick, 1996; positive velocities are northward). Solid lines represent the neutral density model interfaces.

In the WDW density range, there are two inflows from the Powell Basin into the Hesperides Trough (upper panel of Fig. 4.3): a net inflow of 3.8 ± 1.5 Sv through section S8 (51ºW, 61.3ºS), and a flow of 5 ± 2 Sv through 50ºW (section 9 and the sector of transit T2 south of 60.6ºS). Of these 5 Sv, 2.3 ± 1.3 Sv were measured flowing westwards between casts 77-76, in good agreement with the flow registered by a mooring deployed in this area (von Gyldenfeldt et al., 2002). An additional inflow (1.9 ± 1.4 Sv) enters into the ridge region through the shallow, southwestern sector of the box domain, likely coming from the Bransfield Strait and the tip of the Antarctic Peninsula. Most of that inflow (1.5 ± 1.0 Sv) crosses the western sector of transit T3 (casts 113-112) and the rest flows between cast 113 and Elephant Island.

The most important outflow of WDW from the box domain is an eastward flow carrying 3.9 ± 0.6 Sv along the northern wall of the Hesperides Trough. From these, 1.5 ± 1.2 Sv recirculate clockwise within the trough (casts 78-77), while the rest spreads northwards into the Scotia Sea through the Hesperides Passage (Fig. 4.4). Secondary outflows over the northern flank of the box domain (sections S4 and S5) are also obtained, namely a deep outflow of 1.4 ± 1.0 Sv through section S4 and a fast (0.21 ± 0.08 m s^{-1}, Fig. 3.6) but narrow jet over the western shelf break of section S5. This narrow jet, negligible in terms of WDW transport (0.18 ± 0.13 Sv), was also recorded by drifters associated with a branch of the Antarctic Slope Current (Heywood et al., 2004, Thompson et al., 2009).

The source of formation for the lighter component of WSDW that reaches the northern side of the Powell Basin is the Larsen Ice Shelf, in the northwestern Weddell Sea, south of 64.5ºS (Fahrbach et al., 1995). This recently formed WSDW has the buoyancy needed to cross the southern gaps of the SSR, west of the South Orkney Plateau (Naveira-Garabato et al., 2002b). All these gaps are connected with the Hesperides Trough, which in turn is connected to the Scotia Sea only through the Hesperides Passage. The colder and fresher WSDW component observed in the box injects 1.8 ± 1.8 Sv from the Powell Basin into the Hesperides Trough (lower panel of Fig. 4.3), 1.0 ± 0.7 Sv through section S8 (51ºW) and 0.8 ± 0.6 Sv through transit T2 (50ºW). Schodlok et al. (2002) estimated the net transport of WSDW over the SSR west of the South Orkney Islands in 2.2 Sv, indicating that most of the inflow entering the ridge would be guided by the bathymetry of the trough.

4.3. Outflow of Upper WSDW through the Hesperides Passage

The exportation of WSDW from the Weddell Sea to the Scotia Sea deserves special attention. The outward flow of WSDW from the box domain (transit T2, Fig. 4.3) and after that from the Hesperides Trough into the Scotia Sea through the Hesperides Passage (Fig. 4.4) is found below 1500m, a shallower level than the upper level of the WSDW component that outflows into the Scotia Sea through the Orkney Passage (Naveira-Garabato et al., 2002b). Since the Hesperides Passage is not part of the inverse model domain, we had to estimate the WSDW outflow by applying the Rudnick methodology to section S10, obtaining a volume transport of 2.3 ± 1.1 Sv.

We will show next that the WSDW outflow through the Hesperides Passage only accounts for Upper WSDW. Lower WSDW is not allowed to spread into the Scotia Sea over the western sector of the SSR region. We will also show that once the more ventilated form of WSDW observed in the region outflows into the Scotia Sea, it overlies saltier WSDW from the eastern passages of the SSR. To do that, we carry out a separate analysis of the ESASSI-08 stations located in the Powell basin and over the deepest areas of the SSR from those stations sampled in the Scotia Sea. Some of the stations under consideration are out of the box domain and are then shown in Fig. 4.5.
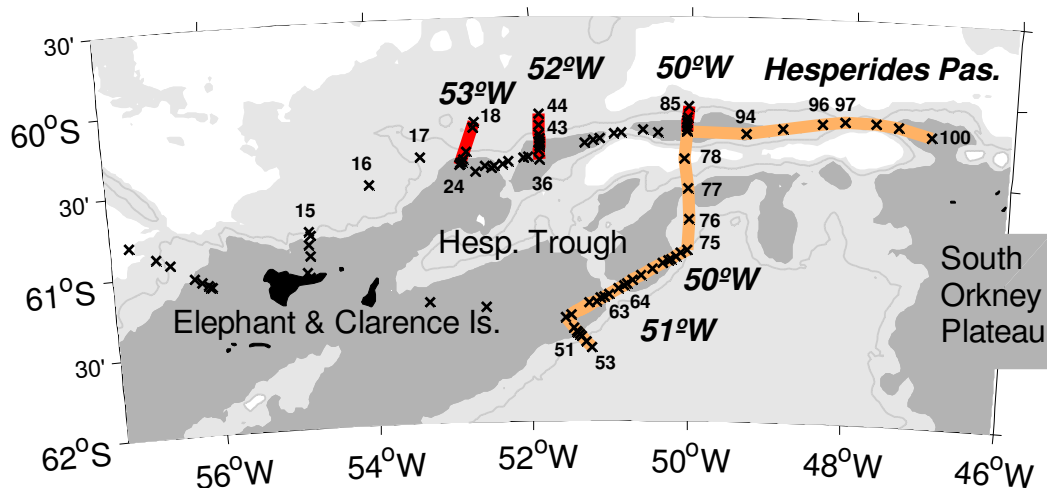
Figure 4.5*. ESASSI-08 hydrographic stations (crosses) used to study the exportation of WSDW across the SSR. Stations over the ridge and in the Scotia Sea are marked with orange/red lines, respectively. The bathymetry (Smith and Sandwell, 1997) delimitates areas shallower than 1500m (dark shading), with depths between 1500-3500m (light shading) and deeper than 3500m (in white). The 2500m isobath is also plotted (grey line).*

The potential temperature vs. salinity diagram (upper panel of Fig. 4.6) shows that the coldest and relatively freshest values of WSDW are observed at the bottom layers of the gap indenting the southern flank of the ridge at about 51ºW (2100-2000m depth, casts 63-64, Fig. 4.5). Eastwards, at 50ºW (2500-2100m depth, casts 75-76, Fig. 4.5), the offshore, deepest profiles show warmer and relatively saltier water at similar densities (see the same upper panel of Fig. 4.6). The transect crossing the Hesperides Trough at about 50ºW (maximum depth of 4200m at cast 78, Fig. 4.5) shows water relatively warmer and saltier than that observed in the southern flank (see the upper panel of Fig. 4.6) and a bottom density slightly higher than 28.31 kg m^{-3} (the neutral density limit between Upper/Lower WSDW). At the Hesperides Passage (3100m depth, station 97, Fig. 4.5) these two types of WSDW are separated by an abrupt change in the salinity trend. The Upper WSDW has similar θS properties to those found in the Hesperides Trough. The Lower WSDW is saltier than that observed at the southern flank of the SSR (see the upper panel of Fig. 4.6).

We also used the quasi-conservative PO4* concentration (see the lower panel of Fig. 4.6) as a water mass tracer (Broecker et al., 1998). Within the Upper WSDW layer (28.27 < γ^n < 28.31 kg m^{-3}), PO_4^* values in the Hesperides Passage range from 1.70-1.72 μmol kg^{-1} (cast 96) to 1.55-1.56 μmol kg^{-1} (cast 97). In the Scotia Sea, PO4* concentrations range from 1.67-1.69 μmol kg^{-1} (casts 43 and 85) to 1.61 μmol kg^{-1} (cast 44). Two groups can be distinguished: casts 75, 77, 78, 97 and 44 range from 1.55 to 1.63 μmol kg^{-1}, whereas casts 64, 96, 85, and 43 range between 1.66 and 1.72 μmol kg^{-1}. Below γ^n = 28.31 kg m^{-3} the near bottom levels of the cross-slope sections in the Powell basin show the highest dispersion of PO4* concentrations: at two stations located nearly over the same isobath (2600-2500m) and at about the same neutral density (28.35 kg m^{-3}) the PO4* concentrations range from 1.77 μmol kg^{-1} (51.5ºW, station 52) to 1.65 μmol kg^{-1} (50ºW, station 75).

These measurements altogether with the circulation inferred from the inverse model suggest that, after crossing the southern flank of the SSR (casts 63 and 76, Fig. 4.5) Upper WSDW from the Powell Basin fills the deeper layers of the Hesperides Trough (cast 78) and thereafter it outflows into the Scotia Sea through the Hesperides Passage. Casts 64, 96, 85, and 43, with PO4* concentrations higher than 1.65 μmol kg^{-1}, trace an outflow path attached to the inner slope of the Hesperides Passage, while casts 75, 77, 78, 97, 44, with PO4* concentrations smaller than 1.65 μmol kg^{-1}, trace an offshore outflow branch.
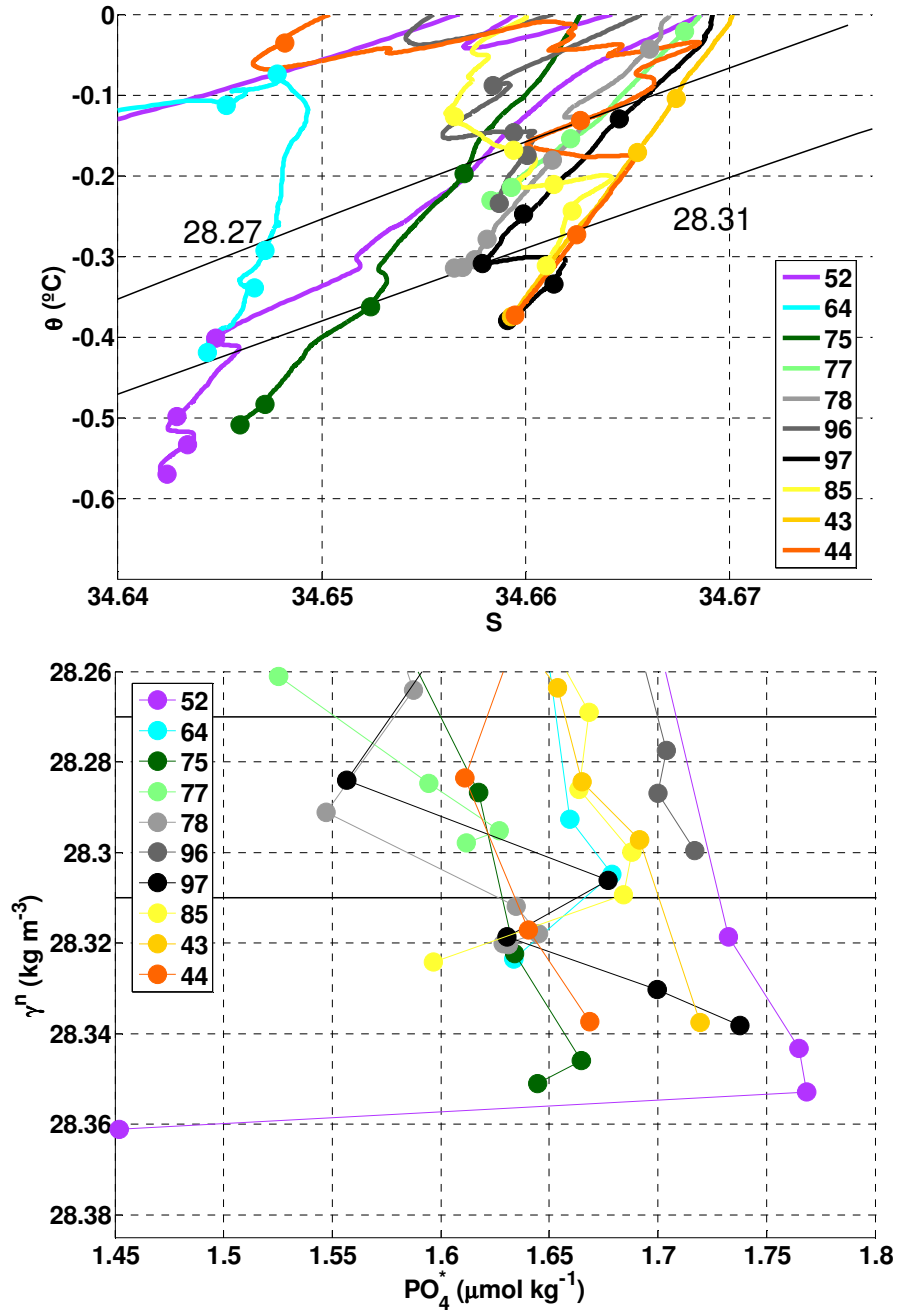
Figure 4.6. *Potential temperature vs. salinity (upper panel), and neutral density vs. PO₄* (lower panel) diagrams for some of the deepest casts of the ESASSI-08 cruise.*

Moreover, the fact that the PO_4^* keep constant between the southern flank of the SSR (casts 64, 75) and different locations of the Hesperides Trough (casts 78, 97) confirms that the water filling the trough ($\gamma^n \sim 28.32$ kg m^{-3}) has also a southern origin. Its values are slightly higher than those reported by Naveira-Garabato et al. (2002a) at the western slopes of the eastern gaps of the SSR at the same density level (i.e. 1.55-1.60 µmol kg^{-1}).

In the Scotia Sea, the bottom level of station 85 ($\gamma^n \sim 28.32$ kg m^{-3}, 2900m) shows a PO4* concentration of 1.60 μmol kg^{-1}, that is, smaller than the concentration observed at the Hesperides Passage and Trough but within the range given by Naveira-Garabato et al. (2002b) at this density level. This provides further evidence that the bottom layer waters of the northern wall of the ridge correspond to Lower WSDW from the eastern gaps of the SSR.

The deep ($\gamma^n > 28.32$ kg m^{-3}) PO$_4$* values of station 97, in the Hesperides Passage, are higher than those observed in the Scotia Sea; they are actually within the range of the densest water sampled at the southern flank of the ridge over the 2500m isobath. This poses the question of whether the bottom layers of station 97 could come straight from the Philip Passage, a shallower passage (2300-2700m deep) located right to the south (60.7-60.8°S) of the Hesperides Passage. However the abrupt change observed in the θS diagram of Fig. 4.6 suggests that this is rather unlikely; instead, the similarity between the θS properties of that lower layer and those of the profiles obtained in the Scotia Sea suggest that this layer has not crossed the Hesperides Passage, but correspond to waters of the northern flank of the ridge. Further evidence comes from historical profiles (Southern Ocean Atlas, R/V Polarstern, April 1998) located over a meridional section (48°W) running from the Powell Basin to the Scotia Sea through the Philip and Hesperides Passages: the differences between the Philip Passage profiles and the profiles of the Hesperides Passage are similar to those observed between the Hesperides Trough and the Hesperides Passage. Right in between the Philip and Hesperides Passages, the deepest (5100m) profile (in green, see Fig. 4.7) shows similar values to those observed further west in the Hesperides Trough (e.g. at 50°W, at 4200m, station 78, see Fig. 4.6): their maximum densities are of about 28.32 kg m^{-3} and they have the same PO$_4$* concentrations at that isopycnal. Moreover, neither the historical PO$_4$* values observed in the Philip Passage (in blue, lower panel of Fig. 4.7) nor those observed at the Hesperides Passage (in red, lower panel of Fig. 4.7) are as high as those measured at the bottom levels of station 97.

Summarizing, the Lower WSDW ($\gamma^n > 28.31$ kg m^{-3}) observed occupying the bottom layers of the Hesperides Trough and the Hesperides Passage is not the same water. We can ensure that the water observed at the bottom of the Hesperides Passage comes from the

61

northern flank of the ridge and that Lower WSDW is not allowed to cross neither the Philip Passage nor the Hesperides Passage. Upper WSDW is therefore the only AABW component able to overflow into the Scotia Sea through the gaps located to the west of the South Orkney Plateau. Conversely, the reason of the high PO$_4$* concentrations observed at station 97 remains known.
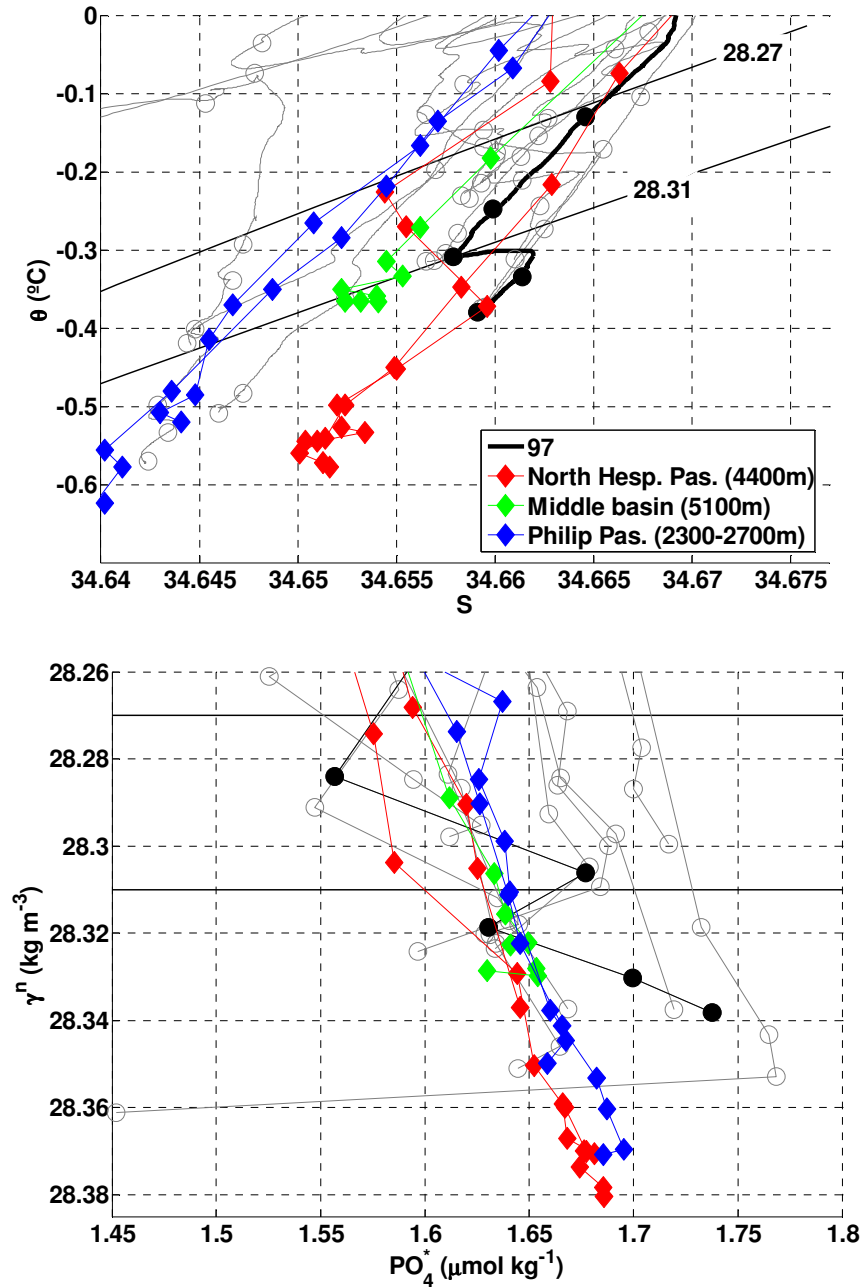
Figure 4.7. *Potential temperature vs. salinity (upper panel), and neutral density vs. PO$_4$* (lower panel) diagrams for the deep casts of the ESASSI-08 cruise shown in Fig. 4.6 (in grey, with cast 97 highlighted in black) and for some historical profiles located at 48ºW (coloured) extracted from the Southern Ocean Atlas data set (Orsi and Whitworth, 2005).*

4.4. Water mass modification

The circulation inside the Hesperides Trough plays a key role in the exchange of hydrographic properties between the involved water masses. It has been shown that modified waters flowing northwards along the eastern continental slope of the Antarctic Peninsula inflow into the trough following the topography. Seaward, less modified water masses are injected into the trough from deeper areas of the Powell Basin. Both branches get close when crossing the southern gaps of the ridge and are forced to surround altogether the walls of the trough. This results in different mixtures exiting the box domain.

The inward and outward volume transports through the walls of the box domain plotted over a θ-S diagram are shown in Fig. 4.8. The first conclusion is that waters outflowing the domain are more homogenous (Fig. 4.8b) than on entrance (Fig. 4.8a), particularly for the temperature. The exception is around the 28.1 kg m^{-3} isopycnal, where the outflowing waters are colder and fresher (barotropic jet at the southeastward transit T3) or warmer and saltier (at the northern shelves) than on entrance. The diapycnal mixing component obtained after the inversion has a small impact on the property transports over the box area when compared with the lateral flows, then suggesting that the modification of the water masses takes place mostly along isopycnals.

The water masses delimited by the 28.16 and 28.23 kg m^{-3} isopycnals inflow into the ridge with temperatures ranging from about -0.3ºC to 0.5ºC (Fig. 4.8c), and outflow within a narrower range: from about -0.2ºC to 0.25ºC (Fig. 4.8d). The core of WDW lies within these isopycnals over the western sector of the SSR. Its potential temperature value is slightly below 0.5ºC when this water mass inflows into the ridge through the southern flank (Fig. 4.8c, casts 62 and 76). The maximum is eroded inside the trough while mixing along isopycnals, cooling down to 0.25ºC (Fig. 4.8d, cast 78). The similarity of casts 78 (in the middle of the trough) and cast 77 supports the idea of some recirculation inside the trough (Fig. 4.8c,d).

Figure 4.8 (next page). *Volume transport over a θ-S diagram (transport associated with each θ-S cell): a) flow entering the box; b) flow exiting the box domain; c) to j) zooms of panels a) and b), with different profiles of ESASSI-08 stations overplotted.*
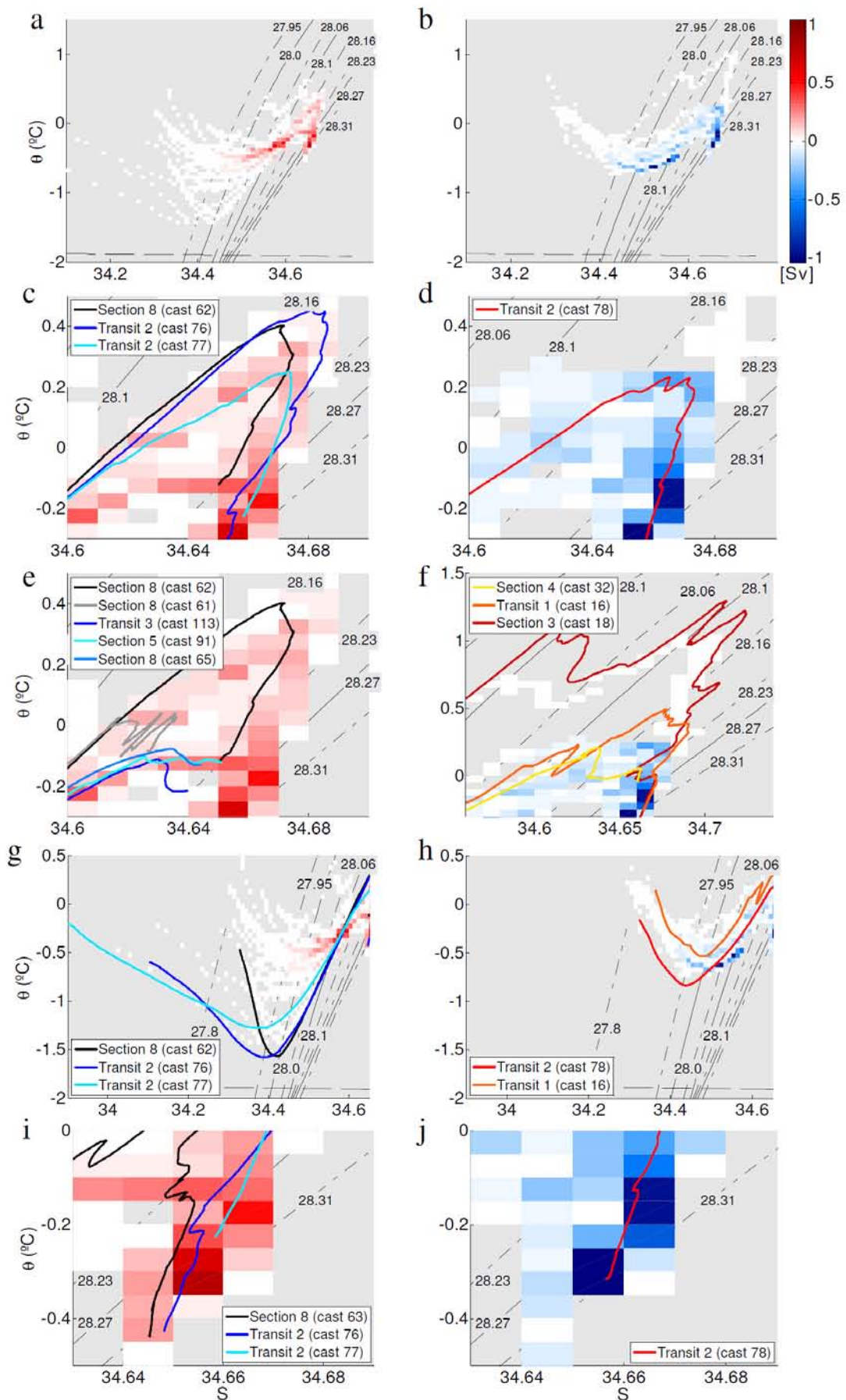
Intense mixing processes associated with the presence of the Antarctic Slope Front (which flows over the western slope of section S8) would be responsible for the modification of the water masses before entering the SSR through that gap (Heywood et al., 2004). The WDW located offshore (0.4ºC, 34.67, Fig. 4.8c, section S8, cast 62, 1400m) is cooled and freshened, resulting in a modified water mass with potential temperature below 0ºC and salinity around 34.63 (Fig. 4.8e, section S8, cast 61, 980m) that bifurcates into two branches. The same water mass is observed 120 km downstream following the 1000m isobath inside the trough (Fig. 4.8e, transit T3, cast 113) and also filling the shallower areas of the western sector of the SSR (Fig. 4.8e, section S5, cast 91, 1300m) as in Heywood et al. (2004). A secondary branch, maybe a bifurcation of this current, is also observed less than 20 km downstream following the 1500m isobath over the eastern slope of section S8 (Fig. 4.8e, cast 65), outflowing to the southeast following the topography.

Once in the Scotia Sea, the colder and fresher WDW from the Hesperides Trough meets the warmer and saltier WDW component from the eastern gaps of the SSR (Naveira-Garabato et al., 2003). The interaction between them and/or with CDW from the ACC further north results in different degrees of modification of the water masses. The deepest profile of section S4 (Fig. 4.8f, cast 32, 1600m) presents two different cores of WDW: the lighter suggests mixing with WDW from the Orkney Passage, and the denser is a deeper branch of WDW from the Hesperides Trough. The proportion of the WDW component from the Orkney Passage is higher seaward (Fig. 4.8f, transit T1, cast 16, 3000m). To the north of the box domain, the LCDW is modified by intrusions of WDW (Fig. 4.8f, cast 18, $\theta_{max} > 1$ºC and $S_{max} > 34.7$, 3000m).

Whereas in the western sector of the Weddell-Scotia Confluence the WDW cools and freshens before overflowing the northern flank of the ridge, the surface and subsurface waters become warmer and saltier (Patterson and Sievers, 1980). The comparison of the sea surface inflow with the more homogeneous surface outflow indicates mixing of water masses, but the heat gain from the atmosphere results in an outflow warmer than expected if only mixing processes were involved (Fig. 4.8h). On the other hand, the freshening of the first 50m at stations 76 and 77 (Fig. 4.8g, transit T2, $\gamma^n < 27.8$ kg m^{-3}, $S < 34.2$) suggests the intrusion of melted water due to their proximity to the South Orkney Plateau, but this signature must quickly dilute as it is not observed anywhere else in the box.

The subsurface WW has a relative temperature minimum of -1.6ºC when inflowing into the ridge through section S8 (Fig. 4.8g, cast 62, S ≈ 34.42, depth ≈ 200m) and transit T2 (Fig. 4.8g, cast 76, S ≈ 34.39, depth ≈ 100m). The value of that minimum warms to the north, where the summer mixed layer is slightly thicker and warmer than to the south (the sea-ice extended north of 62ºS during the cruise, as inferred from the NCEP Reanalysis, NOAA/OAR/ESRL PSD, http://www.esrl.noaa.gov/psd). After surrounding the western side of the Hesperides Trough, this core warms (θ = -0.8ºC) and becomes saltier (S = 34.45) (Fig. 4.8h, transit T2, cast 78). Once outside the trough, in the Scotia Sea, it reaches values of -0.5ºC and 34.47 (Fig. 4.8h, transit T1, cast 16). Overall in the box domain, the relative cores of WW are more pronounced down slope and in seaward locations, whereas over the shelf break an homogenization in temperature (θ ≈ -0.5ºC) is observed and the salinities linearly increase with density at a rate of about 1 (kg m^{-3})$^{-1}$, ranging approximately from 34.4 to 34.6.

Below the WDW, the coldest and freshest component of WSDW observed in the box domain comes from the Powell Basin (Fig 4.11i, section S8, cast 63, and transit T2, cast 76). The outflow from the Hesperides Trough is a water mass slightly warmer and saltier (Fig. 4.8j, transit T2, cast 78). Discarding isopycnal mixing processes on the basis that the inflowing bottom waters are colder and fresher than the northern profiles of the Hesperides Trough, diapycnal mixing is expected to be the responsible for the temperature and salinity changes suffered by the bottom waters while circulating in the trough. Some heat diffusion into the upper layer of WSDW from the lower layer of WDW is obtained after the inversion (Table 4, 0.02 ± 0.05 TW), and some salinity exchange at the deeper layers of the model (Table 4, (0.007 ± 0.007)·10^6 kg s^{-1}).

4.5. Conclusions

The high spatial resolution of the ESASSI-08 data set has allowed the determination of the water mass pathways and property transports in the sector of the South Scotia Ridge west of 50ºW. In order to obtain a better estimation, an inverse model has been applied to correct the barotropic velocities initially inferred from CTD and ADCP data.

Results show that intermediate and bottom Weddell Sea waters overflowing the SSR west of the South Orkney Islands are forced to circulate clockwise around the Hesperides Trough, a process during which water masses undergo some property modifications. Subsurface WW and intermediate WDW (the latter accounts for most of the volume transport) exchange heat and salt mainly along isopycnals. As a consequence of the mixing, both the warmer and saltier WDW and the colder and fresher WW cores are eroded before outflowing into the Scotia Sea and the overall process results in a homogenization of the water masses crossing the ridge. The characteristics of the WDW when outflowing the SSR west of the South Orkney Islands suggest that they could contribute not only to the cooling and freshening of the ACC waters (Whitworth et al., 1994), but also to the modification of the Weddell Sea waters flowing across the Orkney Passage and turning west along the northern flank of the SSR, where they meet (Naveira-Garabato et al., 2002a).

The bottom waters of the Weddell Sea (WSDW) and those in the Scotia Sea are not directly connected through the inverse model domain. It has been shown that when they enter the southern flank of the ridge and recirculate within the Hesperides Trough they incorporate some heat and salt from the lower layers of WDW, but on outflow they are still colder and fresher than the deep water of the Scotia Sea and hence they also contribute to the freshening and cooling of that basin.

When going to the details of the flow, the southern flank of the ridge presents two main entrance gates for WDW and WSDW: the 2100m depth gap at 51ºW, 61.2ºS, where the Antarctic Slope Front is identified, and along the 50ºW meridional section south of the Hesperides Trough. Most of these waters outflow to the Scotia Sea through the deepest gap (3000m, out of the model domain but also sampled during the ESASSI-08 cruise) after circulating around the Hesperides Trough. In the northern flank of the ridge there are two additional shallower gaps playing different roles due to their topographical differences, but the volume transport of WDW is rather small through both gaps. The schemes of the inferred water mass circulation are shown in Fig. 4.9. The pathways of AASW are analogous to the water mass below and therefore not shown in a separate panel. WW is observed overriding the WDW, both following the same pathways.

67
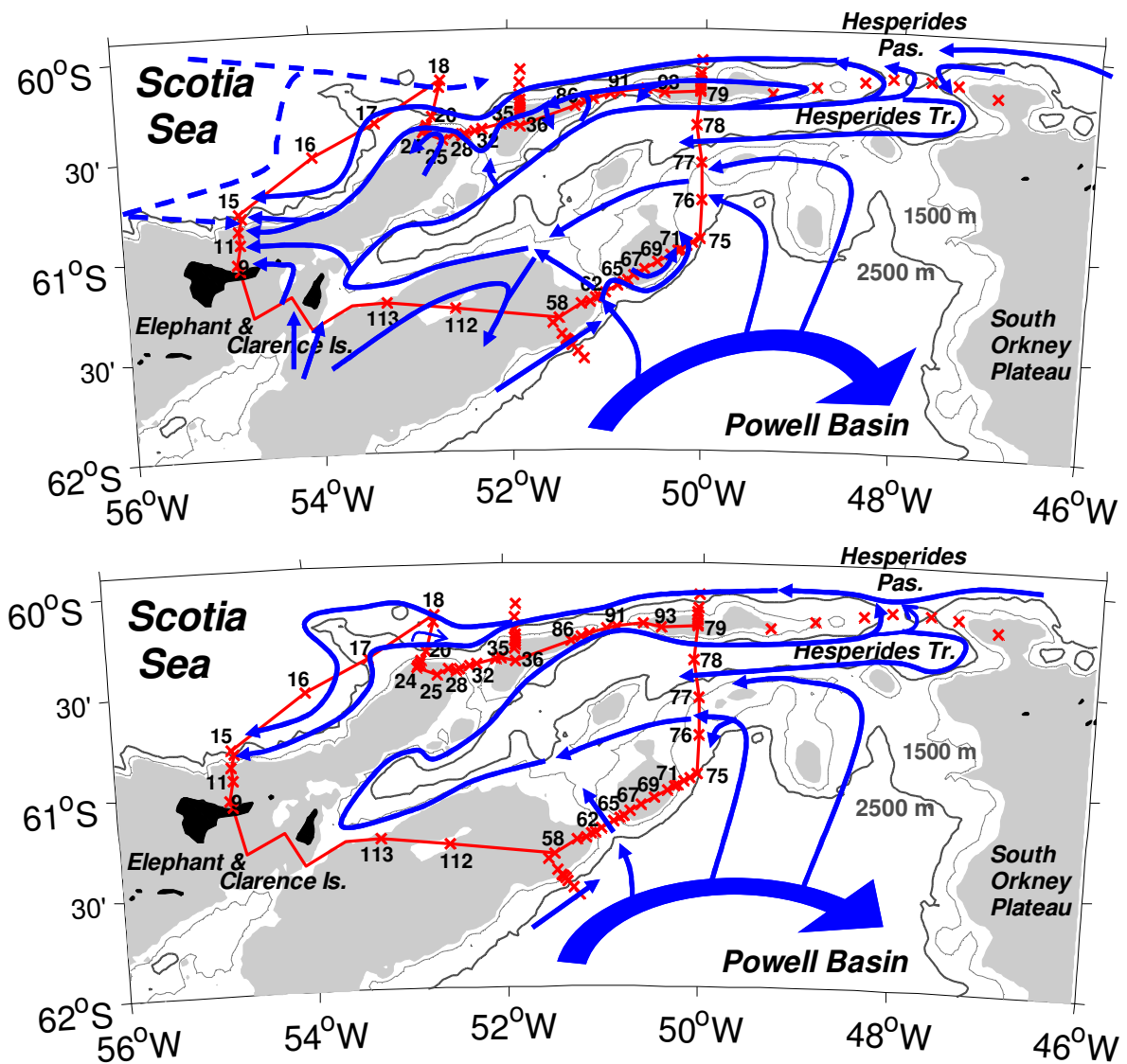
Figure 4.9. *Sketch of the water mass pathways inferred in this study. Upper panel: LCDW (blue dashed lines) and WDW (blue solid lines). Bottom panel: Upper WSDW (blue solid lines).*

A net volume transport of 7 ± 4 Sv of WDW has been obtained flowing from the Weddell Sea into the Scotia Sea across the box domain. When compared with the 10.5 ± 5 Sv estimated by Naveira-Garabato et al. (2003) for the whole South Scotia Ridge, it turns out that the western sector of the SSR plays a very significant role in the export of WDW to the Scotia Sea. The estimated heat- ('enthalpy') and salt-anomaly transports over the box are 11 ± 6 TW and $(0.7 \pm 0.4) \cdot 10^6$ kg s^{-1}, with respect to the local mean values. The box domain is located beyond the Southern Boundary of the ACC, and therefore the obtained heat and salt transports must be understood in the context of the studied region. The mean

values for the box domain are of -0.29 ± 0.16 ºC and 34.56 ± 0.05 (Table 3), much colder but not significantly fresher than the 1.2 ± 1.4 ºC and 34.58 ± 0.14 given by Naveira-Garabato et al. (2003) for the Scotia Sea. Hence, the waters overflowing this sector of the SSR are expected to contribute very significantly to the modification of the lower CDW layers through intense lateral mixing, a process observed by Orsi et al. (1999).

The comparison between the 1.8 ± 1.8 Sv of WSDW entering the southern/southeastern boundaries of the model domain and the 2.2 Sv given by Schodlok et al. (2002) for a section running from the South Shetland to the South Orkney Islands, suggests that a large part of the bottom waters west of the South Orkney Plateau circulates clockwise around the Hesperides Trough, instead of reaching the ultimate gateway (the Hesperides Passage) through the Philip Passage. Note that the 2.2 Sv might be overestimated according to the definition of WSDW used by Schodlok et al. (2002), who based on potential temperature and salinity ranges instead of on neutral density. The obtained values also indicate that the amount of WSDW crossing the western sector of the SSR would be about a half of that flowing through the Orkney Passage (3.48 Sv according to Franco et al. (2007) and 5.6 Sv according to Naveira-Garabato et al., 2002b). When making both statements, however, one must take into account the uncertainties associated with the estimated values.

The modification of the water masses inside the Hesperides Trough inferred from the θ-S analysis is supported by the observations along the 48ºW section obtained by the US DOVETAIL cruise (1997). The clear discontinuity in the vertical distribution of the water mass properties when this section crosses the Hesperides Trough from the Philip Passage to the Hesperides Passage discards a straight, northward flow across the trough. The vertical distribution of LADCP zonal velocities is of special interest: it shows a clear eastward flow along the northern slope of the trough, with velocities higher than 0.10 m s^{-1} for most of the water column and a more localized westward current along the southern slope of the trough, then supporting our results.

CHAPTER 5

THE ANTARCTIC SLOPE CURRENT ACROSS THE SOUTH SCOTIA RIDGE

5.1. Introduction

From Gill (1973) to Baines (2009), all the studies describing the structure of the Antarctic Slope Front have revealed the complexity of the involved processes and of their role in the Southern Ocean circulation. Thus Gill (1973) related bottom water formation with the V-shaped form of the front when the inshore water mass is dense enough to override the shelf break and flow downslope. Orsi et al. (1999) used the oceanic chlorofluorocarbon budget to quantify that about 60% of the circumpolar production of Antarctic Bottom Water (AABW) occur in the Atlantic sector, where the ASF is well apparent. Whitworth et al. (1998) observed that the mixing processes in the frontal region reported by Jacobs (1986) result in different modifications of the regional CDW.

After the lower component of CDW from the ACC incorporates into the Weddell Gyre to the south of the Southern Boundary of the ACC (Orsi et al., 1995), indirect effects from Ekman processes seem to be responsible for the approaching of WDW to the continental slope (Deacon, 1937). The westward current resulting from the geostrophic adjustment and flowing along most of the Antarctic continental margin was first named as the Antarctic coastal current by Deacon (1937). While the transport associated with the ACC has been estimated in many works (e.g., between 117±15 and 144±6 Sv in Whitworth et al., 1982; 143±13 Sv in Naveira-Garabato et al., 2003), the westward transport associated with slope currents remains undetermined at many locations around Antarctica (Mathiot et al., 2011).

In the same way that the ACC is formed by a set of fronts (see Orsi et al., 1995, for a description of their location and properties), the westward flow around Antarctica is not formed by a unique jet. At the tip of the Antarctic Peninsula Thompson and Heywood (2008) distinguished the Antarctic Coastal Current (ACoC), the current associated with the ASF (hereafter the Antarctic Slope Current, ASC) and the Weddell Front (WF), all them in a 400km cross-slope section extending from the continental shelf to the location of the

4000m isobath. They estimated a total net transport of 46 ± 8 Sv, part of it recirculating within the Weddell Gyre, which carries about 60 Sv (Schröder and Fahrbach, 1999). At some locations, like in the southeastern Weddell Sea, the ACoC and the ASC flow too close to each other as to be distinguishable (Heywood et al., 1998), which explains why they were generically referred to as westward coastal currents in early studies.

In this chapter we focus on the path followed by the ASC when it flows from the Weddell Sea into the Scotia Sea through the South Scotia Ridge. This issue has already been addressed by Heywood et al. (2004), who showed the ASC following the bathymetric contours south of the SSR and crossing the southern flank of the ridge at 50ºW over the 1500m isobath. At that point, the transport associated with the ASC was estimated in about 7 Sv. Within the SSR the ASC has been reported to circulate cyclonically around the Hesperides Trough. The last observations of Heywood et al. (2004) were gathered at the northern wall of the trough; further downstream, the observations existing prior to the ESASSI cruise were no conclusive about the outflow of the ASC into the Scotia Sea. Even along the path of the ASF solved by Heywood et al. (2004), the sharpness of the front and the steep bathymetry of the region compared with the spatial resolution of previous cruises showed the convenience of retaking the problem once data with a higher spatial resolution were available. This was precisely one of the major objectives of the E-SASSI project.

A key feature of the ESASSI-08 hydrographic sections is that CTD stations were closely spaced, particularly over the upper slope (1-2 nm) so as to resolve the structure of the Antarctic Slope Front. Because of the trade-off between spatial resolution and temporal synopticity, this poses the problem of whether the stations sampled along a section can be considered to give a synoptic view of the different hydrographic fields and hence used to compute geostrophic velocities between adjacent stations. This problem was already outlined in section 2.6, when examining the geostrophic field. To give an idea of the timing, the completion of the longest ESASSI section, (S9, see Fig. 5.1) took 33 hours; the second longest (S8) took 27 hours; all the others took about 24 hours or less. These values are in principle suitable to consider the stations as 'simultaneous' from a subinertial point of view. However, a few ESASSI stations located very close to their neighbours (e.g. casts 13, 26, 31, 34, 49, 88) were discarded on the basis of the comparison between the vertical structure of the detided currents and the geostrophic currents between stations.
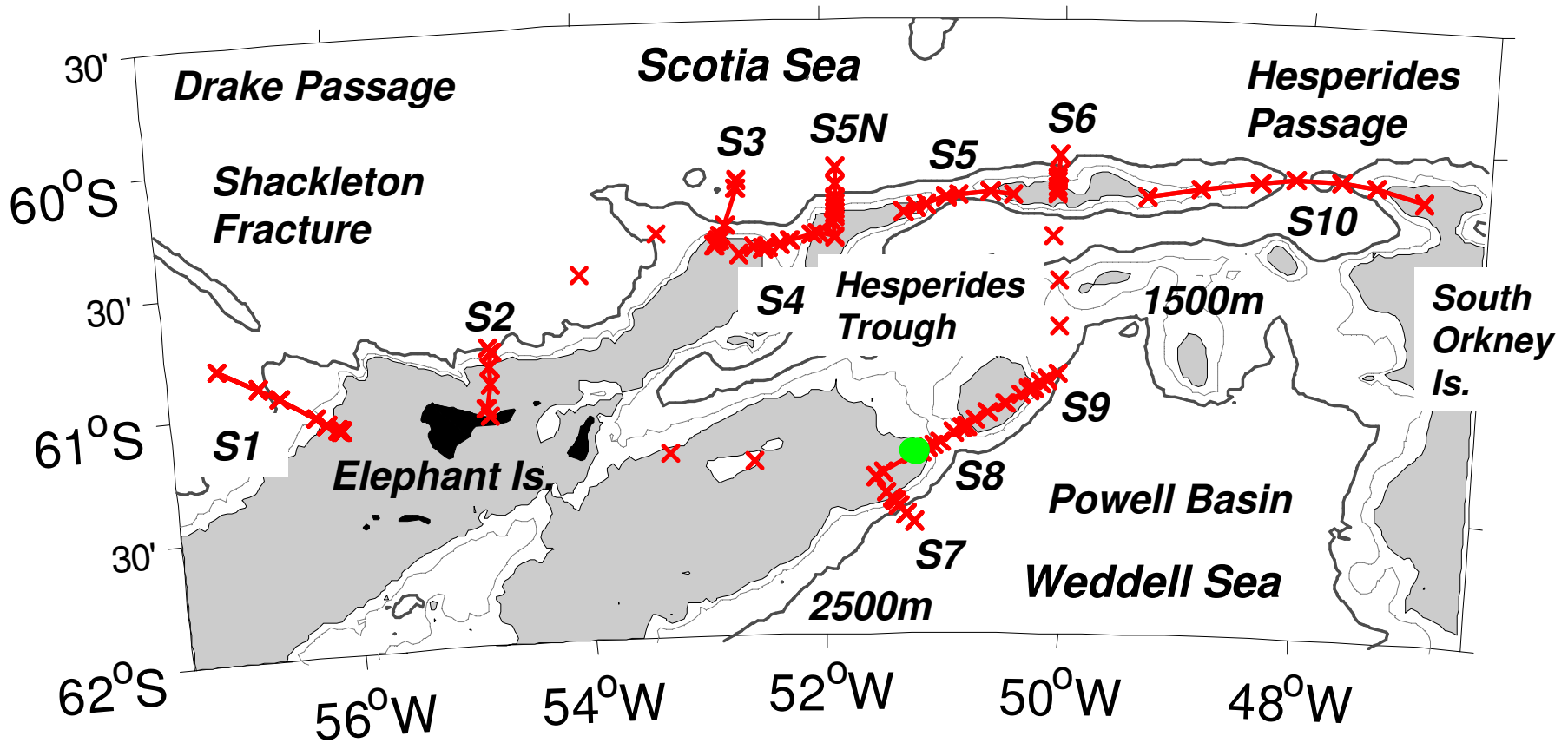
Figure 5.1. *The ESASSI-08 hydrographic sampling (transects and transit casts in red; yo-yo station in green). The bathymetry is from Smith and Sandwell (1997); the areas shallower than 1000m are shaded.*

The goal of this chapter is to make use of the unprecedented spatial resolution of the ESASSI-08 cruise to characterize the ASF/ASC system at three stages of its pathway across the SSR: when it approaches and crosses the southern flank of the SSR; when it crosses the gaps of the northern flank of the ridge; and when it dilutes into the Scotia Sea. The velocity field used to compute transports comes from the results of the inverse model at those sections that are part of the box model (see chapter 3) and from the application of Rudnick's methodology (Rudnick, 1996; Rubio et al., 2009) at the sections located outside the box.

5.2. The Antarctic Slope Current at the southern flank of the South Scotia Ridge

The ASF has been traced in the region from the southeastern Weddell Sea to the southern flank of the SSR, as summarized in the introduction. Here we will first examine three cross-slope ESASSI sections sampled at the southern flank (Sections S7, S8, and S9, see Fig. 5.1). Section S7 (51.4ºW, 61.5ºS) is analogous to the E-DOVETAIL subsection E analyzed by Heywood et al. (2004), except that during ESASSI it was sampled with very high spatial resolution to re-assure the presence of the ASF before it reaches the southern gaps of the SSR. Perpendicular to section S7, section S8 crosses a first gap of the ridge (51ºW, 2100m depth). Section S9 is a cross-slope section at 50ºW, and is collocated with the ALBATROSS subsection G analyzed by Heywood et al. (2004). According to these authors, the ASC goes round the 51ºW gap but it enters into the ridge region at 50ºW. That would be the place where the ASC and the current associated with the WF follow different paths due to bathymetrical constraints: while the ASC turns north and enters the ridge region flowing along the 1000-1600m isobaths, the deeper current associated with the WF continues northeastwards flowing along the 2500-3000m isobaths.

Figure 5.2 (next page). Upper panel: potential temperature distribution across (ESASSI section S7) and along (sections S8 and S9) the southern flank of the SSR; see Fig. 5.1 for location). Lower panel: velocity field across the same sections, with positive velocities directed into the paper (westward in section S7, northward in sections S8 and S9). The ASC is apparent at stations 47 (section S7), 59 and 65 (section S8), and 73 (section S9). The solid lines overplotted on both panels are neutral density isopycnals.
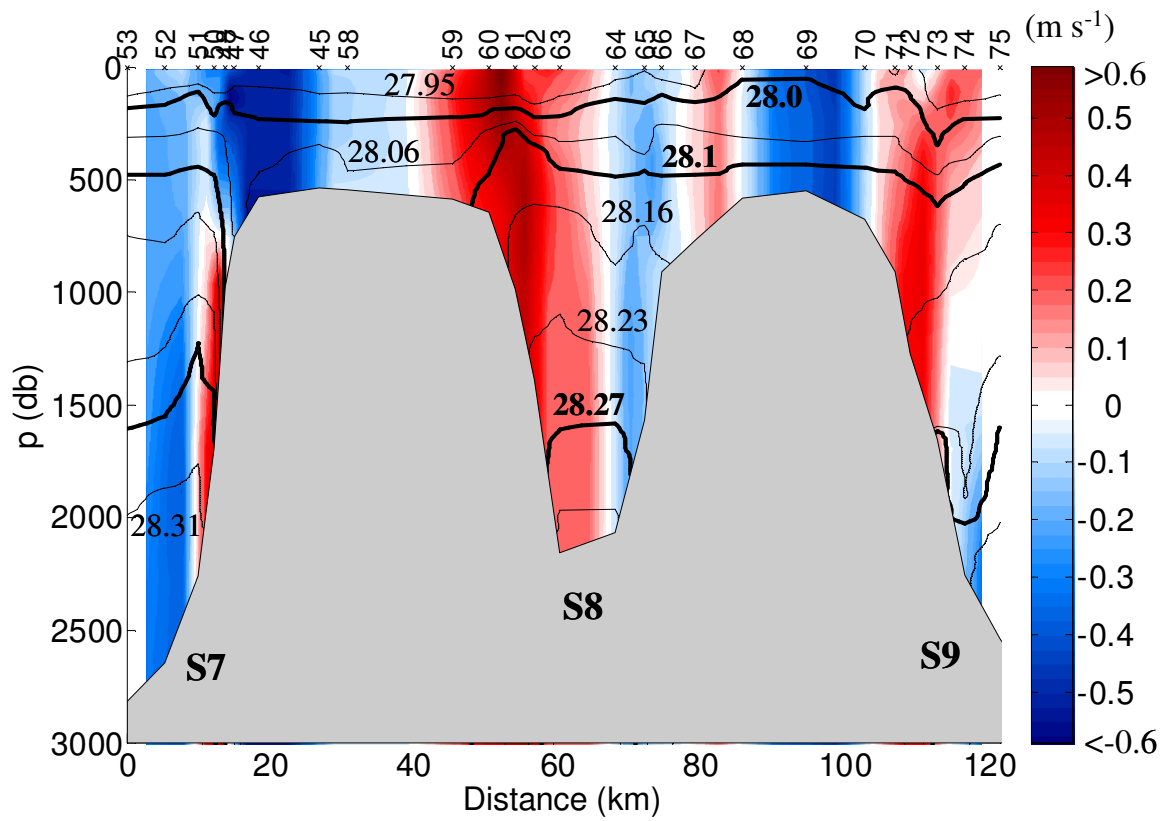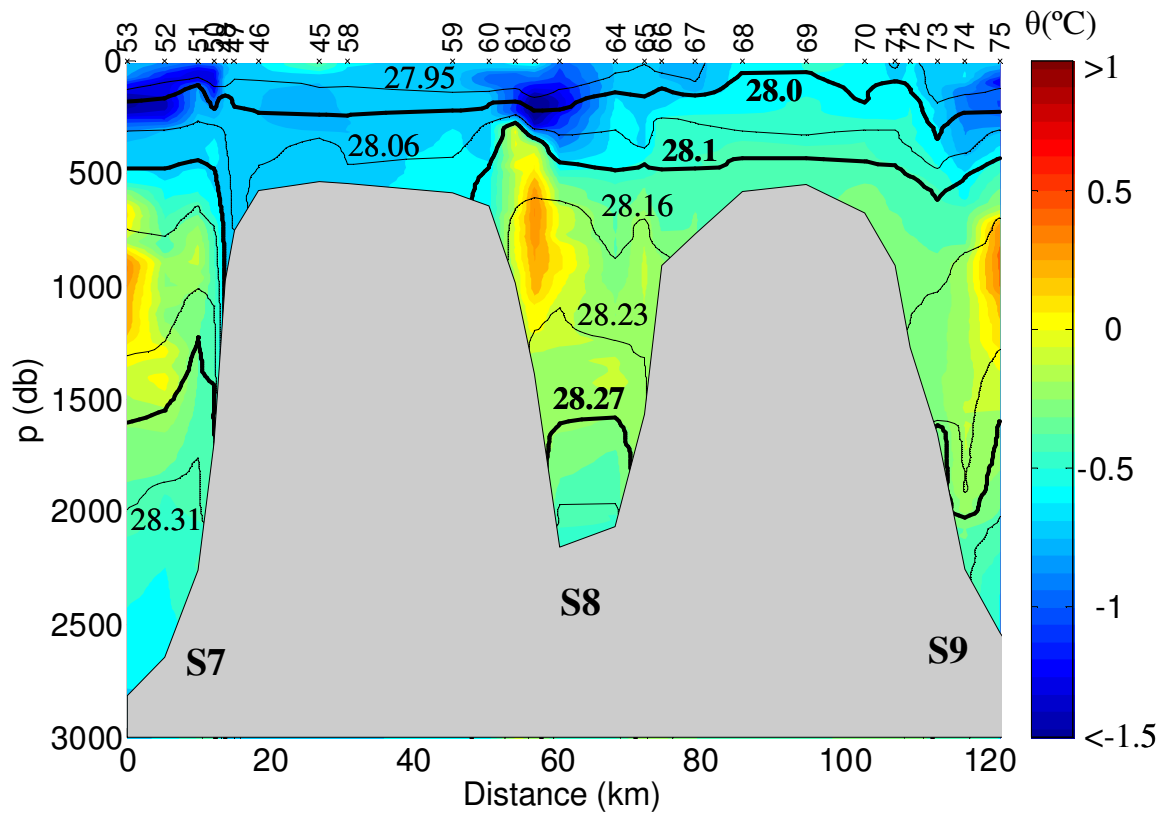
The potential temperature distribution and the velocity field are shown in the upper and lower panels of Fig. 5.2, respectively. The upper panel shows AASW occupying the upper layers, the relatively warm WDW filling the middle depths, and WSDW occupying the lower levels of all the sections. As part of the AASW, the cold remnants of the winter mixed layer (Winter Water, WW, Mosby, 1934) are observed overlying the warmest, less modified cores of WDW, roughly over the 28.0 kg m^{-3} neutral density and limited to the offshore side of the slope frontal structure. WW is observed over the upper slope in section S7 and western side of section S8, but seawards in section S9.

In section S7, a 'V' shape structure described by the 28.06 kg m^{-3} isopycnal is well apparent (casts 46 to 51, Fig. 5.2). This ribbon of relatively cold and fresh water related to the ASC (Gill, 1973) flows along the shelf break (over the 700m isobath). The tilting of this isopycnal together with the velocity field (lower panel of Fig. 5.2) will be determinant to trace the pathway of the ASC downstream. In spite of the "V" shape, the surface water overlying the continental shelf is not cold and dense enough to be recently formed Shelf Water (SW). There are no evidences of bottom water formation.

The offshore side of the front extends about 5km between the 700m and 2200m isobaths (casts 47 to 51, Fig. 5.2). The neutral density change at 700 db is from 28.06 to 28.17 kg m^{-3}, with properties ranging seaward from -0.66 ºC to -0.26 ºC in temperature, from 34.51 to 34.61 in salinity, and from 274 to 242 µmol kg^{-1} (6.3 - 5.6 ml l^{-1}) in dissolved oxygen (Fig. 5.3). Note that in this section the 0ºC isotherm is not an appropriate indicator to locate the ASF (as noted in Heywood et al., 2004): here the front separates surface water from a colder (<-0.1ºC, cast 51) and fresher modification of WDW, the 0ºC isotherm being located at open sea (cast 53, Fig. 5.2).

The transport associated with the ASC has been computed in section S7 integrating the velocity field from cast 45 (over the 500m isobath) to cast 51 (over the 2200m isobath), which makes a total width of 17km. The net value obtained is 3.2 ± 0.3 Sv, similar to the 3.9 ± 0.3 Sv given by Thompson and Heywood (2008) at the tip of the Antarctic Peninsula considering an ASC 35km wide (between the 500m and 1300m isobaths). Part of the net flow (-0.8 ± 0.5 Sv) belongs to the undercurrent observed at the offshore side of the ASF, below the 28.1 kg m^{-3} isopycnal (casts 48 to 51, Fig. 5.3), so that the northward flow really

amounts to 4 Sv. Previous studies had described the presence of bottom undercurrents further upstream (Fahrbach et al., 1994; Heywood et al., 1998; Chavanne et al., 2010), but not at the southern flank of the ridge. We have also estimated the transport associated with the deeper, offshore current crossing between casts 51 (2200m) and 53 (2800m), which could be part of the flow associated with the WF. We obtained 6.6 ± 0.4 Sv, of which 3.4 ± 0.4 Sv would correspond to WSDW. A total of 16.8 ± 1.9 Sv was estimated by Thompson and Heywood (2008) at the tip of the Antarctic Peninsula (see their Fig. 11).
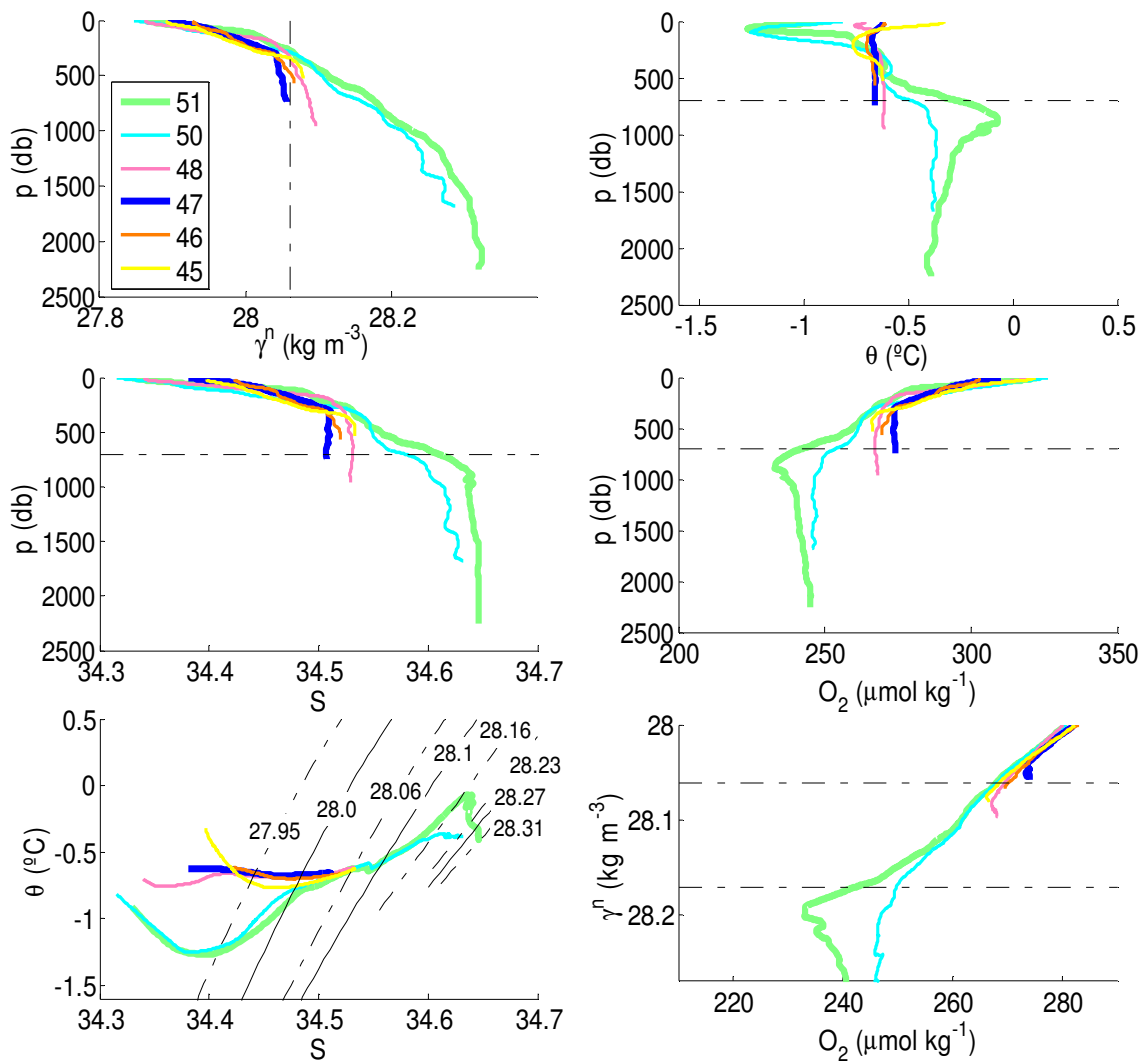
Figure 5.3. Profiles from ESASSI Section S7. Upper and middle panels: neutral density, potential temperature, salinity, and dissolved oxygen. Lower panels: Potential temperature vs. salinity (with neutral density curves overplotted) and neutral density vs. dissolved oxygen diagrams; in the latter the dashed lines denote the 28.06 and 28.17 kg m^{-3} isopycnals).

The strong tidal currents measured at narrow topographic gaps (see Figs. 2.7 and 2.8 in Chapter 2) would be responsible for inshore and offshore displacements of the frontal structure. At section S8 the maximum tilting is again observed for the 28.06 kg m^{-3} isopycnal, but this is now located 5km inshore from the shelf break (cast 59, over the 400m isobath). This spatial variability contrasts with the only 2km variations in the location of the ASF reported by Thompson and Heywood (2008) along the tip of the Antarctic Peninsula. Another important difference with respect to section S7 is that in section S8 tidal currents would have pushed WDW towards the slope, making the frontal structure to separate surface water from actual WDW (cast 62, 1400m) and not from a colder and fresher modification of WDW as in section S7. At section S8 the property gradients across the frontal structure range from 28.06 kg m^{-3} (cast 59, 400m) to 28.13 kg m^{-3} (cast 62) for neutral density, from -0.58 ºC to -0.02 ºC for temperature, from 34.52 to 34.61 for salinity and from 271 to 231 µmol kg^{-1} (6.2 - 5.3 ml l^{-1}) for dissolved oxygen (Fig. 5.4).

Regarding the transport associated with the ASC, the observations suggest a bifurcation of the flow within the gap sampled by section S8. On the western slope, the transport between cast 58 (over the 500m isobath, see the lower panel of Fig. 5.2) and cast 62 (separated 26km from the first, over the 1400m isobath) has been estimated in 3.9 ± 0.5 Sv. That is, all the flow associated with the ASC measured at section S7 would cross section S8 northwards flowing on its western slope. However, Fig. 5.2 also suggests that part of the flow recirculates and crosses again section S8, but now flowing southwards on the eastern slope of the gap. The weaker "V" shape of the 28.06 kg m^{-3} isopycnal indicates that this takes place between cast 67 (over the 800m isobath) and cast 64 (separated 11km from the first, over the 2000m isobaths). Summarizing, while the shallowest part of the current would progress northwards across the gap located at 51ºW, the offshore part would continue flowing eastwards along the slope of the southern flank of the ridge.

The transport associated with the offshore branch of the ASC has been estimated in 1.5 ± 0.3 Sv (about a half of the total transport measured in section S7). It continues along the slope of the southern flank of the ridge until the next passage, located at 50ºW and sampled by section S9 (see Fig. 5.1 for its location). In that section the ASC is found more offshore than upstream, flowing along the 1500-1600m isobaths (cast 73, see Fig. 5.2).

The properties of the water carried by the ASC have changed very slightly during its progression to the East: from cast 65 to cast 73 the temperature changes from – 0.58 ºC to -0.46 ºC, the salinity from 34.53 to 34.54 and the oxygen remains more or less constant (261-260 µmol kg^{-1}, 6.0 ml l^{-1}).
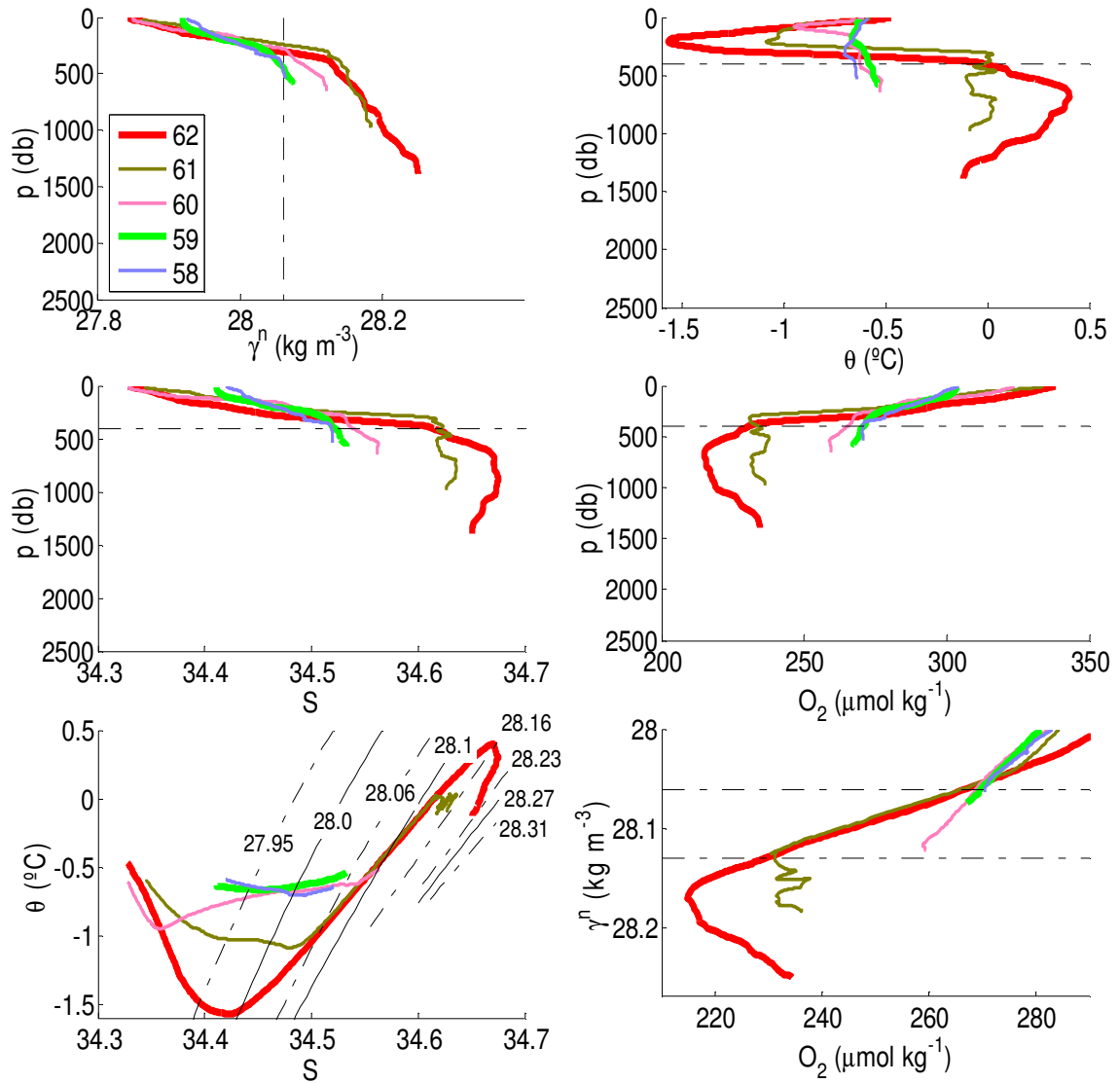
Figure 5.4. *Profiles from the western slope of ESASSI section S8. Upper and middle panels: neutral density, potential temperature, salinity, and dissolved oxygen profiles. Lower panels: Potential temperature vs. salinity (with neutral density curves overplotted) and neutral density vs. dissolved oxygen diagrams; in the latter the dashed lines denote the 28.06 and 28.13 kg m^{-3} isopycnals.*

5.3 The Antarctic Slope Current at the northern flank of the South Scotia Ridge

At the southern flank of the ridge the ASC has been observed to split into two branches, the shallower one following the 700m isobath and the offshore branch following the 1600m isobath. Here we will look for both branches further downstream, at the northern flank of the ridge.

The potential temperature distribution and the velocity field across the gaps of the northern flank of the ridge (sections S4, S5, and S10, see Fig. 5.1) are shown in the upper and lower panels of Fig. 5.5, respectively. Intense velocities and a sharp tilting of the 28.06 kg m^{-3} isopycnal are observed over the western slope of section S5 (cast 87, over the 700m isobath). The properties observed over the 28.06 kg m^{-3} isopycnal (-0.46 ºC, 34.54, 263 µmol kg^{-1} (6.1 ml l^{-1})) lie within the horizontal property ranges characterizing the ASF at the southern flank of the ridge. The gap sampled by section S5 is not deep enough to allow the outflow of the offshore branch of the ASC that enters the ridge through the 50ºW gap (section S9, see Fig. 5.1 and 5.2). Instead, we suggest that it corresponds to the shallower branch of the ASC that crossed the southern flank through the gap located at 51ºW (section S8, see Figs. 5.1 and 5.2) and that it reaches section S5 after surrounding the Hesperides Trough. The northward progression of the ASC around the trough cannot be proved from ESASSI sections. What we can say is that when the ASC reaches section S5 in the northern flank of the ridge, the horizontal gradients of the ASF are about 20% weaker in temperature and about 40% weaker in salinity and dissolved oxygen than when it crossed the gap of the southern flank (section S7 and western slope of section S8).

Figure 5.5 (next page). *Upper panel: potential temperature distribution along the northern flank of the SSR (ESASSI sections S4, S5, and S10, see Fig. 5.1). Lower panel: velocity field across the same sections. Positive velocities are directed into the paper (northwards). The ASC is apparent at stations 87 (section S5), and 33 and 29 (section S4). The solid lines overplotted on both panels are neutral density isopycnals.*
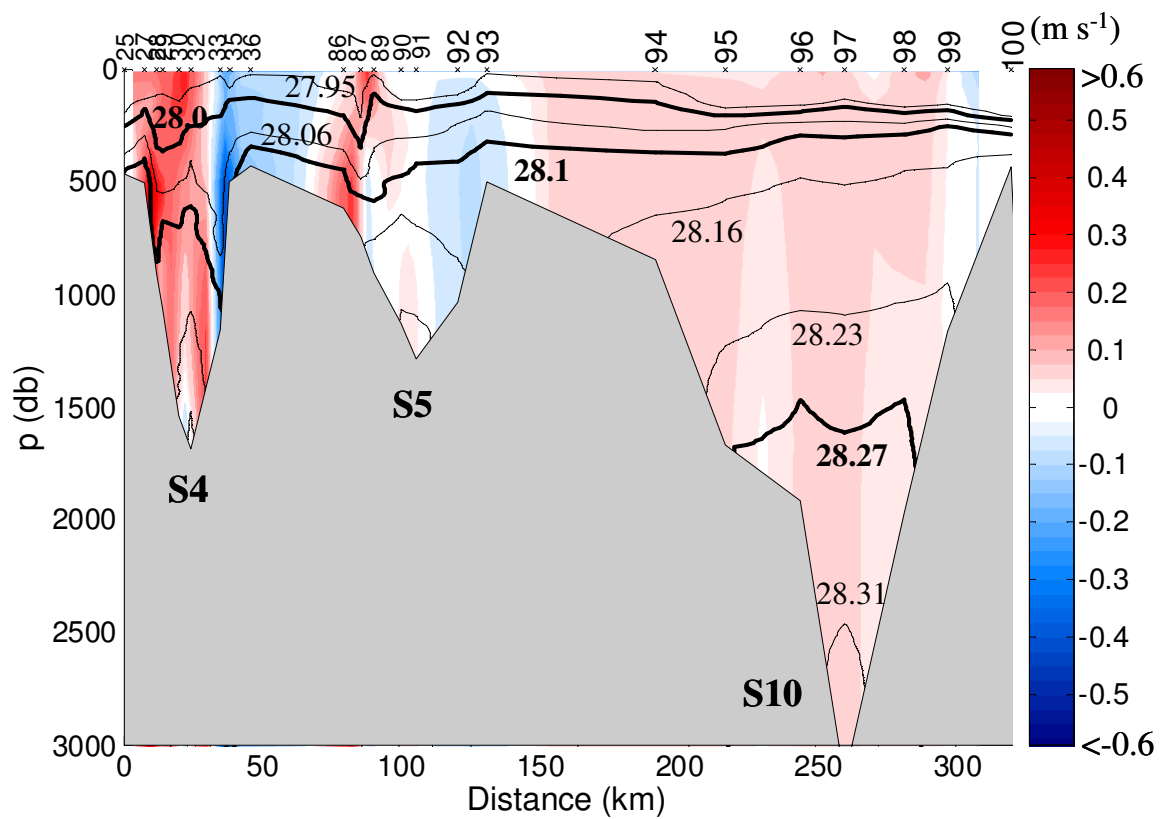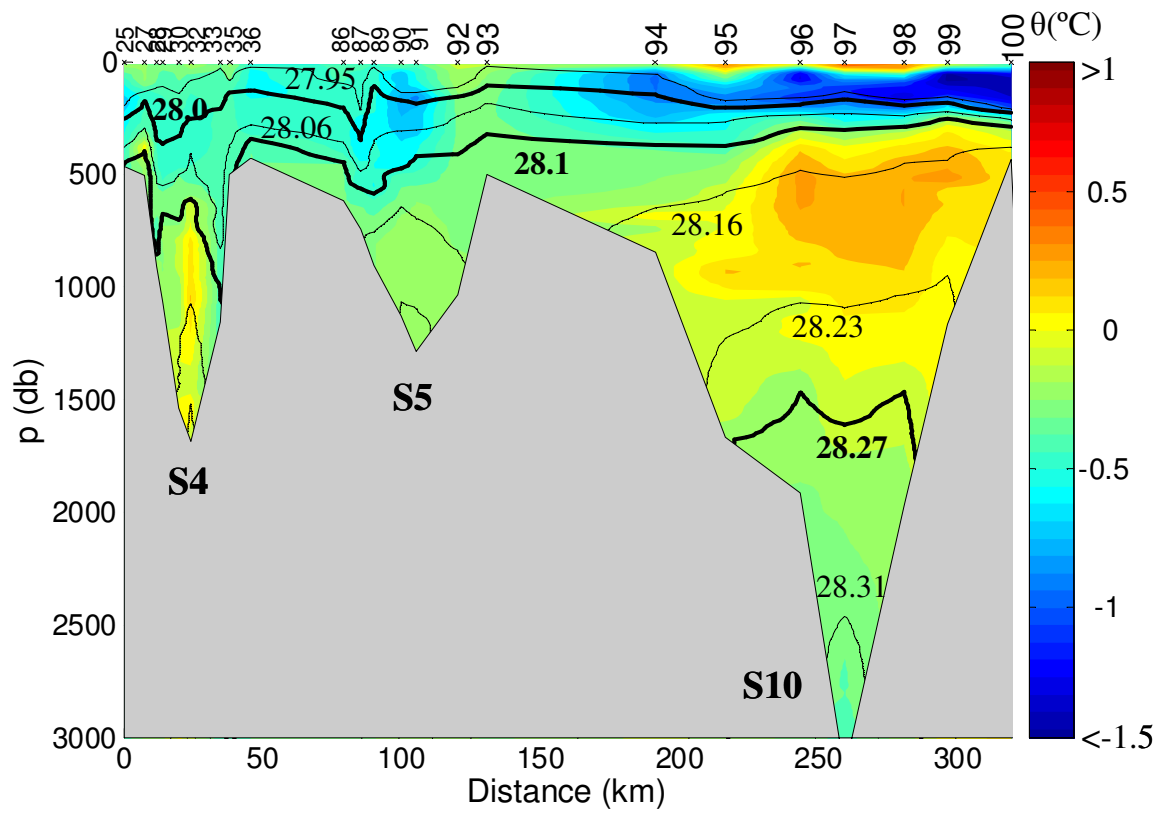
Section S4 (located at about 52ºW, see Figs. 5.1 and 5.5) also shows tilted isopycnals on both the western and eastern slopes of the gap. Our hypothesis is that the ASC does not overflow into the Scotia Sea across that gap, but only across the one sampled by section S5 (at 51ºW) as described above. However, once in the Scotia Sea flank of the ridge, the ASC would flow westwards, meandering within the gap sampled by section S4 (52ºW) more seaward than upstream (over the 1100m isobath, casts 33 and 29). Proving that hypothesis is not easy from the hydrographic data alone, as the gap sampled by section S4 shows intrusions of warmer open-sea waters that make difficult to establish the boundaries of the narrow ASC. It is then useful to check other quasi-conservative parameter as a tracer of the current such as PO_4^* (Broecker et al., 1998). Figure 5.6 shows that the PO_4^* concentrations of approximately 1.8 µmol kg^{-1} observed at the core of the ASC remain constant from the southern flank of the ridge (casts 47 and 48, section S7) to the northern flank (cast 87 of section S5, and casts 33-35 on the eastern slope of section S4). Instead, the lower PO_4^* concentration observed on the western slope of section S4 (1.7 µmol kg^{-1} over cast 29) suggest the influence of offshore, nutrient-poorer WDW. The high concentrations observed at the bottom of cast 35 (over the shelf, 500m depth) could correspond to fecal pellets in the sediment (Turner, 2002; Povero et al., 2003).

Estimating the transport associated within the outflow of the ASC into the Scotia Sea is not an easy task, because the frontal structure is weaker than upstream and at some locations it can hardly be separated from other regional circulation features. Moreover, the barotropic velocities estimated either from Rudnick's method or from the inverse model can change significantly in a few kilometers, making that small errors in the location of the frontal structure translate into significant discrepancies in the estimation of the flow. The net full-depth northward transport over the western slope of section S5 amounts to only 0.4 ± 0.3 Sv when computed from cast 86 (600m isobath) to cast 90 (separated 21km from the first, over the 1100m isobath). However, part of the transport could be missed because no station is located inshore beyond cast 86. Further downstream, on the eastern slope of section S4, the transport ranges between 1.0 ± 0.4 Sv when computed between cast 33 (1100m) and cast 35 (500m) and 1.5 ± 0.4 Sv when computed between cast 33 and cast 36 (400m). On the western slope of section S4 the transport is about 1.0 ± 0.2 Sv when computed from the 500m isobath (casts 25 or 27) to the 1100m isobath (cast 29). These results indicate that the shallower branch of the ASC would pour about 1 Sv of water into the Scotia Sea.
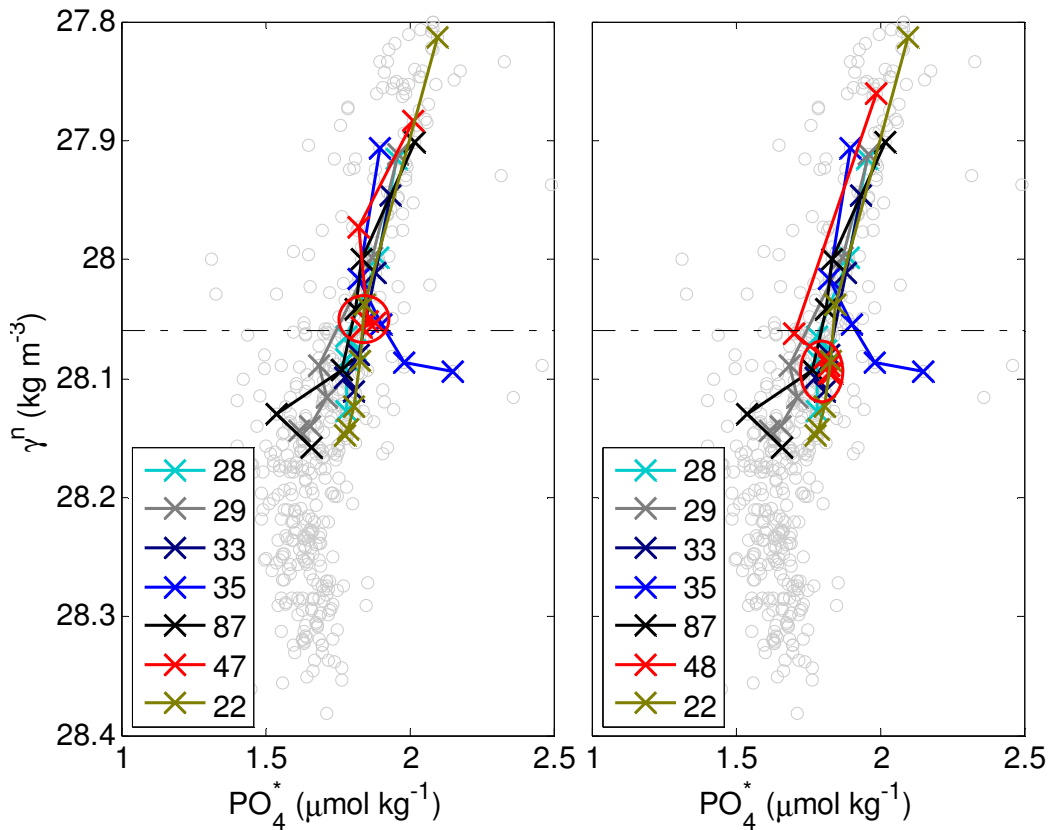
Figure 5.6. Phosphate star (PO_4^*) concentrations at different neutral density layers as observed within the ASC before it enters the South Scotia Ridge (station 47, section S7), when it outflows into the Scotia Sea (station 87, section S5) and on the eastern (stations 33, 35) and western (stations 28, 29) slopes of the gap sampled by section S4 (see Figs. 5.1, 5.2 and 5.5).

5.4. The inshore branch of the Antarctic Slope Current in the Scotia Sea

Three cross-slope sections located to the west of section S4 allow tracking the inshore branch of the ASC until the Shackleton Fracture Zone (sections S3, S2, and S1, Figs. 5.1 and 5.7). As it progresses westwards along the northern flank of the ridge, the narrow ASC is still linked to the 28.06 kg m^{-3} isopycnal, now presenting a smoother "V" shape than upstream and flowing over the 1100m isobath, about 3km seaward from the shelf break (cast 22, section S3, at 53ºW, see Fig. 5.7). Further to the West, at 55ºW, the topography guides the ASC more than 20km seaward (between cast 12 (900m) and cast 14 (2500m). At that point the transport is 0.7 ± 0.2 Sv and 0.8 ± 0.5 Sv, when computed over a 5km section (casts 24–21, section S3) and a 7km section (casts 12–14, section S2), respectively.
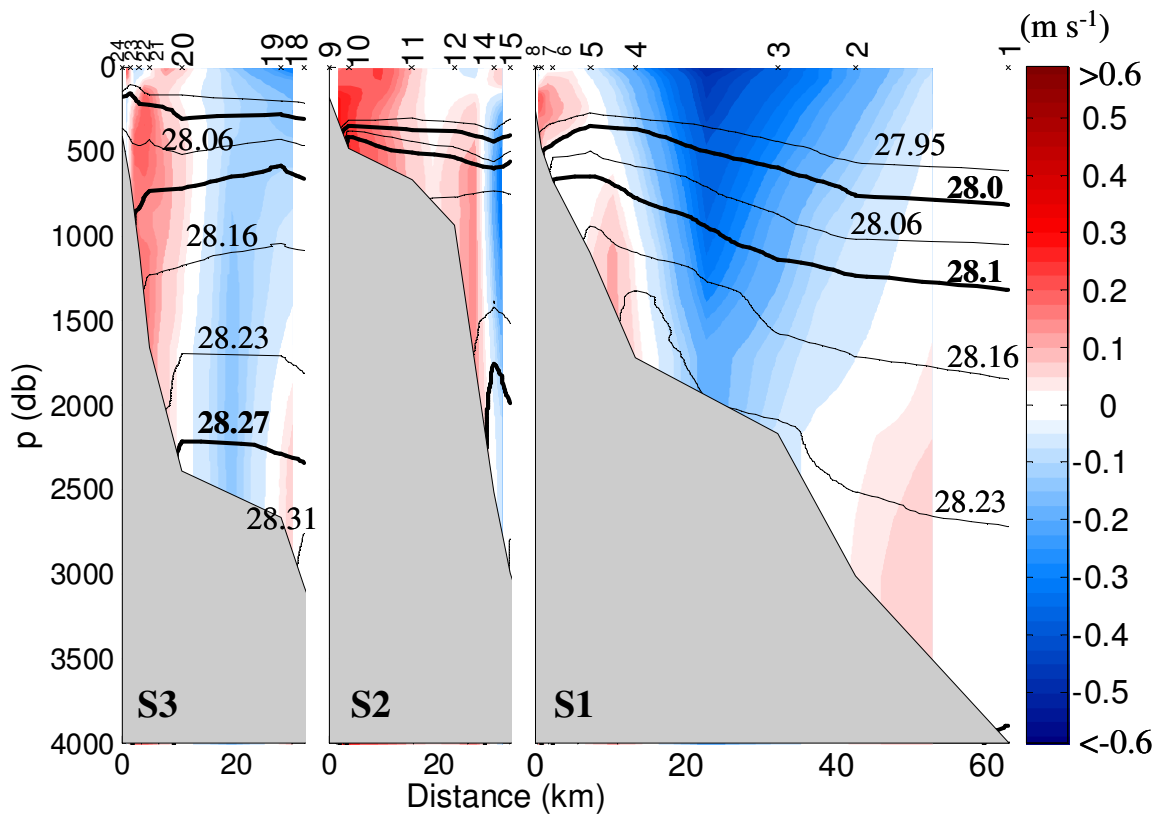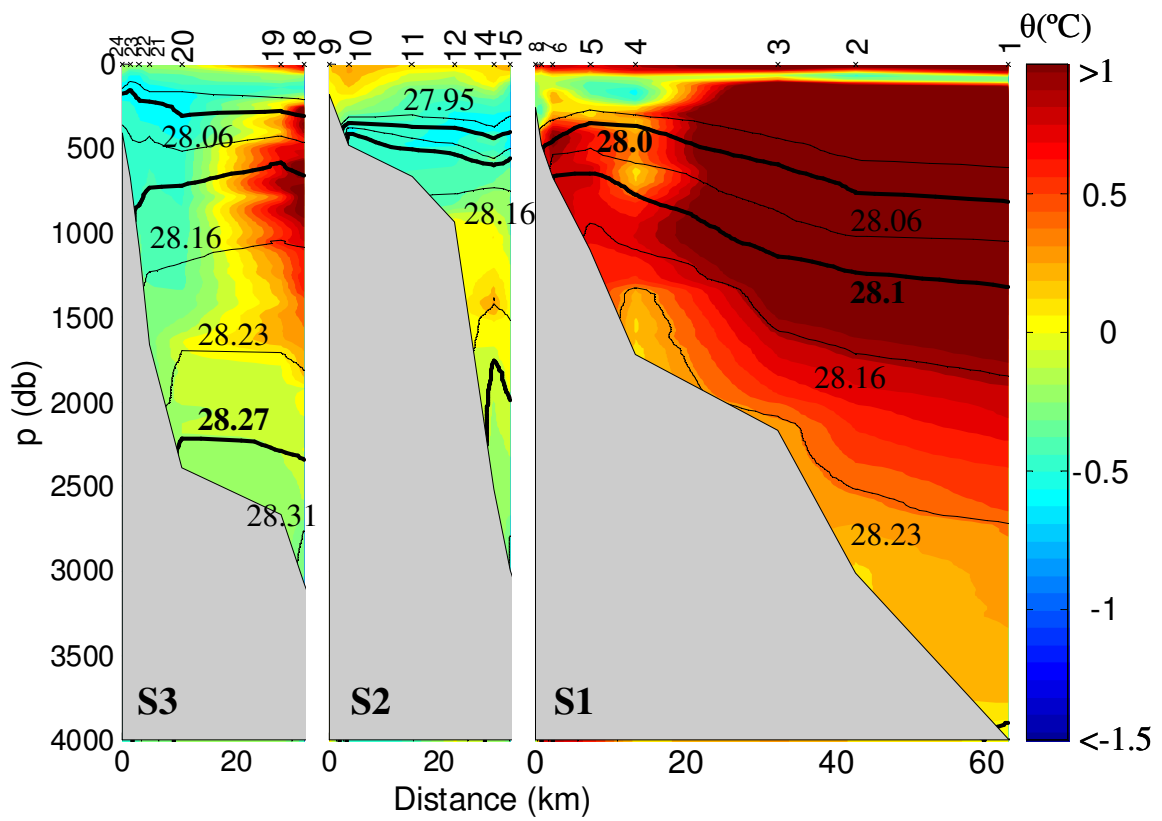
South of the Shackleton Fracture (at 56ºW, section S1, Fig. 5.7), the potential temperature distribution clearly shows the warm waters of the ACC ($\theta > 1$ºC). A sort of "V" shape structure is still observed in the temperature distribution, but not in the shape of the isopycnals. Moreover, the weak westward flow that is still observed at section S1 is no longer linked to the 28.06 kg m^{-3} isopycnal. This makes us to conclude that the ASF and its associated current are blocked before reaching the Shackleton Fracture Zone.

5.5. The offshore branch of the Antarctic Slope Current in the Scotia Sea

Following the fate of the deeper branch of the ASC that entered the southern flank of the ridge through the 50ºW gap is not as easy. The strong topographic constraint of the Hesperides Trough makes that also the deeper branch flows cyclonically around the trough, more or less over the 1600m isobath. However, this branch would be unable to follow the shallower one across the shallow gap of section S5; instead, it would continue eastwards flowing along the northern wall of the Hesperides Trough to spread afterwards into the Scotia Sea through the Hesperides Passage (see Fig. 5.1). That gap was sampled by a transect (S10) with a station separation of more than 20km (Fig. 5.5); thus, instead of trying to trace the current at section S10 it is better to look at some of the high resolution cross-slope sections located further downstream, on the northern flank of the ridge.

Figure 5.8 shows the potential temperature and velocity field of the two Scotia Sea cross-slope sections located to the west of the Hesperides Passage (sections S6 and S5N, see Fig. 5.1). As this second branch of the ASC is not linked to the upper slope, its path is more complicated to follow. We will do it tracing the water mass properties and looking at the velocity jets observed along the 1600m isobath (Fig. 5.9).
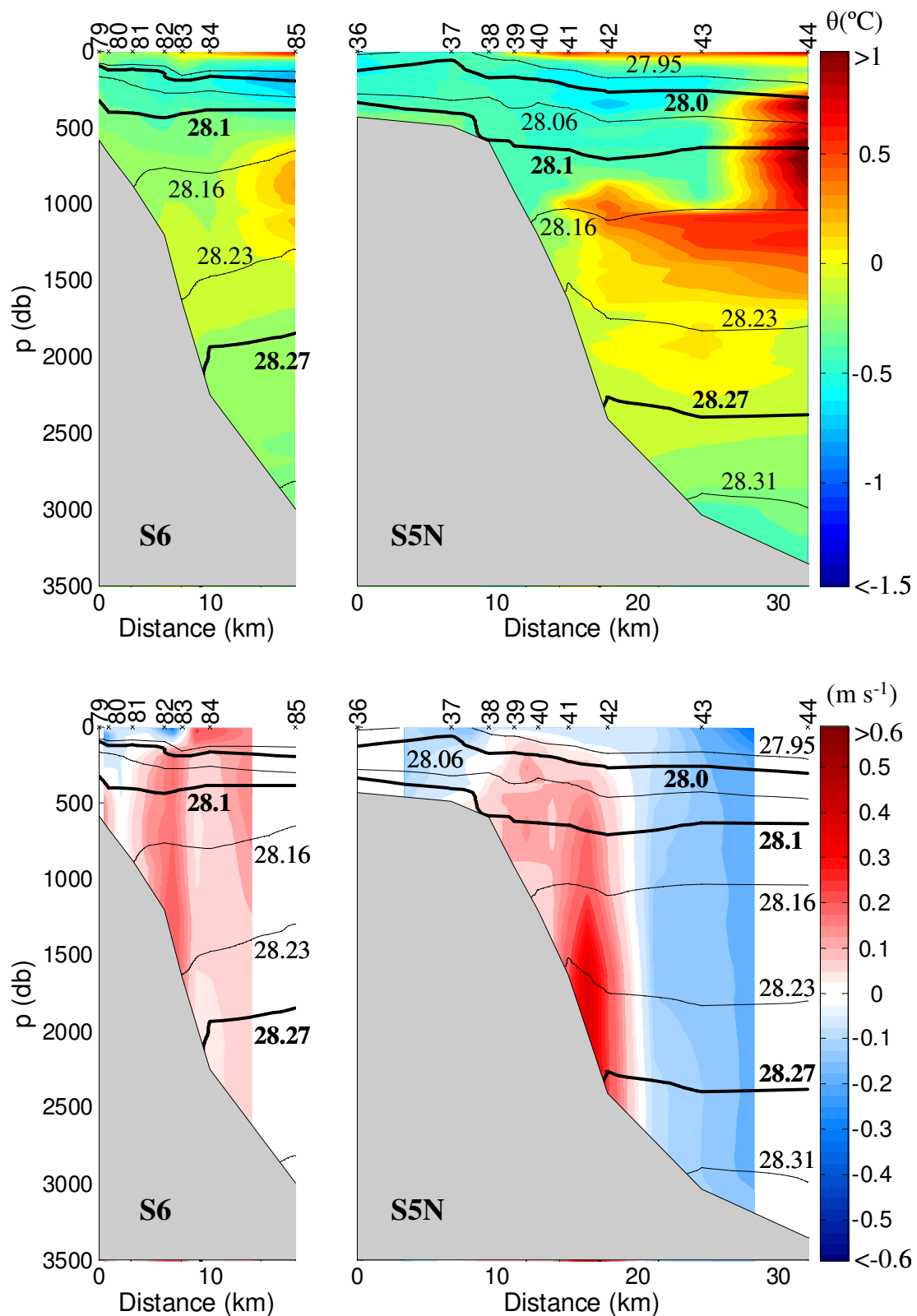
Figure 5.8. *Upper panel: potential temperature distribution over two cross-slope sections located at the northern flank of the SSR (ESASSI sections S6 and S5N). Lower panel: velocity field across the same sections. Positive velocities are directed into the paper (westward). The solid lines overplotted on both panels are neutral density isopycnals.*
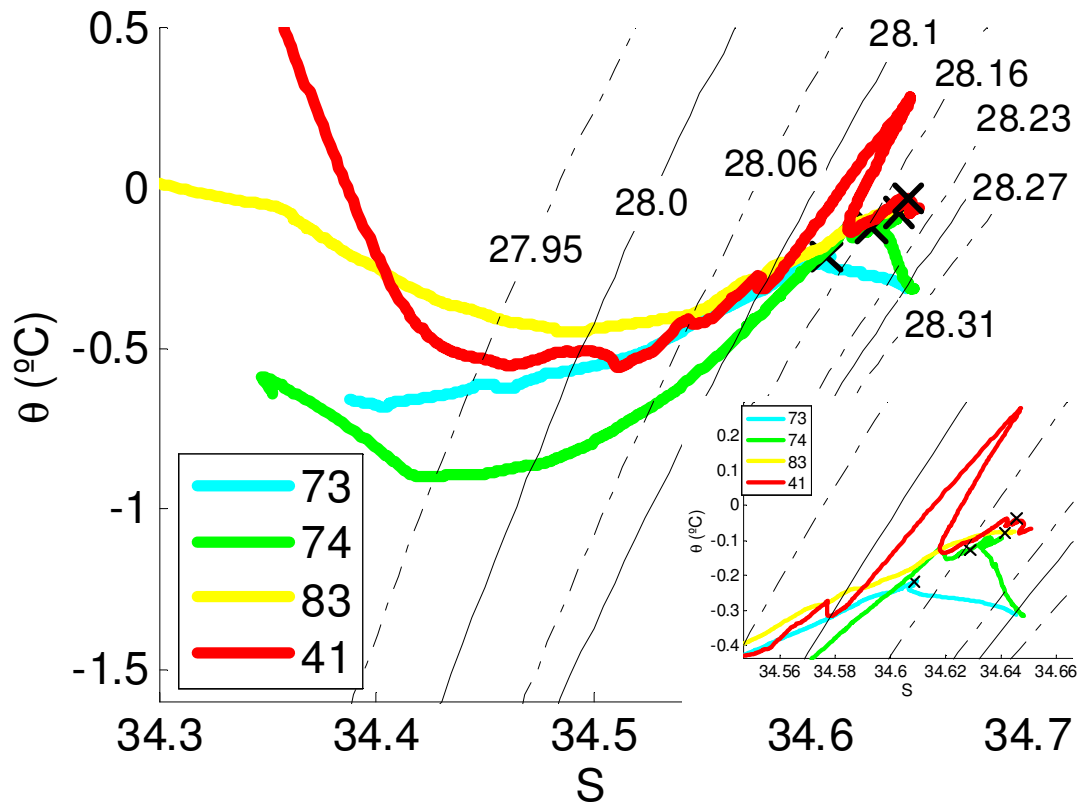
Figure 5.9. *Potential temperature vs. salinity diagram. Casts 73 and 74 are from section S9 (southern flank of the SSR), cast 83 is from section S6 (Scotia Sea), and cast 41 is from section S5N (also in the Scotia Sea). The black crosses locate the 1400m level. Neutral density isopycnals are indicated by dash-dot and solid thin lines.*

The eroded core of modified WDW located below 1400m and related to the offshore branch of the ASC (see the black crosses in Fig. 5.9) can be traced by comparing the profiles observed at 50ºW at the southern flank of the ridge (casts 73-74, 1600-2200m, section S9, see Figs. 5.1 and 5.9) with the profiles located over the 1600m isobath in the Scotia Sea side of the northern flank (50ºW, cast 83, section S6; 52ºW, cast 41, section S5N, see Figs. 5.1 and 5.9). Moreover, the velocity distribution over section S6 (lower panel of Fig. 5.8) shows a jet centered over the 1600m isobath (cast 83). The transport amounts to 0.6 ± 0.3 Sv when it is computed between casts 82 (1200m) and cast 84 (separated 4km from the first and located over the 2200m isobath). The water carried over the 28.06 kg m^{-3} isopycnal surface (i.e. AASW) is as fresher and ventilated as when it entered the southern flank of the ridge (cast 73, section S9), but slightly warmer (-0.40ºC).

More to the west, section S5N (52ºW, Fig. 5.8) shows evidences of both, the shallower branch of the ASC that has crossed section S5 (cast 39, 900m) and a jet linked to the 1600m isobath (cast 41). However, at that point the jet also carries water with properties too different to be related to the offshore branch of the ASC. Our hypothesis is that the deeper branch of the ASC outflows into the Scotia Sea through the Hesperides Passage and then it dilutes into the regional circulation well before the gap crossed by the shallower branch.

5.6 Conclusions

During the ESASSI cruise the different gaps indenting the western sector of the SSR were sampled with an unprecedented spatial resolution. This has allowed tracing the ASF/ASC system across the southern and northern flanks of the SSR. Before entering the ridge, the ASC carries 3-4 Sv of relatively cold (-0.66 ºC), fresh (34.51), and oxygen-rich (274 µmol kg^{-1}, 6.3 ml l^{-1}) water, with a jet centered over the 700m isobath. This transport value is about a half of that obtained by Heywood et al. (2004). The reason is probably that the spatial resolution of their section (35km) prevented a clear delimitation of the boundaries of the ASF. In a more recent work, Thompson and Heywood (2008) also obtained smaller values (3.9 ± 0.3 Sv) across a section located at the southwestern rim of the Powell Basin.

The shallowest part of the flow (about a half of the total transport) enters the SSR through the 51ºW gap; by the time of the ESASSI-08 sampling the ASC flows almost entirely over the western continental shelf, due to the effect of strong tidal currents. The deeper branch continues eastwards flowing over the 1600m isobath of the southern flank of the ridge and turns northwards later on, at 50ºW (the path suggested by Heywood et al., 2004).

Both branches of the ASC surround the Hesperides Trough, their steep slopes acting as a strong topographic guide (Palmer et al., 2012). The shallowest branch outflows into the Scotia Sea through the gap located at 51ºW, where it flows westwards over the 1100m isobath and weakens until it is blocked by the Southern Boundary of the ACC to the South of the Shackleton Fracture. The second, deeper branch would escape further East, through

the Hesperides Passage; after turning to the west with the core of the jet still centered over the 1600m isobath it would widen seawards and disappear within the regional circulation. Thus the deep branch of the ASC would not reach the 51ºW gap through which the shallower branch outflows into the Scotia Sea. The pathway of the ASC is summarized in Fig. 5.10.
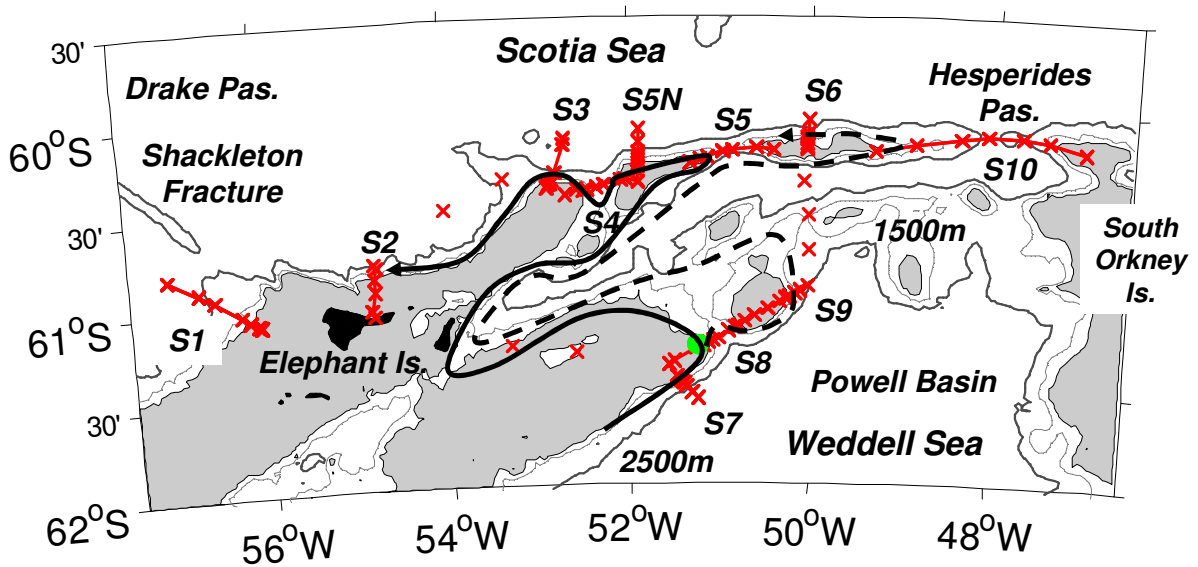
Figure 5.10*. Schematic pathways of the ASC over the SSR as observed during the ESASSI cruise. The solid line denotes the shallower branch of the ASC (centered over the 600-700m isobaths), while the dashed line denotes the deeper branch (centered over the 1600m isobath).*

CHAPTER 6

DIAPYCNAL AND ISOPYCNAL MIXING IN THE WESTERN SECTOR OF THE SOUTH SCOTIA RIDGE (SSR)

6.1. Introduction

The continental margin of Antarctica is an appropriate region for water mass formation due to mixing processes between seaward and coastal water masses (Gill, 1973). The main exchanges of heat, gases, and nutrients take place in the ocean-atmosphere and ocean-ice interfaces and result in different temperature, salinity, and concentrations in a variety of biochemical properties that characterize the newly formed water masses. Their density relative to the surrounding waters and the presence of currents determine the formation of new water masses and their fate into the ocean. The temporal scales differ significantly between the atmosphere and the ocean interior; a generally slower variability of water mass properties in the ocean interior allows their tracking (Tomczak, 1999).

Some of the most important places of Antarctica regarding water mass formation are the environs of the ice-shelves, where cold (near freezing point), high salinity, dense water (Shelf Water, SW, Whitworth et al., 1998) overrides the shelf break, flows downslope and mixes with offshore waters to form Antarctic Bottom Water (Foster and Carmack, 1976). Mixing processes taking place downstream of the formation regions modify the newly formed water masses as they progress along the Weddell Sea continental margin (Gill, 1973). Water masses are continuously modified by different types of mixing (depending on the region and season) until they outflow into the Scotia Sea through the gaps of the South Scotia Ridge (SSR).

Patterson and Sievers (1980) addressed the processes related to the anomalous signature in different properties observed in the western sector of the SSR. According to these authors, convection processes during wintertime are responsible for the vertical mixing observed in the upper layer, where properties from air/sea/ice interactions are pumped downward and achieve the bottom layers of the shallower areas of the region. Vertical mixing was also

observed in summer, but salinity values were higher than those expected from near-surface processes, dominated at that time by sea-ice melting. Patterson and Sievers (1980) suggested that the anomalously high salinities could be due to bottom and lateral Ekman friction processes taking place at the continental margin and noted that those processes could act all year-long because they do not require vertical instability. The classical Ekman theory (Ekman, 1905) states that the thickness of the bottom boundary layer (BBL) at the SSR latitudes should be within the range 50-150m for a constant eddy viscosity between $10^{-2}-10^{-1}$ m^2s^{-1}. Considering a vertical eddy viscosity proportional to the distance to the bottom results in veering angles closer to observations, but the thickness of the BBL remains similar (Cushman-Roisin and Malačič, 1997). Perlin et al. (2007) showed that a second order polynomial expression for the eddy viscosity allowed a better approach to observations recovered at different places. All these theories were based on the assumption of a flat bottom.

In the Southern Ocean, different studies were developed considering a non-flat bottom, in order to account for the processes taking place at the continental slope. Killworth (1977) and many authors thereafter (e.g. Baines, 2009) have described the mechanisms involved in downsloping plumes of dense SW overridding the slope to achieve a new stability state when lighter WDW approaches the continental shelf. Such mechanisms are rather different from the Ekman processes suggested by the preliminary studies by Patterson and Sievers (1980).

In the present work we study the different frictional processes taking place before the Antarctic Slope Current reaches the southern gaps of the SSR region and when it crosses the SSR to outflow into the Scotia Sea. First we will focus on the bottom layer of the Antarctic Slope Front (ASF), showing that frictional processes can result in vertical turbulence and cross-slope lateral mixing that are responsible for the exchange of properties along the continental slope before the current reaches the southern gaps of the SSR region. Our starting points will be, on one hand, the stability of the stratification observed in summer when running downslope along the bottom boundary layer of the continental shelf and slope, and on the other hand, the apparent mixed layers observed close to the bottom in the vertical profiles, which are thicker than those predicted by the classical Ekman layer theory. In particular we will show that these local processes

contribute to the formation and maintenance of the colder, fresher, oxygen-richer branch of Modified Warm Deep Water (i.e. modified Circumpolar Deep Water from the Weddell Sea; Whitworth et al., 1998) at locations far from the ice-shelves and without involving downslope dense water plumes. Finally, we will focus on the lateral mixing along isopycnals that takes place away from the bottom boundary layer.

The structure of this chapter is as follows. A brief description of the methodology used to determine the mixing processes is presented in Section 6.2. The results are analyzed for three different regions. In Section 6.3 we analyze the diapycnal mixing taking place at the bottom layer of the ASF before the frontal current reaches the southern flank of the SSR. In Section 6.4 we study the isopycnal mixing observed at the southern flank of the SSR, paying particular attention to the modification of the WDW core over the western slope of the southern 51ºW gap, where strong tidal currents are detected. In Section 6.5 we focus on the Hesperides Trough, where isopycnal mixing is thought to be the predominant mechanism for subsurface and WDW layers. Last, in Sections 6.6 and 6.7, we obtain the mixing fractions when these waters outflow into the Scotia Sea and meet first the waters coming from the Orkney Passage and later the waters coming from the Drake Passage (at the Southern Boundary of the ACC). Conclusions are outlined in Section 6.8 and Tables are presented in the Appendix (Section 6.9).

6.2. Methodology

The local degree of mixing between the different water masses is estimated by applying an Optimum Multiparameter Analysis (OMP) to the data set collected during the ESASSI-08 cruise (see Fig. 6.1). Away from the interaction with the atmosphere and ice, the contact between different water masses can result in a new water mass with properties in between those of the source water masses. On a potential temperature - salinity (θS) diagram (Mamayev, 1975), a water mass would be strictly defined by a point, though in practice it is usually defined by a small area. A hydrographical profile running along the water column usually samples several water masses, so that on a θS diagram it can reflect both, the representative cores of the sampled water masses and long lines describing the property gradients between adjacent water masses in the water column (e.g. Emery, 2003).

Figure 6.1. *ESASSI-08 hydrographic sections (red lines in the upper panel) and stations (crosses in the lower panels). The blue squares are the ESASSI-08 stations referred to in Fig 4a and the cyan diamond is the ESASSI-08 yo-yo station. Historical stations in the Powell Basin and Drake Passage selected from the Southern Ocean Atlas database (Orsi and Whitworth., 2005) are depicted as green diamonds in the upper panel. The bathymetry is from Smith and Sandwell (1997); the areas shallower than 1000m are shaded.*

The Optimum Multiparameter analysis implemented by Karstensen and Tomczak (1998) bases on the inversion of a linear equation system that combines the properties of different source water masses to result in the properties observed at a given location. In large regions of the ocean or close to the main formation regions (e.g. the continental shelves of polar regions), several water masses can be involved in the formation of a new water mass. In those cases, where several source water masses are involved, not only temperature and

salinity, but also other tracers like oxygen and nutrients (accounting for the biological cycle) must be included in the property combination equations in order to achieve a determined or an over-determined system. This is not our case, however: we will get a determined or an over-determined system just by using temperature and salinity, and adding extra tracers will not give additional information. The obtained residuals will be even smaller than in other studies just by analyzing the observed water masses on the TS diagram. That will be possible using as many water types as possible in the description of the source water masses.

Two mixing recipes will be considered, one yielding a determined equation system and another one yielding an over-determined system. The first one assumes three source water masses involved in the mixing taking place at the bottom boundary layers of the continental slope: inshore AASW carried by the Antarctic Slope Current (ASC), WDW located closer to the bottom of the shelf break, and WSDW located over the slope. This mixing scheme aims to explain the colder, fresher WDW component observed over the continental slope before crossing the southern gaps of the SSR (see the vertices of the black triangle in Fig. 6.2) and it can be set in terms of the determined system of equations:

$$f_{shelf\ bottom}\left(\theta_{shelf\ bottom}-\overline{\theta}\right)+f_{shelf\ break}\left(\theta_{shelf\ break}-\overline{\theta}\right)+f_{bottom\ slope}\left(\theta_{bottom\ slope}-\overline{\theta}\right)=\left(\theta_{observed}-\overline{\theta}\right)$$

$$f_{shelf\ bottom}\left(S_{shelf\ bottom}-\overline{S}\right)+f_{shelf\ break}\left(S_{shelf\ break}-\overline{S}\right)+f_{bottom\ slope}\left(S_{bottom\ slope}-\overline{S}\right)=\left(S_{observed}-\overline{S}\right) \qquad (6.1)$$

$$f_{shelf\ bottom}+f_{shelf\ break}+f_{bottom\ slope}=1$$

where ($\theta_{shelf\ bottom}$, $\theta_{shelf\ break}$, $\theta_{bottom\ slope}$) and ($S_{shelf\ bottom}$, $S_{shelf\ break}$, $S_{bottom\ slope}$) are the temperature and salinity defining the source water types, and ($\overline{\theta}$, $\overline{S}$) are the mean values among the source water types. The source water mass fractions are denoted by "f".

The second mixing recipe considered here is applicable to every neutral density level away from the bottom boundary layer. It involves only the inshore and offshore water types having the same density as the considered level. This scheme aims to explain the isopycnal mixing processes taking place at intermediate layers between recently modified water masses located close to the continental slope and offshore water masses (less modified WW/WDW in the Powell Basin or CDW in the Scotia Sea, see the black arrows in Fig. 6.2). The equation system is in that case over-determined:

$$\frac{1}{\sigma_\theta}\left(f_{inshore}\left(\theta_{inshore}-\overline{\theta}\right)+f_{offshore}\left(\theta_{offshore}-\overline{\theta}\right)\right)=\frac{1}{\sigma_\theta}\left(\theta_{observed}-\overline{\theta}\right)+R_\theta$$

$$\frac{1}{\sigma_S}\left(f_{inshore}\left(S_{inshore}-\overline{S}\right)+f_{offshore}\left(S_{offshore}-\overline{S}\right)\right)=\frac{1}{\sigma_S}\left(S_{observed}-\overline{S}\right)+R_S \qquad (6.2)$$

$$f_{inshore}+f_{offshore}=1+R_{mass}$$

where (σ_θ, σ_S) is the standard deviation among the source water types acting as a normalization factor between the θ, S residuals of the minimization, denoted here by R_θ, R_S. The meaning of the other symbols is as in (1). The same weighting factor is given to the temperature and salinity equations (Tomczak and Large, 1989) and to the water mass conservation equation (Budillon et al., 2003). This setting altogether with the selected local water types presented later on resulted in water type fractions with zero mass residuals for almost the whole set of values. The results shown for a given neutral density will be most of the times the mean value of several depth levels, but the standard deviation of the set of values is typically an order of magnitude smaller than the values themselves.

Over the SSR region west of the South Orkney Islands the properties of the offshore water types can be inferred from historical profiles (Orsi and Whitworth, 2005) located in the Powell Basin, to the South of the SSR (for WW and WDW; see Fig. 6.1) and to the southwest of the Shackleton Fracture, in the Drake Passage (for CDW; see Fig. 6.1). The intermediate levels of these two regions are filled by CDW and WDW, respectively (see Fig. 6.2). In our case the profiles from the Powell Basin were obtained by US and German cruises carried out in August 1997 and April 1998 on board the R/V Nathaniel B. Palmer and Polarstern, respectively. The profiles from the western Drake Passage were obtained during another US cruise carried out in October 1980 on board the R/V Atlantis II and during our ESASSI cruise in January 2008.

As inshore water types we consider the ESASSI profiles located at the ASF instead of historical data, because their properties could be more subject to seasonal or interannual variability, as shown in Orsi et al. (in preparation). The selected profiles are: cast 47 for the subsurface layer ($AASW_{ASC}$) and cast 50 for the intermediate water layer ($MWDW_{ASC}$) (see Figs. 6.1 and 6.2).

The Weddell Sea water masses that fill the Powell Basin mix with inshore water masses from the tip of the Antarctic Peninsula and shallower areas of the ridge as they flow along the continental slope and within the Hesperides Trough (Palmer et al., 2012). Once in the Scotia Sea they meet with Weddell Sea waters from the eastern gaps of the ridge (i.e. Orkney Passage; Naveira-Garabato et al., 2002a) and water masses from the Drake Passage. We will subsequently estimate the water mass fractions contributing to the subsurface and intermediate layers observed at the southern flank of the SSR, their modification within the Hesperides Trough, and the interaction with other water masses once in the Scotia Sea. The modification of WSDW has already been addressed in the previous chapter.
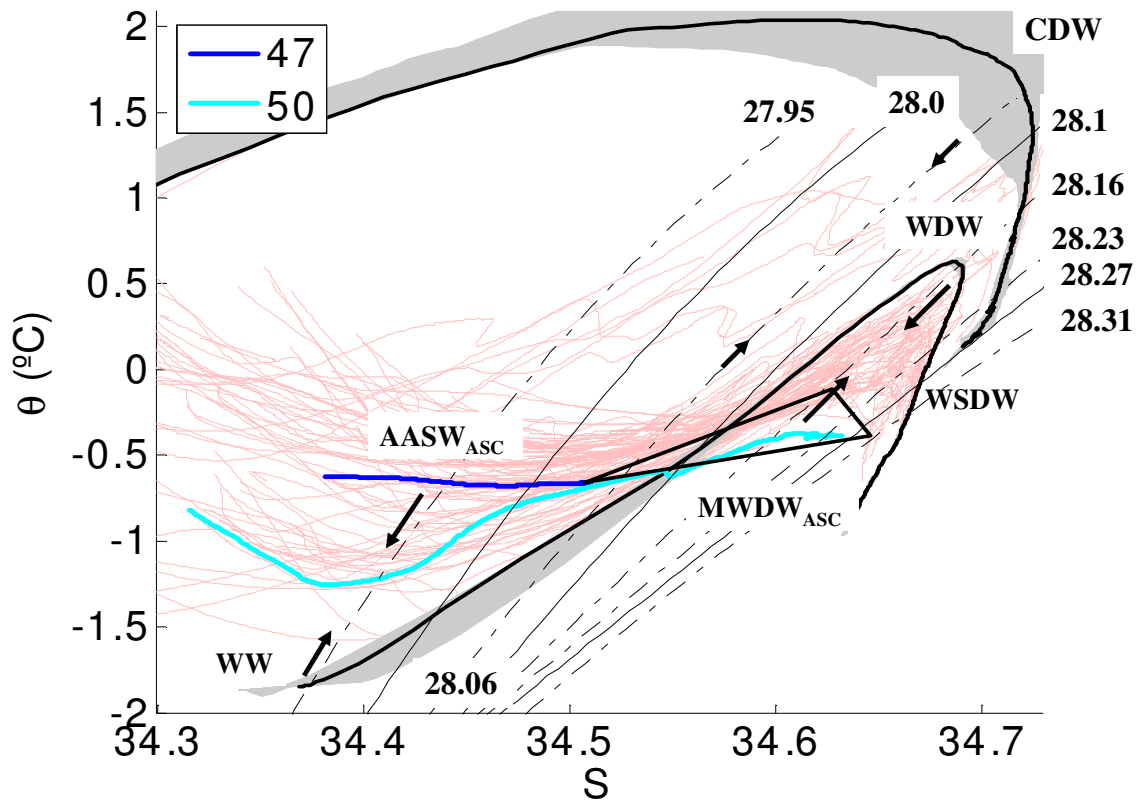
Figure 6.2. *Potential temperature vs. salinity diagram for the whole set of ESASSI-08 profiles (pink). The dark blue and cyan lines correspond to the selected inshore water types: AASW from cast 47; MWDW from cast 50, both located along section S7, see Fig. 6.1. The black lines and shaded areas represent the domain o the offshore water types: WW and WDW from the average profile of the Powell Basin and CDW from the southwestern part of Drake Passage. The arrows schematize isopycnal mixing processes. The vertices of the black triangle correspond to the three water types observed at the bottom boundary layer of the ASF. The solid and dashed lines indicate isopycnals.*

6.3. Mixing at the Antarctic Slope Front just before reaching the southern flank of the South Scotia Ridge

The cross-slope section S7 (see Fig. 6.1) is representative of the properties of the ASF and the associated ASC in the NW Weddell Sea, just before the gaps indenting the southern flank of the SSR. The ASF as observed in section S7 has already been shown in different figures (e.g. in Fig. 5.2), characterized by the pronounced tilting of isopycnals and with the associated ASC flowing over the 700m isobath. By getting back to this section we aim at identifying the factors that determine the properties of the deeper over-slope water mass. Pure isopycnal mixing processes cannot explain the relatively colder and fresher component of WDW observed there (MWDW$_{ASC}$; cast 50, 1700m, Fig. 6.3). The processes related to the formation of MWDW$_{ASC}$ at the bottom of the ASF need of the three-point diapycnal mixing recipe described in the previous section. Instead, away from the bottom boundary, the two-point isopycnal mixing recipe explains the modification of the cores of offshore WW and WDW as they mix with the inshore over-slope water masses of the ASC (AASW$_{ASC}$ and MWDW$_{ASC}$; see the black arrows of Fig. 6.3).

The first step for the three-point diapycnal mixing recipe is to infer the water type property distribution at the bottom levels of the over-slope profiles. The upper slope profiles present well-mixed bottom layers (shown as θS "points" in Fig. 6.3) that are much thicker than those predicted by the classical Ekman theory. Thus, where the ASC is about to cross the gaps of the southern flank of the SSR, the mixed boundary layers are as thick as 400-500m (casts 47-48, over depths of 700-1000m, section S7, Fig. 6.3; see e.g. the vertical structure of these profiles in Fig. 5.3, chapter 5). Moreover, a zoom in over these θS "points" (right bottom corner of Fig. 6.3) suggests the presence of turbulent processes.

The temperature and salinity values of the bottom mixed layer are -0.66ºC and 34.51 for cast 47 and -0.62 ºC and 34.53 for cast 48 (standard deviation of $O(10^{-3})$ for both parameters), resulting in maximum neutral densities of 28.06 and 28.10 kg m^{-3}, respectively. The potential temperature and salinity values corresponding to the 28.06 kg m^{-3} well-mixed bottom layer over the 700m isobath (cast 47) will be taken as representative of the lighter water type (AASW$_{shelf\ bottom}$) of the three-point mixing recipe.

From the upper level of the mixed layer up to the surface, cast 47 runs almost at constant temperature of -0.66 ± 0.02 ºC in the θS diagram (see Fig. 6.3), while salinity ranges from 34.38 at the surface to 34.51 at the bottom mixed layer. This constitutes the AASW carried by the ASC (AASW$_{ASC}$). The offshore cast 50 (over 1700m depth, Fig. 6.3) shows a similar pattern below the shelf break levels, that is an almost constant temperature (-0.38 ± 0.01 ºC) and a varying salinity (from 34.60 to 34.63). This constitutes the coldest and freshest modified WDW observed during the cruise (MWDW$_{ASC}$). The potential temperature and salinity taken as reference values for the less modified offshore WDW observed in the upper 800m are -0.12ºC and 34.63 (resulting in a density of 28.19 kg m^{-3}, casts 51-53, 2200-2800m, in Fig. 6.3). They will be considered as representative of the second water type (WDW$_{shelf\ break}$; S$_{shelf\ break}$, θ$_{shelf\ break}$) in the three-point mixing recipe. In fact this water type is in turn a mixture between AASW (~ 40%) and the non modified WDW observed at about 800m depth (~ 60%).

Deeper down the slope, the water that fills the bottom layer (from 1600 to 2200m, see cast 51, Fig. 6.3) is all represented by a single point in the θS diagram. This water is as colder (-0.38 ± 0.02 ºC) as that observed inshore (cast 50), but saltier (34.65) and therefore denser (28.31 kg m^{-3}) due to its depth. Below the 28.31 kg m^{-3} isopycnal, the limit between Upper and Lower WSDW (Arhan et al., 1999), all seaward profiles show the same θS values. Cast 52 shows a thin (2500-2600m) mixed bottom layer, but it doesn't influence the over-slope water mass properties. Cast 53 (2800m) shows no bottom mixed layer. The third water type (WSDW$_{bottom\ slope}$; S$_{bottom\ slope}$, θ$_{bottom\ slope}$) of the three-point mixing recipe will be therefore characterized by that point (-0.38ºC, 34.65) on the 28.31 kg m^{-3} isopycnal.

With the above definition for the source water types (the vertices of the black triangle depicted in Figs. 2 and 3), the water type fractions obtained from the application of the equation system (1) are as follows. The water filling the lower layer (400-1000m) of cast 48 is a mixture of 80% of reference AASW from the bottom mixed layer of cast 47 and 20% of WSDW. For the deeper cast 50, the bottom layer (1700m depth) is filled by a mixture of 80% of WSDW from the bottom of cast 51 (2200m). Above that level (at 800-1300m), the same cast 50 would consist of a mixture of 20-30% of AASW$_{shelf\ bottom}$, 20-30% of WDW$_{shelf\ break}$, and 50-60% of WSDW$_{bottom\ slope}$. The whole set of values is given in the Appendix, Table 6.1.
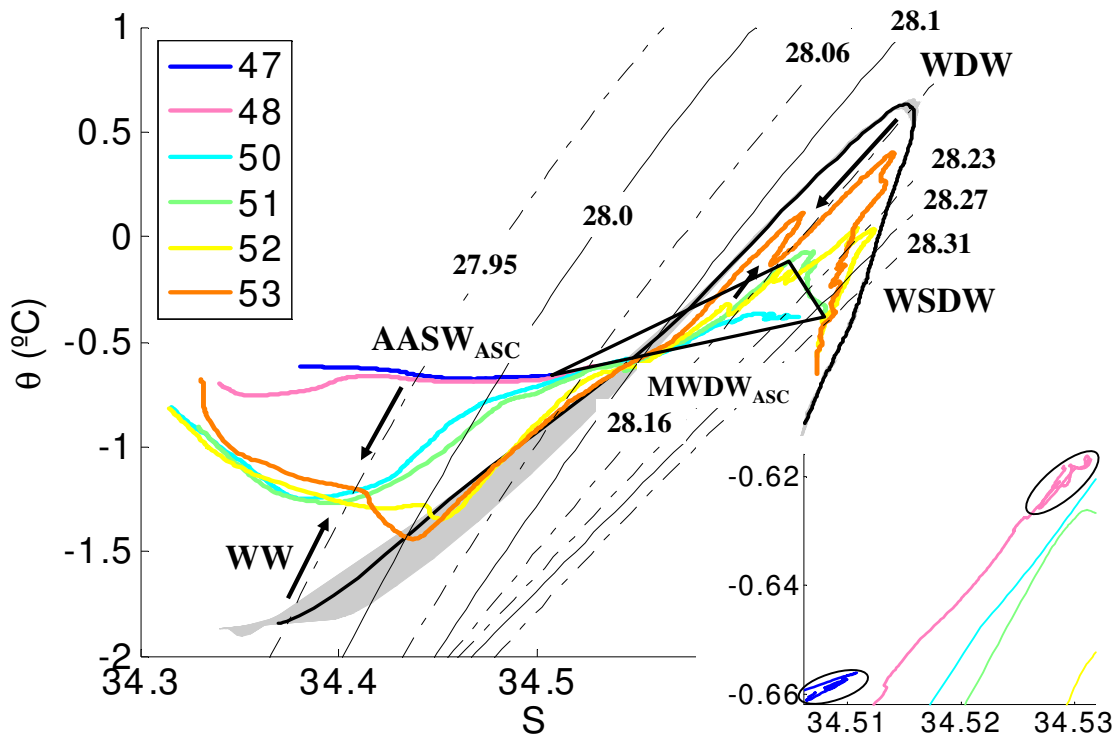
Figure 6.3. *Potential temperature vs. salinity diagram with the ESASSI profiles gathered at section S7. The dark blue and cyan lines correspond to the selected inshore water types: AASW (cast 47) and modified WDW (cast 50). The black line – shaded area corresponds to the offshore water types at that location (WW and WDW), determined here as the average of historical profiles in the Powell Basin. The arrows indicate isopycnal mixing processes, and the θS "points" mentioned in the text are zoomed and encircled. The black triangle is the same as in Fig. 6.2. The solid and dashed lines indicate isopycnals.*

Section S7 shows no evidence of bottom cascading, not seen anywhere else in the sampled region. Instead, the bottom boundary layer is governed by vertical turbulence and cross-slope lateral mixing. The first could be due to the vertical shear of the horizontal jet flowing along-slope, while diapycnal mixing across the front would be due to the cross-slope lateral contact between bottom boundary layers with different properties. There is a linear relationship between the bottom neutral density value and the maximum depth over the slope ($R^2 = 0.93$ for the whole set of ESASSI-08 profiles obtained in the Powell basin). That is, the cross-slope distribution/diffusion of temperature and salinity at the bottom levels would result in a neutral density distribution that gradually increases with depth, ranging from 28.06 kg m^{-3} (100% of AASW$_{shelf\ bottom}$) at 700m (cast 47) to 28.31 kg m^{-3} (100% WSDW$_{bottom\ slope}$) at 2200m (cast 51).

After the determination of the water mass fractions contributing to the water mixture observed at the ASF, the two-point isopycnal mixing recipe can be applied away from the bottom boundary layer. The obtained contributing fractions related to the inshore ($AASW_{ASC}$/$MWDW_{ASC}$) and offshore (WW_{PB}/WDW_{PB}) water masses are as follows (see Appendix, Table 6.2). The core of WW reaching the northern Powell Basin and sampled by casts 50-53 (section S7, Fig. 6.1) is already well mixed with $AASW_{ASC}$ carried by the ASC and sampled by casts 47-48: the two fractions are about 50% from 1700 to 2800m isobaths (neutral density between 27.94 and 27.95 in Table 6.2). Below, at 28.00 kg m^{-3}, the offshore profiles (52-53) remain mostly unmixed (80-100% of WW_{PB}), whereas in the middle slope the casts (50-51) show water with properties closer to that carried by the ASC (80-70 % of $AASW_{ASC}$).

At deeper levels (below 28.10 kg m^{-3}) the mixture is between $MWDW_{ASC}$ and WDW. The core of WDW presents several inshore/offshore contributions depending on the proximity to the slope, e.g. from 70% to 10% of $MWDW_{ASC}$ at 28.19 kg m^{-3} for casts 51 and 53, respectively. Above that level, at 28.16 kg m^{-3}, the proportion of $MWDW_{ASC}$ is higher (90% at cast 51, 60% at cast 53).

In summary, section S7 allows the identification of the two main processes involved around the ASF well downstream of the ice-shelf regions and before interacting with the topography of the SSR. AASW flowing along the shelf break ($AASW_{ASC}$) occupies the upper slope (700-1000m). Offshore (1700-2800m), this $AASW_{ASC}$ is 50% mixed with seaward water. It is along the 1700m isobath than the coldest, freshest MWDW is formed below the shelf break (800m) due to diapycnal mixing processes taking place at the bottom boundary layer down the slope. Offshore (2200-2800m), isopycnal mixing processes show several degrees of mixing between this MWDW and seaward WDW.

6.4. Mixing at the gaps of the southern flank of the South Scotia Ridge

In chapter 5 it has been shown that when the ASC crosses the gaps of the southern flank of the SSR, the well-defined frontal structure observed upstream in section S7 is smoothed,

likely due to the rough topography of the SSR and to the strong tidal currents observed in the narrow gaps. The θS diagram of the profiles collected on the western slope of the 51ºW gap (see Fig. 6.1 for location) suggests that the main process taking place at subsurface and deep layers is isopycnal mixing between inshore $AASW_{ASC}$/$MWDW_{ASC}$ and offshore, less modified WW_{PB}/WDW_{PB} (see the black arrows in Fig. 6.4). The bottom layers over the upper slope are not as thick and well-mixed as in section S7 (compare the zoom over casts 47 and 58 in Fig. 6.4a) and the profiles lie out of the triangle representing the three-point diapycnal mixing recipe (see Fig. 6.4a). Moreover, the bottom layers of some casts located over 600m depth show a grading in their properties along isopycnal (see the grey profiles of Fig. 6.4a).

The casts located over the continental shelf (500-600m, casts 58-60) show the same $AASW_{ASC}$ than that observed upstream at cast 47 (section S7). Offshore casts show mixtures of AASW with seaward WW, with fractions of 70-60% of $AASW_{ASC}$ at cast 61 (1000m) and 30-20% at cast 62 (1400m) over the 27.95-27.96 kg m^{-3} isopycnals (see Appendix, Table 6.3).

At deeper levels, below the WW layer, a core of offshore, less modified WDW is observed inwards overlaying the slope (80% of WDW_{PB} at 1400m, cast 62). At the 28.16 kg m^{-3} isopycnal, a profile located at the upper slope (1000m, cast 61) shows a similar water mass fraction (60% of $MWDW_{ASC}$ and 40% of WDW_{PB}) than that observed seawards upstream (2800m, cast 53). This degree of modification of WDW above/around that level seems to be usual in this area as it is also revealed by previous profiles running over the same area (600m, casts 54-57, Fig. 6.4a) and a yo-yo station carried out one week later (600m, casts 106-111, Fig. 6.4b). The set of profile measurements taken at the yo-yo station in less than 12 hours shows the along isopycnal change in water mass fractions as the WDW layer is pumped back and forth over the continental shelf due to the strong tidal currents observed in this region (see Figs. 2.7 and 2.8). Tides would therefore be one of the mechanisms contributing to mixing at the shelf break levels. At the 28.16 kg m^{-3} isopycnal the obtained fractions of WDW range from a maximum of 60% (cast 109) to a minimum of 30% (cast 106) during the 12h period covered by the measurements (see Appendix, Table 6.4).
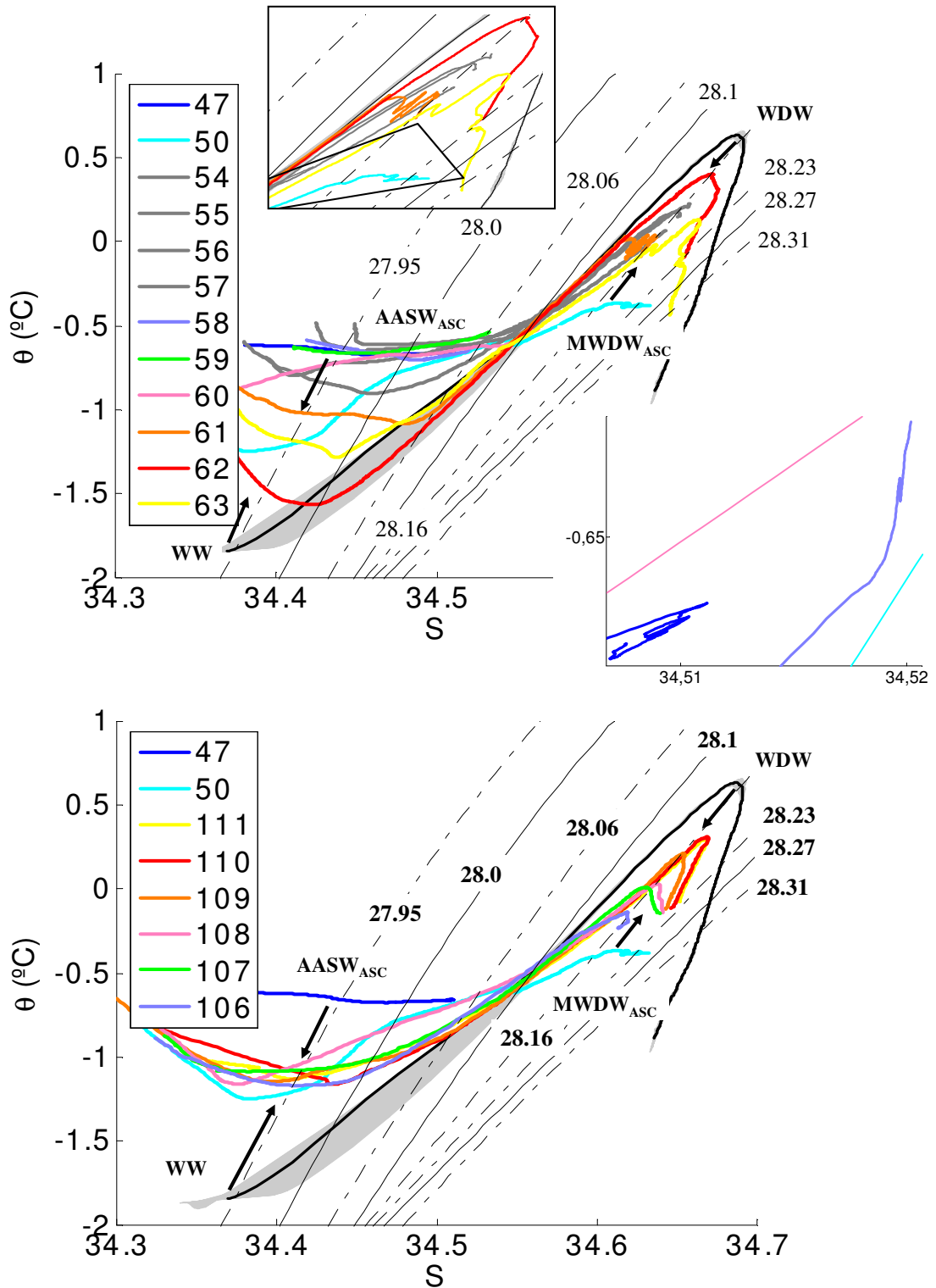
Figure 6.4. *Potential temperature vs. salinity diagram with the ESASSI profiles gathered on the western slope of section S8. Casts 54-57 (600m) shown in the upper panel are indicated by blue squares in Fig. 6.1 and casts 106-111 shown in the lower panel belong to the yo-yo station (600m, cyan diamond). Both panels show also casts 47 and 50, which belong to section S7 and represent the inshore water types. The black line – shaded area corresponds to the offshore water types (WW and WDW), determined here as the average of historical profiles in the Powell Basin. The arrows schematize isopycnal mixing. The solid and dashed lines indicate isopycnals.*

In the previous chapter (see e.g. Fig. 5.10) it has been shown that when the ASC enters the 51ºW gap (see Fig. 6.1) it splits into two branches. The shallower branch follows the 700m isobath and crosses the gap flowing northwards along the western slope. The offshore, deeper branch recirculates within the gap and exits flowing then eastwards still along the southern flank of the SSR; when it reaches the tip located at 50ºW it turns northwards. At the eastern slope of the 51ºW gap, AASW is 100% $AASW_{ASC}$ over the 2000-1500m isobaths (casts 64-65, Fig. 6.5 and Table 6.5). At the WDW layer (density higher than 28.10 kg m^{-3}) the contributing fraction of $MWDW_{ASC}$ respect to WDW_{PB} is higher at upper levels and decreases downwards: it is of 90-70% at 28.16 kg m^{-3}, 80-60% at 28.19-28.20 kg m^{-3} and 50% below the 28.23 kg m^{-3} isopycnal (see Appendix, Table 6.5).

The flow observed on the eastern slope of the 51ºW gap is observed again at the 50ºW cross-slope section (section S9, Fig. 6.1). A profile located over the 1600m isobath shows the highest fraction (90%) of $MWDW_{ASC}$ to the east of section S9 (cast 73, Fig. 6.5 and Table 6.5). These fractions are very localized over that isobath and are not seen upstream, neither over the 2000m nor over the 1500m isobaths (casts 64-65, section S8, Fig. 6.5). This core occupying a thinner layer (from 1400 to about 1600m, cast 73) than at section S7 (from 800 to 1700m, cast 50). In spite of their location within the triangle depicted in the θS diagram, we disregarded diapycnal mixing to be determinant in this case. We tested the application of the three-point mixing recipe and results were as follows (not shown in Tables): 20% of $AASW_{shelf\ bottom}$, 80% of $WDW_{shelf\ break}$, and 0% of $WSDW_{bottom\ slope}$ at 1400m and 1500m; and 10% of $AASW_{shelf\ bottom}$, 50% of $WDW_{shelf\ break}$, and 40% of $WSDW_{bottom\ slope}$ at 1600m. Note that the proportion of WDW is higher than any of the other components.

Next to this cast, an offshore profile (cast 74, over 2200m depth) shows the same eroded core than the upstream casts 64 and 65 (i.e. 80-70% of $MWDW_{ASC}$ at 28.19-28.20 kg m^{-3}, 60% below, see Appendix, Table 6.5). The outermost profile of this section (cast 75, 2500m) shows a much less eroded core of WDW than inwards (90-80% of WDW_{PB} below the 28.16 kg m^{-3} isopcynal). A profile located slightly northwards (cast 76, 2100m, see Fig. 6.1) shows the less modified water masses among the whole set of ESASSI-08 profiles gathered in the Powell basin: the WW_{PB}/WDW_{PB} content is of 80% at 27.95 and 28.16

kg m^{-3} isopycnals (see Appendix, Table 6.5). The most significative feature is that whereas the upper levels are already mixed with inshore water masses, the lower levels are not yet modified at this location (i.e. 100% of WDW$_{PB}$ below 28.19 kg m^{-3}, see Table 6.5 in the Appendix).

In summary, isopycnal mixing taking place at the southern flank of the ridge results in two kinds of water mass mixtures flowing into the Hesperides Trough: an inshore, more modified flow related to the upper and deeper branches of the ASC, and an offshore, less modified flow.
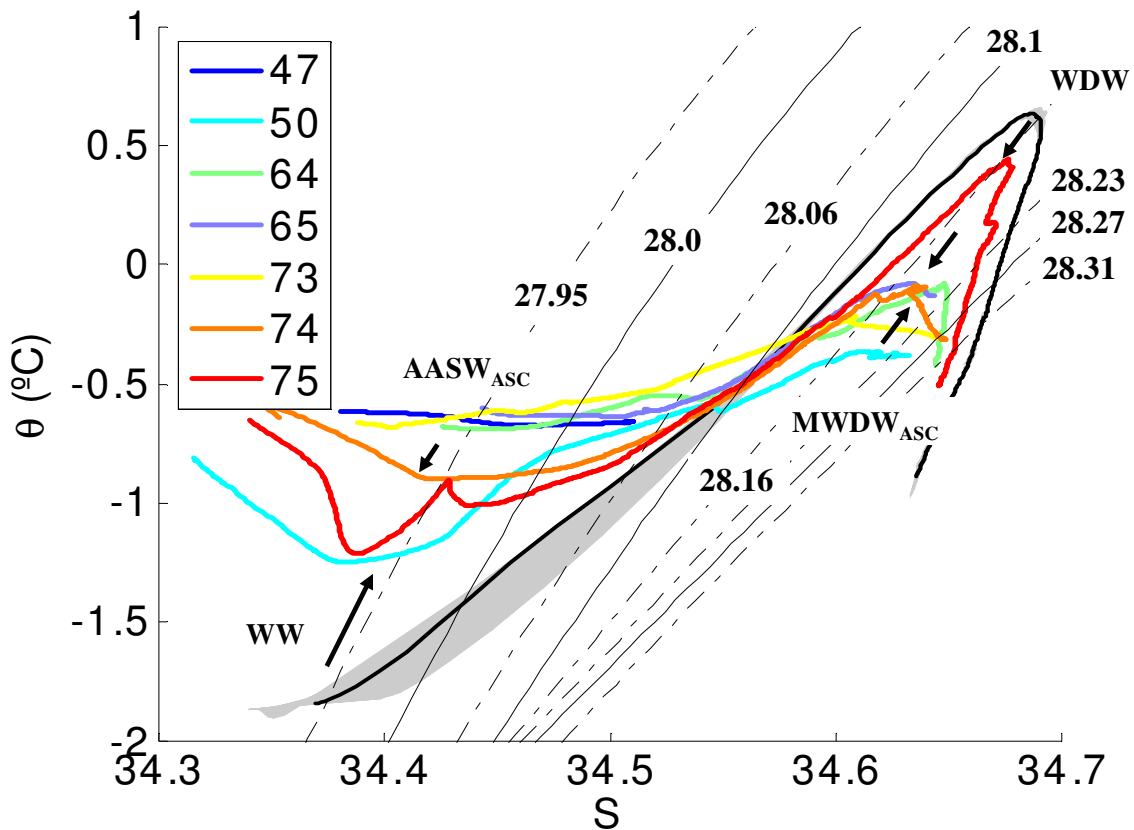
Figure 6.5*. Potential temperature vs. salinity diagram with some of the ESASSI profiles gathered on the eastern slope of section S8 and at section S9. Casts 47 and 50 from section S7, which represent the selected inshore water types, are also shown. The black line – shaded area corresponds to the offshore water types (WW and WDW), determined here as the average of historical profiles in the Powell Basin. The arrows indicate isopycnal mixing. The solid and dashed lines indicate isopycnals.*

6.5. Mixing in the Hesperides Trough. Outflowing mixtures through the Hesperides Passage

In the Hesperides Trough region, the more modified branches of WDW include the flow that crossed the 51ºW gap flowing along the 1000-1300m isobaths (Palmer et al., 2012) and the flow that crossed the 50ºW tip along deeper isobaths. The profiles representative of the upper branch are casts 113, 90 and 91 (see their location in Fig. 6.1 and their θS signature in Fig. 6.6a), which have an $AASW_{ASC}$ mixing fraction of 90-100% at 27.95 kg m^{-3} and a $MWDW_{ASC}$ mixing fraction of 80-90% at 28.16 kg m^{-3}, 70% at 28.19-28.20 kg m^{-3}, and 60-70% at 28.23 kg m^{-3} (Appendix, Table 6.6). The profile representative of the deeper branch is cast 74 (see Fig. 6.5 and Appendix, Table 6.5). This more modified flow mixes isopycnally with the offshore, less modified flow while travelling clockwise around the trough. The less modified WDW core filling the center of the trough (at 50ºW, cast 78, over a 4200m depth) is therefore a mixture of both kind of flows (Fig. 6.6a). The fractions obtained from the OMP analysis show that the fractions of $MWDW_{ASC}$ reduce to 50% at 28.16 kg m^{-3}, 30-20% at 28.19-28.20 kg m^{-3}, and 10% below, in benefit of higher fractions of WDW_{PB}.

The more modified WDW branch is observed flowing over the 1000m isobath at section S5 (casts 90, 91, and 92) and also in between casts 94-95 from the Hesperides Passage (Figs. 6.6a,b). The outflow into the Scotia Sea through the gap sampled by section S5 (see Fig. 4.9) is a minor fraction of the total outflow, which takes place mainly through the deepest gap of the northern flank: the Hesperides Passage (3100m), located at 48ºW.

In Section S10 (Hesperides Passage; see Fig. 6.6b and Appendix, Table 6.7) the subsurface layer shows a higher content of $AASW_{ASC}$ close to the upper slope (80%) than in the middle of the gap (60-50%). The deepest, offshore casts (casts 96-97, over 1900-3100m) present similar $MWDW_{ASC}$ vs. WDW mixtures to those observed in the middle of the Hesperides trough (cast 78; Appendix, Table 6.6), that is a WDW_{PB} content of 60% at 28.16 kg m^{-3}, 70-80% at 28.19-28.20 kg m^{-3}, and 90% at 28.23 kg m^{-3}. The inshore profiles are more modified by $MWDW_{ASC}$: 60% at 28.16 kg m^{-3}, 40% at 28.23 kg m^{-3} for cast 95, over 1600m depth (Appendix, Table 6.7).
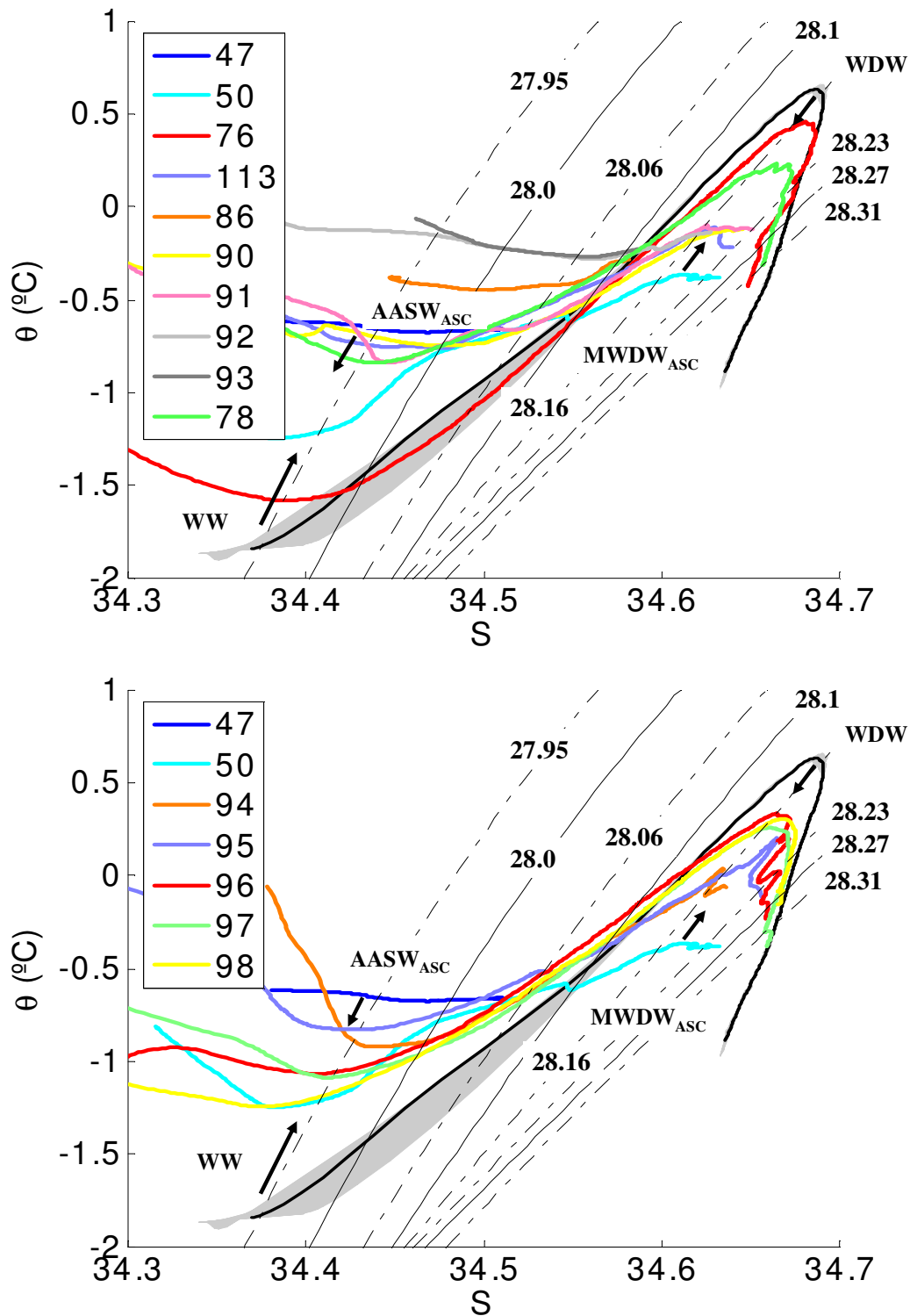
Figure 6.6. Potential temperature vs. salinity diagrams with profiles from the Hesperides Trough (casts 113, 76, and 78) and from the northern wall of the South Scotia Ridge (casts 86, 90, 91, 92, and 93, section S5) in the upper panel, and with profiles from the Hesperides Passage (casts 94-98, section S10) in the lower panel. Both panels show also casts 47 and 50, which belong to section S7 and represent the inshore water types.. The black line – shaded area corresponds to the offshore water types (WW and WDW), determined here as the average of historical profiles in the Powell Basin. The arrows indicate isopycnal mixing. The solid and dashed lines indicate isopycnals.

6.6. Water mass fractions in the Scotia Sea side. Intrusions of WDW from the eastern gaps of the SSR

Once in the Scotia Sea, the θS properties observed at a cross-slope section located just to the west of the Hesperides Passage (section S6, see Fig. 6.1) show that WDW from the Hesperides Trough extends seawards to at least over the 2900m isobath, since the outermost cast of this section (cast 85, Fig. 6.7a) has similar contributing fractions than the deeper profiles of the Hesperides Passage (e.g., 50% of WDW_{PB} at 28.16 kg m^{-3}, 80-70% at 28.19-28.20 kg m^{-3}, and 80% at 28.23 kg m^{-3}; see Appendix, Table 6.8). The more modified WDW branch observed crossing section S5 also extends seawards to at least the 2200m isobath (cast 84, section S6). The $MWDW_{ASC}$ fractions at cast 84 are of 70% at upper levels (i.e. 28.16, 28.19, and 28.20 kg m^{-3}) and of 50% at 28.23 kg m^{-3} (Appendix, Table 6.8).

Intrusions of WDW different from that seen in the Hesperides Passage are observed further west, at 52ºW (section S5N, Fig. 6.1). Some fragments of the outermost profiles of this section (Fig. 6.7a) show water that is warmer and saltier than that observed at the deeper, less modified profile of the Hesperides Passage (cast 97). Moreover, their properties overlap the mean profile of the Powell Basin, which altogether suggest that this water comes from less modified branches crossing the SSR through the eastern gaps (e.g. from Orkney Passage; Naveira-Garabato, 2002a). The outermost profile of this section S5N (3300m, cast 44) shows eastern WDW extending from 1100m to 1600m (100% of WDW_{PB} at 28.17-28.21 kg m^{-3}, see Table 6.8). Inshore, a profile located over the 3000m isobath (cast 43) shows this intrusion not extending as deep as offshore (from 1100 to 1200m), and over the 2400m isobath (cast 42) this intrusion is even shallower (from 1000 to 1100m). Below the levels occupied by eastern WDW, cast 42 shows water from the Hesperides Trough: 40% of $MWDW_{ASC}$ and 60% of WDW_{PB} at 28.19,28.20 and 28.23 kg m^{-3}, see Table 6.8). Over the 1600m isobath, a nearby profile (cast 41, section S5N) shows such an intrusion just at 1000m (28.16 kg m^{-3}). Except at this level, profile 41 has the same water mass fractions than those observed upstream over the 2200m isobath (cast 84, section S6). Such an intrusion extends westwards: the θS properties seen at cast 44 are also observed at 53ºW inshore than upstream (cast 18, over a 3000m depth, see Figs. 1 and 7a; Appendix, Table 6.8).
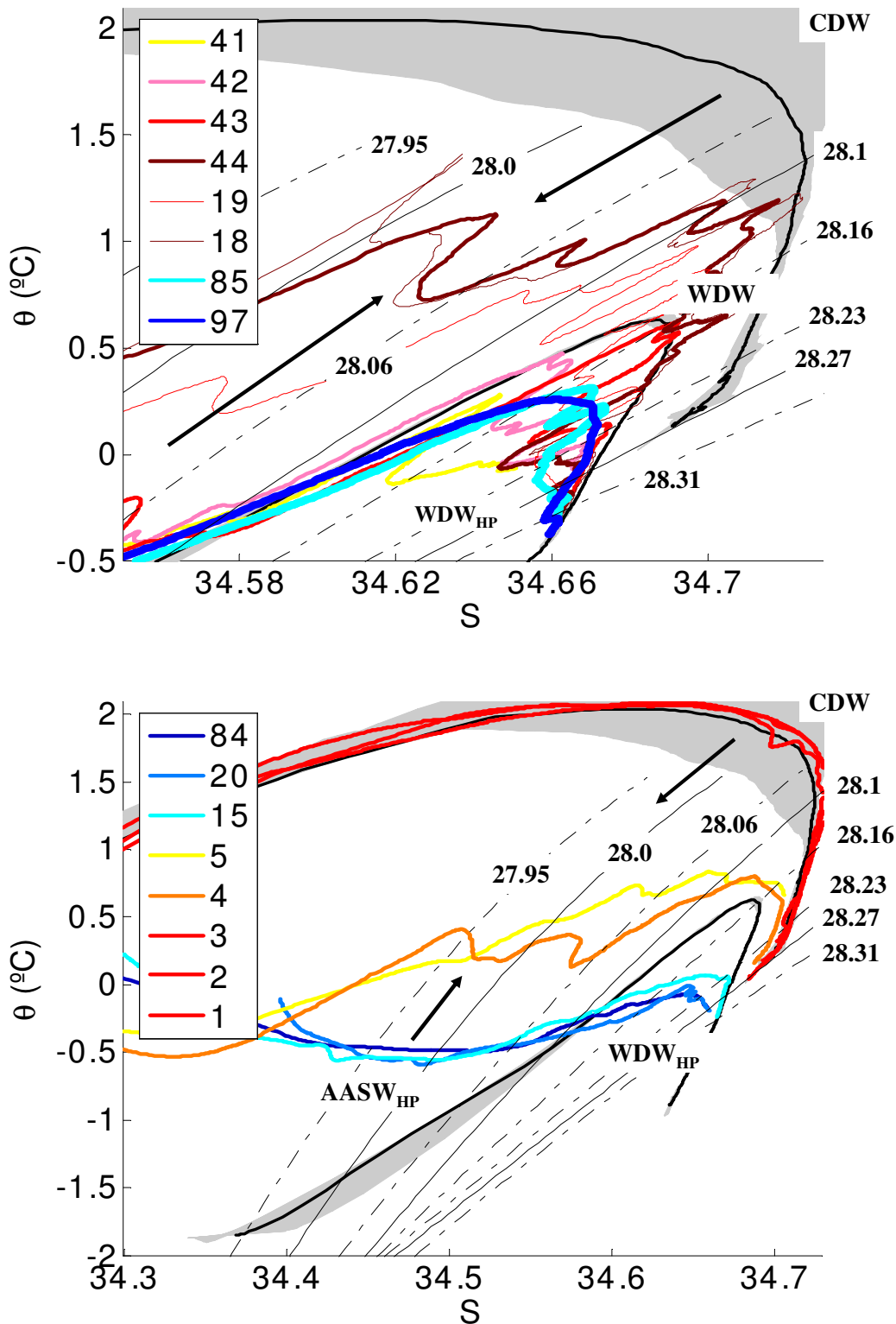
Figure 6.7*. Potential temperature vs. salinity diagrams with ESASSI profiles gathered in the Scotia Sea (sections S6, S5N, S3, S2, and S1, see Fig. 6.1) and the deepest profile of the Hesperides Passage (cast 97, section S10). The black line – shaded area correspond to the offshore water types (WW/WDW and CDW, determined here as the average of historical profiles in the Powell Basin and southern Drake Passage, respectively). The arrows indicate isopycnal mixture. The solid and dashed lines indicate isopycnals.*

The WDW that flows westwards and reaches the cross-slope section at 55ºW (section S2, Fig. 6.1) has a Hesperides Trough origin, with no evidence of intrusions of WDW from the eastern gaps of the SSR (see e.g. cast 15 in section S2, over 2900m; Fig. 6.7b). The AASW is also water overflowing the western sector of the SSR, although it becomes warmer after crossing the gaps of the northern flank (see the shallower layers of casts 86 and 93 from section S5, Fig. 6.6a). The outermost profile of section S2 (cast 15, over 2900m) lies approximately in between those profiles observed at the cross-slope section immediately out from the Hesperides Passage (casts 84-85, section S6). Its $MWDW_{ASC}$ fractions are of about 60% at 29.16 kg m^{-3}, 50-40% below, and about 20% at 28.23 kg m^{-3}, for instance. At 28.26-28.27 kg m^{-3} a higher proportion of WDW_{PB} than that obtained for the outflow through the Hesperides Passage suggests that these lower levels of WDW would come from the eastern gaps. We take this profile (cast 15, section S2) as a reference ($AASW_{HP}$/WDW_{HP}, see Appendix, Table 6.8) to estimate the contributing fractions of CDW from the Drake Passage at the Southern Boundary of the ACC.

6.7. Mixing at the southern boundary of the Antarctic Circumpolar Current

The northwestermost section of the cruise (section S1) is a cross-slope section located southwest of the Shackleton Fracture Zone (at 56ºW, see Fig. 6.1), in Drake Passage. This is the only set of measurements gathered outside the Scotia Sea and Weddell Sea regions during the cruise. Its outermost stations (casts 1-3, over 3900-2100m depth) extend 60km from the continental shelf and show 100% CDW from the ACC sector west of the Drake Passage (see Fig. 6.7b). The southern profiles of section S1 (casts 4-5, over 1700-1100m depth) present several degrees of mixing between CDW from the ACC and the inshore AASW/WDW outflowing from the Hesperides Trough, except at 28.26 kg m^{-3} that WDW would come from the eastern gaps (see that cast 15 has a water mass fraction of WDW_{PB} higher than the outflow through the Hesperides Passage at this level; see Appendix, Tables 6.7 and 6.8). Their contributing fractions are: about 30-40% of CDW at 27.95-28.00 kg m^{-3}, 50-70% at 28.10 kg m^{-3}, 80% at 28.16 kg m^{-3}, and 90% below (Appendix, Table 6.9). That is, the WDW layer is suffering more modification from the ACC than the upper levels south of the Shackleton Fracture Zone.

The Southern Boundary of the ACC within the Scotia Sea is represented by the outermost casts of section S3 (casts 18, over 3000m depth) and section S5N (cast 44, over 3300m depth, see Figs. 1 and 7a), both located 30 km away from the shelf break. Conversely, the outermost profile of section S6 is only 15 km away from the shelf break (see Fig. 6.1) and has no sign of CDW from the ACC. Mixtures of CDW with AASW/WDW are found from the surface down to the 28.16 kg m^{-3} isopycnal (see Appendix, Table 6.9). No contribution from the ACC is found at lower levels, which are occupied by WDW coming from the eastern gaps of the SSR.

Summarizing, south of the Shackleton Fracture Zone, CDW mixes with AASW/WDW from the western sector of the SSR except at 28.26 kg m^{-3}, where WDW would come from the gaps located to the East of the South Orkney Plateau. Further east, at 53-52ºW and seaward than 3000m, the AASW/WDW branch from the Hesperides Trough mixes with CDW for waters lighter than 28.16 kg m^{-3}. Nevertheless, WDW from the eastern gaps of the SSR intrudes between 28.17-28.21 kg m^{-3}.

6.8. Conclusions

At the continental margin of the Weddell Sea, water carried by the Weddell Gyre gets in contact with continental shelf waters suffering a progressive ventilation along its pathway. The deepest fraction of this ventilated water flows along the southern flank of the SSR beyond the South Orkney Plateau and escapes through the deep gaps to the East of the Orkney Islands. Surface and intermediate water however can shorten the way and outflow into the Scotia Sea through the gaps to the west of the Orkney Islands, where they suffer further modifications. In this chapter we have described the mixing processes occurring from just before the ASF reaches the southern flank of the SSR to the contact with ACC waters once in the Scotia Sea.

Before the ASC crosses the southern flank of the SSR, the collected profiles show thick mixed layers over the upper slope. The downslope stratification is however stable, as the absence of SW over the continental shelves prevents downslope plumes/cascading at the

time of the cruise. Conversely, lateral, cross-slope mixing takes place at the bottom boundary layer between three different water masses: AASW carried by the ASC, WDW occupying the open-sea shelf break levels, and WSDW flowing over the lower slope. Such process explains the formation of the colder, relatively fresher component of MWDW, and differs from the mixing processes observed further upstream (i.e., next to Weddell Sea ice shelves) which imply the presence of SW. Away from the bottom boundary layer, mixing processes are mainly along isopycnals at the subsurface and intermediate levels. This kind of mixing becomes clear when observing the modification of offshore WW and WDW cores: the offshore relative temperature minimum of WW is modified by the water carried by the ASC over the shelf break, whereas at deeper layers the relative temperature maximum of WDW is eroded by the MWDW formed at the offshore side of the ASF.

A crucial step of the Weddell Sea water overflowing the western sector of the SSR is its transit around the Hesperides Trough. During its clockwise circulation around the trough, we distinguish two branches. First, the coldest WDW flowing over depths shallower than 1300m, which does not show any further significant change after crossing the ridge. This is straightforward when comparing the profiles located at the 51ºW gap (section S5) and the cross-slope section located just outside in the Scotia Sea (section S6) with the 1000m isobath profile located at the southwestern side of the trough (see Fig. 6.1 for locations and Fig. 6.7a for the comparison of the profiles). Second, the flow that goes over deeper isobaths inside the trough, which shows several mixtures between the coldest, inshore WDW component and the offshore, less modified WDW. When this water flows into the Scotia Sea after its 400-500km pathway around the Hesperides Trough, its fraction of $MWDW_{ASC}$ has increased from 20% to 40% at the upper levels of the WDW layer. The profiles located in the middle of the Hesperides Passage (the major gate to the Scotia Sea) show a contribution of about 20% of $MWDW_{ASC}$ at intermediate levels and of about 10% at lower levels in the WDW layer.

Once in the Scotia Sea, a cross-slope section extending from the shelf break to the 2900m isobath shows WDW from the Hesperides Passage. Sections extending to deeper isobaths (> 3000m) also show less modified WDW coming from the eastern gaps of the SSR and several mixtures with CDW from the ACC at the outermost stations sampling the Southern Boundary of the ACC.

Altogether, our results show the contribution of water lighter than 28.16 kg m^{-3} crossing the western sector of the SSR (AASW/WDW) to the ventilation of the upper levels of the ACC (UCDW/LCDW) in the southwestern side of the Scotia Sea. Moreover, eastern than 55ºW, the lower levels of the LCDW layer are occupied by WDW from the western and eastern sectors of the SSR offshore to depths of at least 3000m at the time of the cruise.

6.9. APPENDIX: Source water mass proportions

Table 6.1. *Diapycnal mixing at the bottom boundaries of the ASF as observed in the Weddell Sea cross-slope section (S7), just before reaching the southern gaps of the SSR (see Fig. 6.1). The values are the fraction of the three water types contributing to different levels of the observed profiles.*

	Cast 47 (700m)		
Depth (m)	**AASW$_{shelf\ bottom}$ (%)**	**WDW$_{shelf\ break}$ (%)**	**WSDW$_{bottom\ slope}$ (%)**
300-700	100	0	0
	Cast 48 (1000m)		
Depth (m)	**AASW$_{shelf\ bottom}$ (%)**	**WDW$_{shelf\ break}$ (%)**	**WSDW$_{bottom\ slope}$ (%)**
400-1000	80	0	20
	Cast 50 (1700m)		
Depth (m)	**AASW$_{shelf\ bottom}$ (%)**	**WDW$_{shelf\ break}$ (%)**	**WSDW$_{bottom\ slope}$ (%)**
800	30	20	50
900	30	20	50
1000	20	30	50
1200	20	20	60
1300	20	20	60
1400	20	20	60
1500	20	10	70
1600	10	10	80
1700	10	10	80
	Cast 51 (2200m)		
Depth (m)	**AASW$_{shelf\ bottom}$ (%)**	**WDW$_{shelf\ break}$ (%)**	**WSDW$_{bottom\ slope}$ (%)**
1600-2200	0	0	100

Table 6.2. *Isopycnal mixtures at the Weddell Sea cross-slope section (S7), located just before the ASF/ASC reach the southern gaps of the SSR (see Fig. 6.1). The values are the fraction of the two water types contributing to different layers of the observed profiles.*

γ^n (kg m^{-3})	Cast 47 (700m)		Cast 48 (1000m)		Cast 50 (1700m)		Cast 51 (2200m)		Cast 52 (2600m)		Cast 53 (2800m)	
	AASW$_{ASC}$ (%)	WW$_{PB}$ (%)	AASW$_{ASC}$ (%)	WW$_{PB}$ (%)	AASW$_{ASC}$ (%)	WW$_{PB}$ (%)	AASW$_{ASC}$ (%)	WW$_{PB}$ (%)	AASW$_{ASC}$ (%)	WW$_{PB}$ (%)	AASW$_{ASC}$ (%)	WW$_{PB}$ (%)
27.94	100	0	100	0	50	50	50	50	50	50	50	50
27.95	100	0	100	0	50	50	50	50	50	50	50	50
27.96	100	0	100	0	50	50	50	50	40	60	40	60
27.98	100	0	100	0	60	40	60	40	40	60	30	70
27.99	100	0	100	0	70	30	60	40	30	70	10	90
28.00	100	0	100	0	80	20	70	30	20	80	0	100
γ^n (kg m^{-3})	MWDW$_{ASC}$ (%)	WDW$_{PB}$ (%)	MWDW$_{ASC}$ (%)	WDW$_{PB}$ (%)	MWDW$_{ASC}$ (%)	WDW$_{PB}$ (%)	MWDW$_{ASC}$ (%)	WDW$_{PB}$ (%)	MWDW$_{ASC}$ (%)	WDW$_{PB}$ (%)	MWDW$_{ASC}$ (%)	WDW$_{PB}$ (%)
28.10					100	0	100	0	100	0	100	0
28.11					100	0	100	0	100	0	90	10
28.12					100	0	90	10	100	0	90	10
28.13					100	0	90	10	100	0	80	20
28.14					100	0	100	0	90	10	60	40
28.15					100	0	100	0	90	10	50	50
28.16					100	0	90	10	90	10	60	40
28.17					100	0	90	10	100	0	70	30
28.18					100	0	80	20	90	10	50	50

28.19					100	0	70	30	80	20	10	90
28.20					100	0	60	40	80	20	10	90
28.21					100	0	70	30	80	20	10	90
28.22					100	0	60	40	70	30	20	80
28.23					100	0	70	30	40	60	30	70
28.24					100	0	70	30	30	70	30	70
28.25					100	0	70	30	20	80	30	70
28.26					100	0	70	30	10	90	40	60
28.27					100	0	70	30	20	80	40	60

Table 6.3. *Isopycnal mixtures at the western slope of the 51ºW gap indenting the southern flank of the SSR (S8, see Fig. 6.1). The values are the fraction of the two water types contributing to different layers of the observed profiles.*

	Cast 58 (500m)		Cast 59 (600m)		Cast 60 (600m)		Cast 61 (1000m)		Cast 62 (1400m)		Cast 63 (2100m)	
γ^n (kg m^{-3})	AASW$_{ASC}$ (%)	WW$_{PB}$ (%)	AASW$_{ASC}$ (%)	WW$_{PB}$ (%)	AASW$_{ASC}$ (%)	WW$_{PB}$ (%)	AASW$_{ASC}$ (%)	WW$_{PB}$ (%)	AASW$_{ASC}$ (%)	WW$_{PB}$ (%)	AASW$_{ASC}$ (%)	WW$_{PB}$ (%)
27.94	100	0	100	0	90	10	70	30	30	70	50	50
27.95	100	0	100	0	90	10	70	30	30	70	50	50
27.96	100	0	100	0	100	0	60	40	20	80	50	50
27.98	100	0	100	0	100	0	60	40	10	90	40	60
27.99	100	0	100	0	100	0	60	40	0	100	30	70
28.00	100	0	100	0	100	0	50	50	0	100	20	80
γ^n (kg m^{-3})	MWDW$_{ASC}$ (%)	WDW$_{PB}$ (%)	MWDW$_{ASC}$ (%)	WDW$_{PB}$ (%)	MWDW$_{ASC}$ (%)	WDW$_{PB}$ (%)	MWDW$_{ASC}$ (%)	WDW$_{PB}$ (%)	MWDW$_{ASC}$ (%)	WDW$_{PB}$ (%)	MWDW$_{ASC}$ (%)	WDW$_{PB}$ (%)
28.10					100	0	30	70	60	40	100	0
28.11					90	10	20	80	40	60	90	10
28.12					90	10	20	80	40	60	80	20
28.13							30	70	30	70	80	20
28.14							50	50	40	60	80	20
28.15							60	40	30	70	80	20
28.16							60	40	20	80	80	20
28.17							60	40	20	80	70	30
28.18							60	40	20	80	60	40

28.19								20	80	60	40
28.20								20	80	40	60
28.21								20	80	30	70
28.22								30	70	40	60
28.23								30	70	40	60
28.24								30	70	40	60
28.25								40	60	40	60
28.26										40	60
28.27										40	60

Table 6.4. *Isopycnal mixtures at the yo-yo station (see Fig. 6.1 for location).*

γ^n (kg m^{-3})	Cast 106 (600m)		Cast 107 (600m)		Cast 108 (600m)		Cast 109 (600m)		Cast 110 (600m)		Cast 111 (600m)	
	MWDW$_{ASC}$ (%)	WDW$_{PB}$ (%)	MWDW$_{ASC}$ (%)	WDW$_{PB}$ (%)	MWDW$_{ASC}$ (%)	WDW$_{PB}$ (%)	MWDW$_{ASC}$ (%)	WDW$_{PB}$ (%)	MWDW$_{ASC}$ (%)	WDW$_{PB}$ (%)	MWDW$_{ASC}$ (%)	WDW$_{PB}$ (%)
28.10	30	70	50	50	40	60	70	30	70	30	80	20
28.11	30	70	40	60	50	50	60	40	60	40	70	30
28.12	50	50	50	50	60	40	60	40	60	40	70	30
28.13	60	40	50	50	60	40	60	40	60	40	70	30
28.14	60	40	50	50	60	40	60	40	70	30	70	30
28.15	70	30	50	50	60	40	50	50	60	40	60	40
28.16	70	30	60	40	50	50	40	60	50	50	50	50
28.17	80	20	60	40	60	40	40	60	30	70	40	60
28.18			60	40	60	40	40	60	30	70	30	70
28.19			60	40	60	40	50	50	30	70	30	70
28.20			70	30	60	40	60	40	40	60	40	60
28.21					60	40	60	40	50	50	50	50
28.22									50	50	50	50

Table 6.5. *Isopycnal mixtures at the eastern slope of section S8, at section S9, and at station 76 (see Fig. 6.1 for location).*

	Cast 64 (2000m)		Cast 65 (1500m)		Cast 73 (1600m)		Cast 74 (2200m)		Cast 75 (2500m)		Cast 76 (2100m)	
γ^n (kg m^{-3})	$AASW_{ASC}$ (%)	WW_{PB} (%)	$AASW_{ASC}$ (%)	WW_{PB} (%)	$AASW_{ASC}$ (%)	WW_{PB} (%)	$AASW_{ASC}$ (%)	WW_{PB} (%)	$AASW_{ASC}$ (%)	WW_{PB} (%)	$AASW_{ASC}$ (%)	WW_{PB} (%)
27.94	100	0	100	0	100	0	80	20	60	40	20	80
27.95	100	0	100	0			80	20	60	40	20	80
27.96	100	0	100	0			80	20	70	30	20	80
27.98	100	0	100	0			80	20	60	40	10	90
27.99	100	0	100	0			70	30	60	40	0	100
28.00							70	30	60	40	0	100
γ^n (kg m^{-3})	$MWDW_{ASC}$ (%)	WDW_{PB} (%)	$MWDW_{ASC}$ (%)	WDW_{PB} (%)	$MWDW_{ASC}$ (%)	WDW_{PB} (%)	$MWDW_{ASC}$ (%)	WDW_{PB} (%)	$MWDW_{ASC}$ (%)	WDW_{PB} (%)	$MWDW_{ASC}$ (%)	WDW_{PB} (%)
28.10	70	30	60	40	40	60	100	0	70	30	70	30
28.11	70	30	60	40	50	50	90	10	70	30	50	50
28.12	80	20	70	30	70	30	90	10	70	30	40	60
28.13	80	20	70	30	70	30	80	20	70	30	40	60
28.14	80	20	70	30	80	20	80	20	70	30	40	60
28.15	90	10	70	30	90	10	90	10	70	30	30	70
28.16	90	10	70	30	90	10	80	20	50	50	20	80
28.17	90	10	70	30	90	10	80	20	20	80	20	80
28.18	90	10	70	30	90	10	80	20	10	90	10	90

28.19	80	20	70	30	90	10	80	20	10	90	0	100
28.20	80	20	60	40	90	10	70	30	20	80	0	100
28.21	70	30	60	40	90	10	70	30	20	80	0	100
28.22	60	40	60	40	90	10	60	40	20	80	0	100
28.23	50	50	60	40	90	10	60	40	20	80	0	100
28.24	50	50	50	50	80	20	60	40	20	80	0	100
28.25	40	60	50	50	80	20	60	40	10	90	0	100
28.26	50	50			80	20	60	40	20	80	10	90
28.27	50	50			70	30	60	40	30	70	20	80

Table 6.6. Isopycnal mixtures in the Hesperides Trough (see Fig. 6.1 for the location of the profiles).

γ^n (kg m^{-3})	Cast 113 (1000m)		Cast 78 (4200m)		Cast 90 (1100m)		Cast 91 (1300m)	
	AASW$_{ASC}$ (%)	WW$_{PB}$ (%)	AASW$_{ASC}$ (%)	WW$_{PB}$ (%)	AASW$_{ASC}$ (%)	WW$_{PB}$ (%)	AASW$_{ASC}$ (%)	WW$_{PB}$ (%)
27.94	90	10	80	20	100	0	100	0
27.95	90	10	80	20	100	0	90	10
27.96	90	10	80	20	90	10	90	20
27.98	90	10	80	20	90	10	80	20
27.99	80	20	80	20	90	10	80	20
28.00	80	20	80	20	90	10	90	10
γ^n (kg m^{-3})	MWDW$_{ASC}$ (%)	WDW$_{PB}$ (%)	MWDW$_{ASC}$ (%)	WDW$_{PB}$ (%)	MWDW$_{ASC}$ (%)	WDW$_{PB}$ (%)	MWDW$_{ASC}$ (%)	WDW$_{PB}$ (%)
28.10			10	90	80	20	60	40
28.11	70	30	30	70	70	30	60	40
28.12	80	20	40	60	80	20	70	30
28.13	80	20	50	50	80	20	70	30
28.14	90	10	50	50	80	20	70	30
28.15	90	10	50	50	80	20	80	20
28.16	90	20	50	50	80	20	80	20
28.17	80	20	40	60	80	20	70	30
28.18	80	20	40	60	80	20	70	30
28.19	70	30	30	70	70	30	70	30

28.20	70	30	20	80	70	30	70	30
28.21	70	30	20	80	60	40	60	40
28.22	70	30	10	90	60	40	60	40
28.23	70	30	10	90	60	40	60	40
28.24	70	30	10	90	50	50	50	50
28.25	60	40	10	90			40	60
28.26	60	40	10	90				
28.27			20	80				

Table 6.7. *Isopycnal mixtures across the Hesperides Passage (section S10 in Fig. 6.1).*

γ^n (kg m^{-3})	Cast 94 (800m)		Cast 95 (1600m)		Cast 96 (1900m)		Cast 97 (3100m)		Cast 98 (1900m)	
	AASW$_{ASC}$ (%)	WW$_{PB}$ (%)	AASW$_{ASC}$ (%)	WW$_{PB}$ (%)	AASW$_{ASC}$ (%)	WW$_{PB}$ (%)	AASW$_{ASC}$ (%)	WW$_{PB}$ (%)	AASW$_{ASC}$ (%)	WW$_{PB}$ (%)
27.94	80	20	80	20	60	40	60	40	50	50
27.95	80	20	80	20	60	40	60	40	50	50
27.96	80	20	80	20	60	40	60	40	50	50
27.98	70	30	80	20	60	40	60	40	50	50
27.99	70	30	80	20	60	40	60	40	50	50
28.00	70	30	90	10	60	40	60	40	50	50
	MWDW$_{ASC}$	WDW$_{PB}$	MWDW$_{ASC}$	WDW$_{PB}$	MWDW$_{ASC}$	WDW$_{PB}$	MWDW$_{ASC}$	WDW$_{PB}$	MWDW$_{ASC}$	WDW$_{PB}$

	(%)	(%)	(%)	(%)	(%)	(%)	(%)	(%)	(%)	(%)
28.10	10	90	30	70	0	100	0	100	0	100
28.11	30	70	40	60	0	100	10	90	10	90
28.12	50	50	50	50	10	90	30	70	20	80
28.13	60	40	60	40	20	80	40	60	30	70
28.14	70	30	60	40	30	70	40	60	40	60
28.15	70	30	70	30	30	70	40	60	40	60
28.16	60	40	60	40	30	70	40	60	40	60
28.17	60	40	60	40	30	70	30	70	30	70
28.18	70	30	60	40	20	80	30	70	30	70
28.19	60	40	50	50	20	80	30	70	20	80
28.20			30	70	20	80	20	80	20	80
28.21			40	60	20	80	20	80	10	90
28.22			50	50	30	70	10	90	10	90
28.23			40	60	40	60	10	90	10	90
28.24			40	60	20	80	10	90	10	90
28.25			30	70	20	80	10	90	10	90
28.26			30	70	30	70	10	90	10	90
28.27					30	70	10	90	10	90

Table 6.8. *Isopycnal mixtures at the offshore profiles of the Scotia Sea sections (S3, S5N and S6 in Fig. 6.1).*

γ^n (kg m^{-3})	Cast 84 (2200m)		Cast 85 (2900m)		Cast 40 (1200m)		Cast 41 (1600m)		Cast 42 (2400m)		Cast 43 (3000m)		Cast 44 (3300m)		Cast 15 (2900m)	
	MWDW$_{ASC}$ (%)	WDW$_{PB}$ (%)	MWDW$_{ASC}$ (%)	WDW$_{PB}$ (%)	MWDW$_{ASC}$ (%)	WDW$_{PB}$ (%)	MWDW$_{ASC}$ (%)	WDW$_{PB}$ (%)	MWDW$_{ASC}$ (%)	WDW$_{PB}$ (%)	MWDW$_{ASC}$ (%)	WDW$_{PB}$ (%)	MWDW$_{ASC}$ (%)	WDW$_{PB}$ (%)	MWDW$_{ASC}$ (%)	WDW$_{PB}$ (%)
28.10	0	100	50	50											0	100
28.11	30	70	50	50	60	40	50	50	40	60	60	40			10	90
28.12	50	50	60	40	80	20	60	40	50	50	80	20			30	70
28.13	60	40	60	40	80	20	80	20	40	60	90	10			50	50
28.14	70	30	60	40	90	10	80	20	20	80	90	10			50	50
28.15	70	30	60	40	90	10	50	50	20	80	80	20			60	40
28.16	70	30	50	50	90	10	50	50	20	80	60	40			60	40
28.17	80	20	40	60	90	10	60	40	30	70	10	90	0	100	60	40
28.18	70	30	30	70	80	20	70	30	40	60	0	100	0	100	50	50
28.19	70	30	20	80	80	20	70	30	40	60	0	100	0	100	50	50
28.20	70	30	30	70	80	20	70	30	40	60	20	80	0	100	40	60
28.21	60	40	20	80			60	40	30	70	20	80	0	100	40	60
28.22	60	40	10	90			50	50	30	70	30	70	20	80	30	70
28.23	50	50	20	80			50	50	40	60	20	80	40	60	20	80
28.24	40	60	30	70			50	50	40	60	0	100	40	60	20	80
28.25	40	60	30	70					10	90	0	100	20	80	10	90
28.26	30	70	30	70					10	90			20	80	0	100
28.27	30	70	30	70					10	90			10	90	0	100

Table 6.9. *Isopycnal mixtures at the Southern Boundary of the ACC (section S1, and outermost stations of sections S3 and S5N, see Fig. 6.1).*

γ^n (kg m^{-3})	Cast 44 (3300m)		Cast 19 (2600m)		Cast 18 (3000m)		Cast 5 (1100m)		Cast 4 (1700m)	
	AASW$_{HP}$/WDW$_{HP}$ (%)	CDW$_{DP}$ (%)	AASW$_{HP}$/WDW$_{HP}$ (%)	CDW$_{DP}$ (%)	AASW$_{HP}$/WDW$_{HP}$ (%)	CDW$_{DP}$ (%)	AASW$_{HP}$/WDW$_{HP}$ (%)	CDW$_{DP}$ (%)	AASW$_{HP}$/WDW$_{HP}$ (%)	CDW$_{DP}$ (%)
27.94	80	20	90	10	80	20	80	20	70	30
27.95	80	20	90	10	80	20	70	30	70	30
27.96	80	20	80	20	70	30	70	30	70	30
27.97	70	30	80	20	70	30	70	30	70	30
27.98	70	30	80	20	60	40	70	30	70	30
27.99	60	40	80	20	30	70	60	40	70	30
28.00	50	50	70	30	40	60	60	40	70	30
28.01	40	60	70	30	40	60	60	40	70	30
28.02	30	70	70	30	30	70	60	40	70	30
28.03	30	70	60	40	40	60	50	50	60	40
28.04	40	60	60	40	40	60	40	60	60	40
28.05	40	60	70	30	40	60	40	60	60	40
28.06	40	60	60	40	40	60	40	60	60	40
28.07	30	70	60	40	40	60	40	60	70	30
28.08	30	70	40	60	30	70	40	60	70	30
28.09	20	80	40	60	10	90	30	70	70	30
28.10	10	90	30	70	10	90	30	70	50	50

28.11	10	90	30	70	20	80	30	70	40	60
28.12	10	90	20	80	0	100	30	70	40	60
28.13	10	90	40	60	0	100	30	70	30	70
28.14	10	90	20	80	10	90	20	80	20	80
28.15	10	90	20	80	10	90	20	80	20	80
28.16	20	80	30	70	20	80	20	80	20	80
28.17							10	90	10	90
28.18							10	90	10	90
28.19							10	90	10	90
28.20									10	90
28.21									10	90
28.22									10	90
28.23									10	90
28.24									20	80
28.25									20	80
28.26									*20*	*80*

CHAPTER 7

CONCLUSIONS

The objectives of this thesis were (1) to describe the regional circulation of the western sector of the South Scotia Ridge, between the South Shetland and South Orkney Islands, paying particular attention to the path of the Antarctic Slope Current; (2) to quantify the water mass transports over the western sector of the SSR; and (3) to study the modification of Weddell Sea water masses as they cross the SSR and how do they interact with Scotia Sea waters. To do that we have analyzed the hydrographic data collected during a high spatial resolution survey (1-2 nm over the continental slopes and about 5 nm elsewhere) carried out in January 2008: the ESASSI-08 cruise.

The regional pathways and exportation of waters from the Weddell Sea into the Scotia Sea were inferred using an inverse model initialized with ship-borne ADCP velocities. The value obtained for the full-depth net transport into the Scotia Sea is 7 ± 5 Sv. Comparing this value with the one given for the whole SSR (10.5 ± 5 Sv; Naveira-Garabato et al., 2003) we must conclude that either the contribution of the western sector to the exportation of Weddell Sea waters is more important than it was thought before, or the value given for the whole SSR clearly underestimates the actual value. The largest amount of the water crossing the western sector of the SSR is surface and intermediate water. However, comparing the fraction of bottom water (WSDW) that crosses the Hesperides Passage (1.8 ± 1.8 Sv; Palmer et al., 2012) with the outflow through the Orkney Passage (3.48 Sv according to Franco et al., 2007; 5.6 Sv according to Naveira-Garabato et al., 2002b) it results that the western sector of the SSR would still account for about a half of the exportation through the Orkney Passage. It is worth noting, however, that all the given transport estimates have a large associated uncertainty.

The unprecedented spatial resolution of the ESASSI-08 sampling across the different channels connecting the Weddell Sea with the Scotia Sea has also allowed the tracking of the Antarctic Slope Current as it crosses the ridge. The absence of the ASC west of the Antarctic Peninsula was a well known feature (Whitworth et al., 1998), but the exact path of the ASC before diluting to the south of the Drake Passage remained uncertain. Thus

Heywood et al. (2004) traced the ASC linked to the 1500m isobath as it crosses the southern flank of the ridge region at about 50ºW; later on, Thompson et al. (2009) inferred its pathway at shallower levels by using drifter data. This study has not only clarified the path of the ASC as it crosses the southern flank of the ridge, but also the outflow into the Scotia Sea through the gaps of the northern flank of the SSR.

Our results show the ASC carrying up to 3 Sv before reaching the southern flank of the SSR, in good agreement with the transport estimated further upstream by Thompson and Heywood (2008). When the ASC enters the ridge it splits into two branches. A first one surrounds the slopes of the Hesperides Trough and reaches the northern flank of the ridge crossing a narrow, shallow gap at a depth of about 700m. Once in the Scotia Sea it turns west, flowing more seaward than upstream (1100m isobath) until it is blocked by the Southern Boundary of the ACC south of the Shackleton Fracture (56ºW). A second branch enters the southern flank of the ridge further eastwards, over the 1600m isobath, and outflows into the Scotia Sea through the widest and deepest gap to the west of the Orkney Islands: the Hesperides Passage. Once in the Scotia Sea this branch also turns to the west and becomes undistinguishable within the local circulation.

The mean water property values obtained over the western sector of the SSR are about -0.29 ± 0.16 ºC and 34.56 ± 0.05, that is, much colder and slightly fresher than the values given by Naveira-Garabato et al. (2003) for the Scotia Sea (1.2 ± 1.4 ºC and 34.58 ± 0.14). This altogether with the significant volume transport suggests that the western sector of the SSR would contribute very significantly to the modification of the Scotia Sea waters. Before reaching the Scotia Sea, however, Weddell Sea waters are submitted to local modifications as they cross the ridge, particularly within the Hesperides Trough. In the last part of the thesis we have determined the source water mass proportions by applying an Optimum Multiparameter Analysis. Two different mixing schemes are needed to explain the mixing processes observed in the region. In the Powell Basin, before the Antarctic Slope Current reaches the southern flank of the SSR, diapycnal mixing taking place at the bottom boundary layer of the offshore side of the Antarctic Slope Front (ASF) results in Modified Warm Deep Water (MWDW) from a mixture of Antarctic Surface Water (AASW), Warm Deep Water (WDW), and Weddell Sea Deep Water (WSDW). Away from the bottom boundary layer, mixing processes are mainly along isopycnals: the

offshore cores of Winter Water (WW) and WDW are eroded by continental shelf waters and by colder, relatively fresher MWDW formed on the offshore side of the ASF, respectively. When these modified waters outflow into the Scotia Sea they mix isopycnally with less modified Weddell Sea water coming from the eastern gaps of the SSR. Further offshore, at the southern boundary of the Antarctic Circumpolar Current, these waters get in contact with eastward water from the Drake Passage and contribute to its ventilation.

Although the main questions posed at the beginning of the thesis have been solved, there remain some uncertainties related to different processes taking place in this region. Regarding the data processing, the magnitude of the errors associated with the estimated transports raise the necessity of an even more accurate estimation of the velocity field. This could be achieved, first, with a better understanding and modelling of the tidal currents over the ridge, particularly over the shelf-slope regions. It is not clear for instance why tidal currents are much stronger in the southern flank of the ridge than in the northern flank. Another remaining question is whether some of the strong barotropic jets observed over the shelf areas are temporary or permanent features, or even if they could be an artifact of the detiding process. The uncertainty associated with the bottom triangle extrapolation needed to compute transports at the section crossing the Hesperides Trough also emphasizes the need for higher resolution observations over such a steep bathymetry. The use of a lower ADCP could report some advantages over an ADCP.

Regarding physical process, a key issue that has not been addressed here is the seasonal and interannual variability of the observed features. For instance, is the Hesperides Trough a constant outflowing gate for Weddell Sea waters or, instead, during eventual weakenings of the northern flow it can also host waters from the Scotia Sea ?. What is the residential time of the water masses in the Hesperides Trough and how this time affects the modification of bottom waters ?. Related to the ASF/ASC, we do not know for instance if a surface warming could translate into a weakening of the ASC or, instead, a reduction of the baroclinic component would be compensated by an increase in the barotropic component. How can the bottom undercurrent observed at some locations fit with the structure of the ASF ?. How are the vertical and lateral diffusive terms related to the bottom Ekman layer on the continental slope ?. All these questions will have to be explained in future works.

REFERENCES

Ainley, D.G., and S.S. Jacobs, 1981. Sea-bird affinities for ocean and ice boundaries in the Antarctic. Deep-Sea Research A, 28, 1173–1185.

Arhan, M., K.J. Heywood, and B.A. King, 1999. The deep waters from the Southern Ocean at the entry to the Argentine Basin. Deep-Sea Research II, 46, 475-499.

Baines, P.G., 2009. A model for the structure of the Antarctic Slope Front. Deep-Sea Research II, 56, 859-873.

Broecker, W.S., 1991. The great ocean conveyor. Oceanography, 4, 79-89.

Broecker, W.S., S.L. Peacock, S. Walker, R. Weiss, E. Fahrbach, M. Schroeder, U. Mikolajewicz, C. Heinze, R. Key, T.-H. Peng, and S. Rubin, 1998. How much deep water is formed in the Southern Ocean? Journal of Geophysical Research, 103, 15833-15843.

Budillon, G., M. Pacciaroni, S. Cozzi, P. Rivaro, G. Catalano, C. Ianni, and C. Cantoni, 2003. An optimum multiparameter analysis of the shelf waters in the Ross Sea. Antarctic Science, 15 (1), 105-118.

Carmack E.C., 1974. A quantitative characterization of water masses in the Weddell Sea during summer. Deep-Sea Research, 21, 431-442.

Cushman-Roisin, B., and V. Malačič, 1997. Bottom Ekman pumping with stress-dependent eddy viscosity. Journal of Physical Oceanography, 27, 1967-1975.

Chavanne, C.P., K.J. Heywood, K.W. Nicholls, and I. Fer, 2010. Observations of the Antarctic Slope Undercurrent in the southeastern Weddell Sea. Geophysical Research Letters, 37, L13601.

Chereskin, T.K., and M. Trunnell, 1996. Correlation scales, objective mapping and geostrophic flow in the California current. Journal of Geophysical Research, 101 C10, 22619–22629.

Deacon, G.E.R., 1937. The hydrology of the Southern Ocean. Discovery Reports, 15, 3–122.

Deacon, G.E.R., and T.D. Foster, 1977. The boundary region between the Weddell Sea and Drake Passage currents. Deep-Sea Research, 24, 505-510.

DOVETAIL, 1997. Deep Ocean Ventilation Through Antarctic Intermediate Layers. U. S. Cruise Report, available from: http://www.ldeo.columbia.edu/res/fac/physocean /Dovetail/cruiserep.htm.

Ekman, V.W., 1905. On the influence of earth's rotation on ocean currents. Arkiv för Matematik, Astronomi och Fysik 2, 11.

Emery, W.J., 2003. Water Types and Water Masses. Ocean Circulation, Elsevier Science, 1556-1567.

Fahrbach, E., R.G. Peterson, G. Rohardt, P. Scholsser, and R. Bayer, 1994. Suppression of bottom water formation in the southeastern Weddell Sea. Deep-Sea Research I, 41, 389-411.

Fahrbach, E., G. Rohardt, N. Scheele, M. Schröder, V. Strass, and A. Wisotzki, 1995. Formation and discharge of deep and bottom water in the northwestern Weddell Sea. Journal of Marine Research, 53, 515-538.

Franco, B.C., M.M. Mata, A.R. Piola, and C.A.E. Garcia, 2007. Northwestern Weddell Sea deep outflow into the Scotia Sea during the austral summers of 2000 and 2001 estimated by inverse methods. Deep-Sea Research I, 55, 1815-1840.

Ganachaud, A., and C. Wunsch, 2000. Improved estimates of global ocean circulation, heat transport and mixing from hydrographic data. Nature, 408, 453-457.

Gill, A.E., 1973. Circulation and bottom water production in the Weddell Sea. Deep-Sea Research, 20, 111-140.

Golub, G.H., and W. Kahan, 1965. Calculating the singular values and pseudo-inverse of a matrix. Journal of the Society for Industrial and Applied Mathematics: Series B, Numerical Analysis 2 (2): 205–224.

Gordon, A.L., M. Visbeck, and B. Huber, 2001. Export of Weddell Sea deep and bottom water. Journal of Geophysical Research, 106, 9005-9018.

Hansen, H.P., and F. Koroleff, 1999. Determination of nutrients. Methods of Seawater Analysis. Wiley-VCH, 159–226.

Heywood, K.J., R. Locarnini, R. Frew, P. Dennins, and B. King, 1998. Transport and water masses of the Antarctic Slope Front system in the eastern Weddell Sea. Ocean, Ice, and Atmosphere: Interactions at the Antarctic Continental Margin, Antarctic Research Series, 75, 203-214.

Heywood, K.J., A.C. Naveira-Garabato, D.P. Stevens, and R.D. Muench, 2004. On the fate of the Antarctic Slope Front and the origin of the Weddell Front. Journal of Geophysical Research, 109, C06021.

Jackett, D., and T.J. McDougall, 1997. A neutral density variable for the world's oceans. Journal of Physical Oceanography, 27, 237-263.

Jacobs S.S., 1986. The Antarctic Slope Front. Antarctic Journal, 21, 123-124.

Jacobs, S.S., 1991. On the nature and significance of the Antarctic Slope Front. Marine Chemistry, 35, 9-24.

Jullion, L., K.J. Heywood, A.C. Naveira-Garabato, and D.P. Stevens, 2010. Circulation and Water Mass Modification in the Brazil–Malvinas Confluence. Journal of Physical Oceanography, 40, 845–864.

Karstensen, J., and M. Tomczak, 1998. Age determination of mixed water masses with CFC and oxygen data. Journal of Geophysical Research, 24, 2777-2780.

Killworth, P.D., 1977. Mixing on the Weddell Sea continental slope, Deep-Sea Research, 24, 427-448.

Lawson, C.L., and R.J. Hanson, 1974. Solving Least Squares Problems. Classics in Applied Mathematics, 15.

López, O., M.A. García, D. Gomis, P. Rojas, J. Sospedra, and A.S. Arcilla, 1999. Hydrographic and hydrodynamic characteristics of the eastern basin of the Bransfield Strait (Antarctica). Deep-Sea Research I, 46, 1755–1778.

Mamayev, O.I., 1975. Temperature – salinity analysis of world ocean waters. Elsevier Oceanography Series, 11.

Mathiot, P., H. Goosse, T. Fichefet, B. Barnier, and H. Gallée, 2011. Modelling the seasonal variability of the Antarctic Slope Current. Ocean Science, 7, 455-470.

McDougall, T.J., 1987. Neutral surfaces. Journal of Physical Oceanography, 17, 1950-1964.

McDougall, T.J., 1991. Parameterizing mixing in inverse models. Dynamics of Oceanic Internal Gravity Waves. 'Aha Huliko'a Hawaiian Winter Workshop, 355–386.

McIntosh, P.C., and S.R. Rintoul, 1997. Do box inverse models work? Journal of Physical Oceanography, 27, 291-308.

Morgan, P.P., 1994. Box Inverse Modelling with DOBOX 4.2. CSIRO Marine Laboratories Report, 225.

Mosby, H., 1934. The waters of the Atlantic Antarctic Ocean. Scientific results of the Norwegian Antarctic Expeditions 1927-1928, 11.

Muench, R.D., and H.H. Hellmer, 2002. The international DOVETAIL program. Deep-Sea Research II, 49 (21), 4711-4714.

Naveira-Garabato, A.C., K.J. Heywood, and D.P. Stevens, 2002a. Modification and pathways of Southern Ocean deep waters in the Scotia Sea. Deep-Sea Research I, 49 (4), 681-705.

Naveira-Garabato, A.C., E.L. McDonagh, D.P. Stevens, K.J. Heywood, and R.J. Sanders, 2002b. On the export of Antarctic Bottom Water from the Weddell Sea. Deep-Sea Research II, 49 (21), 4715-4742.

Naveira-Garabato, A.C., D.P. Stevens, and K.J. Heywood, 2003. Water mass conversion, Fluxes, and Mixing in the Scotia Sea diagnosed by an inverse model. Journal of Physical Oceanography, 33, 2565-2587.

Orsi, A.H., W.D. Nowlin Jr., and T. Whitworth III, 1993. On the circulation and stratification of the Weddell Gyre. Deep-Sea Research I, 40 (1), 169-203.

Orsi, A.H., T. Whitworth III, and W.D. Nowlin Jr., 1995. On the meridional extent and fronts of the Antarctic Circumpolar Current. Deep-Sea Research I, 42, 641-673.

Orsi, A.H., G.C. Johnson, and J.L. Bullister, 1999: Circulation, mixing, and production of Antarctic Bottom Water. Progress in Oceanography, 43, 55-109.

Orsi, A.H., and T. Whitworth III, 2005. WOCE Southern Ocean Atlas, http://wocesoatlas.tamu.edu.

Orsi, A.H., M. Palmer, D. Gomis, M. M. Flexas, Y-S. Kim, G. Jordà, C. Wiederwohl, M. Álvarez, in preparation. On the Antarctic Slope Front and Current crossing of the South Scotia Ridge.

Padman, L., H.A. Fricker, R. Coleman, S. Howard, and S. Erofeeva, 2002. A new tidal model for the Antarctic ice shelves and seas. Annals of Glaciology, 34, 247-254.

Padman, L., L. Erofeeva, and H.A. Fricker, 2008. Improving Antarctic tide models by assimilation of ICESat laser altimetry over ice shelves. Geophysical Research Letters, 35, L22504.

Palmer, M., D. Gomis, M.M. Flexas, G. Jordà, L. Jullion, T. Tsubouchi, A.C. Naveira-Garabato, 2012. Water mass pathways and transports over the South Scotia Ridge west of 50ºW. Deep-Sea Research I, 59, 8-24.

Patterson, S.L., and H.A. Sievers, 1980. The Weddell-Scotia Confluence. Journal of Physical Oceanography, 10, 1584-1610.

Perlin, A., J.N. Moum, J.M. Klymak, M.D. Levine, T. Boyd, and P.M. Kosro, 2007. Organization of stratification, turbulence, and veering in bottom Ekman layers. Journal of Geophysical Research, 112, C05S90.

Povero P., C. Misic, C. Ossola, M. Castellano, and M. Fabiano, 2003. The trophic role and ecological implications of oval faecal pellets in Terra Nova Bay (Ross Sea). Polar Biology, 26, 302–310.

Rahmstorf, S., 1997. Risk of sea-change in the Atlantic. Nature, 388, 825-826.

Reid, J.L., W.D. Nowlin Jr., and W.C. Patzert, 1977. On the characteristics and circulation of the southwestern Atlantic Ocean. Journal of Physical Oceanography, 7, 62-91.

Rintoul, S., C. Hughes, and D. Olbers, 2001. The Antarctic Circumpolar Current System. Ocean Circulation and Climate. Academic Press.

Rubio, A., D. Gomis, G. Jordà, and M. Espino, 2009. Estimating geostrophic and total velocities from CTD and ADCP data: Intercomparison of different methods. Journal of Marine Systems, 77, 61-76.

Rudnick, D.L., 1996. Intensive surveys of the Azores front: 2. Inferring the geostrophic and vertical velocity fields. Journal of Geophysical Research, 101, C7, 16291–16303.

Savidge, D.K., and J.A. Amft, 2009. Circulation on the west Antarctic Peninsula derived from 6 years of shipboard ADCP transects. Deep-Sea Research I, 56, 1633–1655.

Schodlok, M.P., H.H. Hellmer, and A. Beckmann, 2002. On the transport, variability and origin of dense water masses crossing the South Scotia Ridge. Deep-Sea Research II, 49B, 4807-4825.

Schröeder, M., and E. Fahrbach, 1999. On the structure and the transport of the eastern Weddell Gyre. Deep-Sea Research II, 46, 501–527.

Sloyan, B.M., and S.R. Rintoul, 2000. Estimates of area-averaged diapycnal fluxes from basin-scale budgets. Journal of Physical Oceanography, 30, 2320-2341.

Smith, W.H.F., and D.T. Sandwell, 1997. Global sea floor topography from satellite altimetry and ship depth soundings. Science, 277, 1956-1962.

Stewart, R.H., 2005. Introduction to physical Oceanography. Department of Oceanography, Texas A&M University.

Sverdrup, H.U., 1953. The currents off the coast of Queen Maud Land. Norsk Geografisk Tidsskrift, 14, 239-249.

Talley, L.D., G.L. Pickard, W.J. Emery, and J.H. Swift, 2011. Descriptive Physical Oceanography: An Introduction. Elsevier.

Thompson, A.F., and K.J. Heywood, 2008. Frontal structure and transport in the northwestern Weddell Sea. Deep-Sea Research I, 55, 1229-1251.

Thompson A.F., K.J. Heywood, S.E. Thorpe, A.H.H. Renner, and A. Trasviña, 2009. Surface circulation at the tip of the Antarctic Peninsula from drifters. Journal of Physical Oceanography, 39, 3-26.

Tomczak, M., and D.G.B. Large, 1989. Optimum multiparameter analysis of mixing in the thermocline of the eastern Indian Ocean. Journal of Geophysical Research, 94, 16141-16149.

Tomczak, M., 1999. Some hystorical, theoretical and applied aspects of quantitative water mass analysis. Journal of Marine Research, 57, 275-303.

Turner, J.T., 2002. Zooplankton fecal pellets, marine snow and sinking phytoplankton blooms. Aquatic Microbial Ecology, 27, 57-102.

von Gyldenfeldt, A.-B., E. Fahrbach, M.A. García, and M. Schröder, 2002. Flow variability at the tip of the Antarctic Peninsula. Deep-Sea Research II, 49, 4743–4766.

Whitworth, T., W.D. Nowlin, Jr., and S.J. Worley, 1982. The net transport of the Antarctic Circumpolar Current through Drake Passage. Journal of Physical Oceanography, 12, 960-971.

Whitworth III, T., W.D. Nowlin, A.H. Orsi, R.A. Locarnini, and S.G. Smith, 1994. Weddell Sea Shelf Water in the Bransfield Strait and Weddell-Scotia Confluence. Deep-Sea Research I, 41, 629-641.

Whitworth III, T., A.H. Orsi, S.J. Kim, W.D. Nowlin Jr., and R.A. Locarnini, 1998. Water masses and mixing near the Antarctica Slope Front. Ocean, Ice, and Atmosphere: Interactions at the Antarctic Continental Margins, Antarctic Research Series, 75, 1-27,

Wunsch, C., 1977. Determining the general circulation of the oceans: A preliminary discussion. Science, 196, 871-875.

Wunsch, C., 1996. The ocean circulation inverse problem. Cambridge University Press.

LIST OF FIGURES

LIST OF TABLES

LIST OF ACRONYMS

AABW – Antarctic Bottom Water

AASW – Antarctic Surface Water

ACC – Antarctic Circumpolar Current

ACoC – Antarctic Coastal Current

ADCP – Acoustic Doppler Currentmeter Profiler

ASC – Antarctic Slope Current

ASF – Antarctic Slope Front

AZ – Antarctic Zone

BBL – Bottom Boundary Layer

CDW – Circumpolar Deep Water

CTD – Conductivity-Temperature-Depth

DOVETAIL – Deep Ocean Ventilation Through Antarctic Intermediate Layers

ESASSI – The Spanish contribution to the SASSI project

HP – Hesperides Passage

IMEDEA – Institut Mediterrani d'Estudis Avançats

LCDW – Lower Circumpolar Deep Water

MCDW – Modified Circumpolar Deep Water

MWDW – Modified Warm Deep Water

NADW – North Atlantic Deep Water

NSR – North Scotia Ridge

OMP – Optimum Multiparameter analysis

PF – Polar Front

PFZ – Polar Frontal Zone

SACCF – Southern ACC Front

SAF – Subantarctic Front

SASSI – Synoptic Antarctic Shelf-Slope Interactions Study

SAZ – Subantarctic Zone

SB – Southern Boundary of the ACC

SSR – South Scotia Ridge

STF – Subtropical Front

SW – Shelf Water

UCDW – Upper Circumpolar Deep Water

WDW –Warm Deep Water or Weddell Deep Water

WF – Weddell Front

WOCE – World Ocean Circulation Experiment

WSBW – Weddell Sea Bottom Water

WSDW – Weddell Sea Deep Water

WW – Winter Water